Design Loads Generator: Estimation of Extreme Environmental Loadings for Ship and Offshore Applications

by

Dae-Hyun Kim

A dissertation submitted in partial fulfillment
of the requirements for the degree of
Doctor of Philosophy
(Naval Architecture and Marine Engineering)
in The University of Michigan
2012

Doctoral Committee:

Professor Armin W. Troesch, Chair
Professor Robert F. Beck
Assistant Professor Matthew D. Collette
Professor Charles R. Doering

To My Parents

ACKNOWLEDGEMENTS

As I look back on the past few years of my life in Ann Arbor, I realize how precious they were. Those wonderful years enabled me to finish this dissertation, but this would not have been possible without the help of many teachers, sponsors, friends, and my own family.

I owe a debt of gratitude to my advisor, Prof. Armin Troesch. He is one of the best teachers I have ever met in my entire life. His insights, guidance, and support made it possible to complete the dissertation. I am also deeply grateful to my committee members: the new development presented in Chapter III started with a short discussion with Prof. Charlie Doering. My discussions with him had been always enlightening, but this was more than that. Prof. Matt Collette was there whenever I needed help with the LAMP program and more. The questions Prof. Bob Beck raised infrequently always made me think harder and study more, which became an important pillar of the dissertation.

I would like to thank Mr. Allen Engle at Naval Surface Warfare Center Carderlock Division (NSWCCD) for his valuable inputs, which significantly contributed to the dissertation. In addition, the experimental data introduced in this dissertation, which I believe illustrates the power of the current research, was conducted at NSWCCD and was provided by him. I would also like to thank Mr. Kenneth Weems at Science Applications International Corporation (SAIC) for his support with the LAMP program. In addition. I would like to acknowledge that several discussions I had with Prof. Jørgen J. Jensen at Technical University of Denmark and Dr. Steven R. Winterstein, respectively, were extremely beneficial and indirectly helped me to write a better dissertation. I would also like to appreciate Ms. Kelly Cooper and Dr. Paul Hess at the Office of Naval Research for supporting this research.

Several friends at the NA&ME department directly and indirectly contributed to the dissertation. The discussions with Dave Hodapp often led me to think outside of the box, which was always exciting and helpful. I would also like to thank him for proofreading some of the dissertation. Spending time with my KNAME friends always comforted me, which without a doubt, contributed to my mental health.

I owe a great deal to Dr. Christine Feak at the English Language Institute for reading almost every line of the dissertation. Through numerous discussion sessions with her, I came to understand how to better write a paper, which will positively affect my entire career. Prof. John Swales was also extremely generous with his time in reading some of the dissertation.

I was quite nervous when I started my new life. My friends were there to encourage me. I appreciate many friends, including but not limited to my Joamo friends, at Hyundai Heavy Industry (HHI) who encouraged me to welcome the challenge of pursing the graduate study. My various experiences at HHI, which I am really proud of, naturally led me to pursue this new life in Michigan and I enjoyed it a lot.

My life after the age of 16 was practically shaped by the Pine Tree Family and I will always be thankful for that. My dear father, mother, and sister literally made me who I am. Without them, I could not have survived on this planet in the first place. Last but not least, my loving wife, Seyjung, contributed to this work in so many ways I cannot even count. I do not know what the future holds for us, but I do know I will welcome any challenge as long as she is with me.

> *Now this is not the end. It is not even the beginning of the end. But it is, perhaps, the end of the beginning.* – Sir Winston Churchill

TABLE OF CONTENTS

LIST OF FIGURES

Figure

LIST OF TABLES

Table

LIST OF APPENDICES

Appendix

ABSTRACT

Design Loads Generator: Estimation of Extreme Environmental Loadings for Ship and Offshore Applications

by

Dae-Hyun Kim

Chair: Armin W. Troesch

High-fidelity hydrodynamic loads computation systems have become available due to developments in fluid dynamics and computer science. However, the use of these programs during the concept design stage of novel marine systems remains relatively unpopular, partly due to prohibitive costs. Addressing this issue requires approaches in at least two directions. The first would be to improve the accuracy and speed of computation, while the second would be to find rational and accurate ways of determining design events. Compared to the many efforts being made in the former direction, the latter has often been considered an open question or an area of future research. The aim of the current dissertation is to address this very question.

Design processes can be highly subjective and vary significantly depending on projects. However, any rational design process should include the identification of design life and operating environments. The extreme response of a marine system under an operating environment for a finite time period should then be studied not as a deterministic event, but as a stochastic process. Therefore, it is fitting and proper to consider the distribution of extreme environmental loadings.

The distribution of extreme responses can be calculated without extensive Monte Carlo type computations through a probabilistic process, here designated as Design Loads Generator (DLG), redeveloped in this dissertation. More specifically, DLG is a process that can construct an ensemble of short input time series, the extreme responses of which follow the theoretical extreme value distribution of a Gaussian random variable for a given exposure time. The input time series are calculated based on the assumption of a linear system and a Gaussian seaway, which are both

deemed fit and proper especially during the concept design stage. Moreover, the exposure time associated with the Gaussian process becomes a good measure by which the associated nonlinear responses can be bounded. This dissertation presents several examples that show, through the use of this strategy, how the distribution of even a highly nonlinear, non-Gaussian process can be bounded, suggesting DLG can supplement or even replace the rule-based design approach.

CHAPTER I

Introduction

1.1 Estimation of Extreme Environmental Loadings

Crucial to the robust structural performance of marine vehicles and offshore units is the prediction of extreme environmental loading. The source of environmental loading includes, but is not limited to, ocean waves, winds, currents and tides. While winds, currents and tides can also become salient sources of environmental loading to offshore units, the most important environmental loading for any marine system near or on the water surface is due to ocean waves.

Traditionally, environmental loading has been incorporated into design loads estimation via a rule-based design approach. However, this inherently empirical approach may not guarantee a robust design in an unconventional system, the experience of which is limited, or when operational requirements are rather special, as in high-speed vessels. Moreover, since the estimation of loads is based on only a handful of parameters, the effects of evolutionary changes during the design process may not be fully captured in this rather standard approach.

To address this limitation, rule-based initial estimates should be further refined by incorporating results from model tests and/or computer-based direct analyses. While model tests produce reliable results when properly done, they are very expensive to conduct, especially during the concept design stage. Due to the prohibitive cost and time constraints of model testing in this stage, computer-based design or rationally-based design as explained in e.g., Hughes (1988) may be more appropriate.

As computation power has literally exploded over the last few decades, many high-fidelity, hydrodynamic load computation systems have now become available for the use in rationally-based design. However, computer-based direct analysis also does not provide a perfect solution that is readily and quickly available to naval architects. In particular, fully nonlinear problems still require a significant amount of

time to be solved even with high-performance computers, thus preventing a thorough investigation of the design space necessary to determine an optimal design. Hence, one of the open questions is how to efficiently identify the extreme environments that will yield design loads; this is a formidable task considering the inherent random nature of ocean environments and the lack of complete mathematical models for such phenomena as rogue waves.

In order to handle this issue, long-term design load estimates that require lengthy time domain simulations are often statistically extrapolated, under certain assumptions, from a series of rather short-term Monte Carlo simulations that utilizes pseudo-random number generators. However, these short-term results are still problematic in that the confidence level in the statistical estimation might be low when based on a small number of samples, not to mention that the results are dependent on the validity of the assumptions.

One of the critical assumptions includes a specific probability distribution that the target response of interest would follow, where the target response refers to a specific loading to be considered during the design process. For example, the Weibull distribution (Weibull, 1951) is widely used to model extreme hull bending moments, and many other important responses. Another important assumption relates to the proper mathematical models for ocean waves and the characteristics of the marine system in question. With regard to the ocean waves, the Gaussian model is still deemed sufficiently accurate for concept design studies. Meanwhile, the response of a marine system exhibits both linear and nonlinear types of behavior.

1.2 Objective of Current Research

The aim of the current research is not to reexamine the validity and the limitations of the assumptions described above, but rather to find a rational engineering process that can properly address the aforementioned limitations of model testing and/or computer-based design approaches utilizing the assumptions. More specifically, the problem that the current research answers is how to find an ensemble of short wave/response time histories around the design event defined in a way that is statistically meaningful. The short input time histories can then be used relatively easily as inputs to high-fidelity (or very expensive), hydrodynamic load computation systems. The inception of the idea dates back to Troesch (1997), but Alford (2008) was first to realize the idea using a non-uniform phase distribution and an optimization algorithm. Later, Kim & Troesch (2010), Kim *et al.* (2010), and Alford *et al.*

(2011) presented a more complete picture of the process by including the results from nonlinear time domain simulations. However, this early version of the Design Loads Generator (DLG) process did not completely satisfy the overall objective of finding an ensemble of inputs wave series whose distribution of resulting extreme responses matches a theoretically derived probability density function (PDF).

The current dissertation presents a significantly redeveloped probabilistic process/model, here again designated as DLG. This process can now be used to exactly and efficiently identify design events under the assumption of a linear system in the Gaussian ocean wave, eliminating the need for Monte Carlo experiments. In essence, DLG produces an ensemble of short time series around the target extreme events of a marine system. The target extreme events in DLG refer to the distribution of extreme responses that a system would experience in a given time period. The time period (or exposure time) and the distribution of extreme responses are two fundamental components assessing the risk associated with a selected design load, which will be discussed again in Sec. 2.3.

The capability to generate an ensemble of short time histories is invaluable for addressing the limitation associated with the considerable cost of applying the nonlinear time domain simulators: even high-fidelity nonlinear time domain simulators can now be routinely utilized in the concept design stage despite the cost, if the input time series are short—typically $150 \sim 200$ seconds long. More importantly, the development of multi-core CPU technology can readily be exploited to simulate the DLG ensemble of short time histories simultaneously.

The other crucial advantage of DLG over the typical Monte Carlo approach that includes time simulation with statistical extrapolation techniques, is that the physics underlying the distribution of extreme responses need not be lost in DLG. Whereas the statistical parameter fitting (e.g., the Weibull fitting) and subsequent extrapolation generate mere numbers with all the relevant physics being lost, DLG can identify an ensemble of short response time series and corresponding input wave time histories associated with the distribution of the target extreme events. This opens a possibility of calculating auxiliary, but critical input parameters for a rationally-based design. For example, the entire hull hydrodynamic pressure map associated with the maximum combined wave-induced midship bending moments and their associated impact induced midship bending moments are readily available with DLG. These external pressure distributions can then be used as input into a finite element program for subsequent structural analysis of the system.

1.3 Literature Review

As mentioned, the DLG is able to construct an ensemble of short design wave profiles identifying the design events of a marine system. How to find a short wave profile to be used as a design event has been a subject of previous studies, which are reviewed in this section.

1.3.1 New Wave Profiles

The generation of a short design wave profile under the Gaussian seaway assumption has been addressed before. For example, the most likely wave profile around an a priori maximum crest height is simply the normalized autocorrelation function multiplied by the crest height, as developed by Lindgren (1970) and demonstrated by Tromans *et al.* (1991). More specifically, on the condition that the crest height at $t = 0$ is a, the expected wave elevation can be approximated as

$$E[\zeta(t)|\zeta(0) = a, \dot{\zeta}(0) = 0] = a\rho(t) \tag{1.1}$$

where $\zeta(t)$ is a random process describing wave elevation at each time instance t, $\rho(t)$ is the normalized autocorrelation function of $\zeta(t)$, and $E[\cdot]$ is the conditional mean of the random variable $\zeta(t)$ at t.

This *New Wave* method was studied and developed further in subsequent research to address limitations in generating the short design wave profile. For example, the most likely wave may not generate the extreme response when the dynamic effect of a system is important. This limitation was addressed to a degree by Friis-Hansen & Nielsen (1995) and Taylor *et al.* (1995). Friis-Hansen & Nielsen (1995) included an additional condition on the instantaneous wave frequency in addition to the given crest height a, while Taylor *et al.* (1995) embedded the most likely wave profile in a short term random wave profile without changing the mean and the variance of the random signal to the first order. In subsequent research, Jensen (1996) derived a more general form of Eq. (1.1) to include the second order effect of a slightly non-Gaussian process.

1.3.2 Response Conditioned Wave Profiles

The New Wave method was later extended to the conditional response of linear systems. For instance, Adegeest *et al.* (1998) applied essentially the same method to obtain random response profiles conditioned on a known extreme response by embed-

ding the most likely extreme bending response profile. Adegeest *et al.* (1998) further used the corresponding linear irregular wave profile for additional nonlinear time domain simulations. While Pastoor (2002) extended Tromans *et al.* (1991) to multidirectional seaways, the embedment of the random backgrounds to the directional New Wave has never been developed. Later, Dietz *et al.* (2004) combined the work of Friis-Hansen & Nielsen (1995), Taylor *et al.* (1995), and Adegeest *et al.* (1998). In the combined approach, the linear response, conditioned on a known extreme response and an arbitrary instantaneous frequency defined by the derivate of the Hilbert transform, was first calculated, after which the conditioned linear response was embedded in random responses to calculate the distribution of the associated nonlinear random responses. A more detailed explanation of how Dietz *et al.* (2004) calculated this distribution is given in Sec. 1.3.4. The wave profiles in the above series of research studies is relatively simple to obtain. However, one potential drawback common to these approaches, including the New Wave profiles, is that the extreme value must be fixed a priori and thus the randomness inherent in the extreme value of the ocean wave for a given time period is not captured systematically by the method itself. In recognition of this limitation, a few attempts were made to make this method more useful, which will be introduced in Sec. 1.3.4.

1.3.3 FORM and SORM

In addition to the New Wave method and the Response Conditioned method, an approach popular in structural reliability theory has been applied to generate a design wave profile for a marine system. The reliability of a system has been estimated using the first order reliability method (FORM) and/or the second order reliability method (SORM). Kiureghian (2000) demonstrated that FORM and/or SORM can also be used to generate the most probable extreme wave profile leading to a known extreme response or a design event. Following this work, Jensen (2008, 2009), for example, applied FORM to several problems such as the deck sway motion of a Jack-Up unit, the parametric roll of a ship, the TLP floating foundation of an offshore wind turbine, and the midship bending moment of a ship. In order to illustrate the difference between Jensen's FORM approach and the current DLG approach, the FORM formulation used in Jensen (2008, 2009) is reviewed and summarized below.

In Jensen's FORM approach, the generation of the most probable wave profile leading to a given fixed extreme response starts from the construction of the input wave elevation. For example, the input wave profile may be written as

$$\zeta(x,t) = \sum_{i=1}^{N} a_i \sigma_i \cos(\omega_i t - k_i x) + b_i \sigma_i \sin(\omega_i t - k_i x) \tag{1.2}$$

where a_i and b_i are two uncorrelated standard normal random variables, ω_i and k_i are the discretized circular wave frequency and the wave number respectively, and σ_i is related to the input wave spectrum $S(\omega)$ through

$${\sigma_i}^2 = S(\omega_i)\Delta\omega_i \tag{1.3}$$

Note that the notation for the spatial coordinate x in one dimension wave can easily be extended to (x, y) to represent two dimensional waves. The notation x and y will also be used to denote random process/variable as used in Eq. (2.1) and Eq. (3.12). Since the difference is self-explanatory, it is not expected to cause any problem.

The spectrum of a single random wave input in this model may become degenerate, unless the number of wave components N is sufficiently large. Moreover, the random input $\zeta(x,t)$ from Eq. (1.2) may not be an accurate representation of typical input wave elevation, unless N is sufficiently large. However, the system can be nonlinear in the FORM approach, because the formulation requires only outputs of the system during the iteration of the solution scheme. Let the nonlinear response of the system under the wave input $\zeta(x,t)$ be termed as $\phi(t|a_1, b_1, a_2, b_2, ..., a_N, b_N)$. In addition, the known extreme response at an arbitrary time t_o may be written as ϕ_o. The points on the limit-state surface G then represent the infinite number of design points, where G in $2N$ space is defined as

$$G(a_1, b_1, a_2, b_2, ..., a_N, b_N) = \phi(t|a_1, b_1, a_2, b_2, ..., a_N, b_N)\big|_{t=t_o} - \phi_o = 0 \tag{1.4}$$

Of the infinite number of failure points on G, the point nearest to the origin in the $2N$ space is the design event with the highest likelihood of occurring. The most probable wave profile leading to the design event ϕ_o at $t = t_o$ can be calculated from a typical FORM code by a series of iterations, as explained in, e.g., Madsen *et al.* (2006). Specifically, the solution of Eq. (1.4) (i.e., a set of a_i and b_i) can be used to generate the wave profile using Eq. (1.2). In addition, the distance from the origin to the most likely design point can be related back to the mean outcrossing rate, which is the rate of excursions of $\phi(t)$ into the failure domain (i.e., $G \leq 0$) (Kiureghian, 2000). This mean outcrossing rate may at times be very useful, e.g., when the assessment of the mean probability of failure of a known system is a primary target of an analysis. On the other hand, the variability of the extreme response for a given time period is

not obtained in the approach, since the problem has not been formulated as such.

Although the system in Jensen (2008, 2009) is not assumed to be linear (i.e., $\phi(t_o|a_1, b_1, a_2, b_2, ..., a_N, b_N)$ and its gradient required during the iteration inside a FORM code may be generated using a nonlinear time domain code), FORM essentially generates an equivalent Gaussian process. In other words, FORM linearizes the limit-state surface. Like the original New Wave method proposed by Tromans *et al.* (1991), this approach generates only one response profile and the associated incident wave profile, conditioned on an a priori extreme response. In other words, FORM does not directly address the following questions, which are of critical significance to any marine designer:

- *What would the distribution of extreme responses and corresponding inputs for the design lifetime of a system be like?*
- *What are the individual extreme responses and corresponding inputs that have a desired probability of non-exceedance in the distribution?*

As explained in Sec. 1.2, the distribution of the extreme responses is important, because of the random nature of ocean environments. For example, the maximum response would not be the same even for two identical vessels operating under the statistically identical environmental and operating conditions for their entire design lifetime. Identifying this distribution would thus make it possible to assess the confidence level of the design of a system. In addition, the capability to assess each individual input time series associated with the distribution of the extreme responses would be invaluable because the nonlinear time domain simulators can now be applied. Recognizing the importance of the distribution, a small number of attempts to address at least the first question have been made utilizing the aforementioned research, which will be a topic of the next section.

1.3.4 Unconditioning Conditioned Profiles

Cassidy (1999) proposed a convolution technique, based on Taylor *et al.* (1995), to "approximate" the distribution of the extreme responses that a Jack-Up structure would experience for a given time period. In this procedure, five discrete crest elevations representative of the expected range of wave heights in a three-hour storm were first selected, after which 200 conditioned wave profiles per each crest height were generated using Taylor *et al.* (1995). Cassidy (1999) then simulated these 1000 short conditioned wave profiles in time domain to construct a diagram that shows

200 possible relations between the crest height and the response height. The cost associated with the construction of the diagram may not be cheap, but the generation of additional extreme responses is readily available at a small cost. While this is a very creative procedure, the mathematical rigorousness associated with this process is somewhat questionable. For example, it remains to be seen whether 200 conditioned wave profiles, generated by Taylor *et al.* (1995), can fully capture the randomness associated with the extreme wave profiles for the given exposure time. In addition, relating to the two questions in the previous section, this approach is not able to determine the individual extreme response and corresponding inputs associated with the approximate distribution of extreme responses. Therefore, the results of this approach can not be used in subsequent higher fidelity simulations.

Dietz *et al.* (2004) introduced a similar approach. As mentioned in Sec. 1.3.2, Dietz *et al.* (2004) combined the work of Friis-Hansen & Nielsen (1995), Taylor *et al.* (1995), and Adegeest *et al.* (1998). In addition, Dietz *et al.* (2004) applied a total probability theorem to "un-condition" the response conditioned profile:

$$F_{R_{NL}}(r_{NL}\big|H_s,T_z,V,\beta)=\int_0^\infty F_{R_{NL}}(r_{NL}\big|R_L=r_L,H_s,T_z,V,\beta)f_{R_L}(r_L)dr_L \qquad (1.5)$$

where R_{NL} is the nonlinear response, R_L is the linear response used in the response condition wave profile, H_s and T_z are the significant wave height and the characteristic period of the input wave spectrum, V is the cruise velocity of a vessel, and β is the wave heading.

The calculation of $F_{R_{NL}}(r_{NL}\big|R_L=r_L,H_s,T_z,V,\beta)$ starts from generating the response conditioned wave and the associated incident wave profile (Adegeest *et al.*, 1998). Utilizing a nonlinear time domain simulator, the associated nonlinear response time histories can be calculated. By repeating this process multiple times for a few different values of r_L that follow a Rayleigh distribution, $F_{R_{NL}}(r_{NL}\big|H_s,T_z,V,\beta)$ might be calculated if the following issues are addressed properly.

- How should R_L be discretized?
- How many random backgrounds should be used to generate $F_{R_{NL}}(r_{NL}\big|R_L=r_L,h_s,t_z,v,\beta)$?

Dietz *et al.* (2004) applied 15 points in the discretization of R_L and $100\sim250$ random backgrounds in the generation of $F_{R_{NL}}(r_{NL}\big|R_L=r_L,h_s,t_z,v,\beta)$. Consequently, the total number of short simulations for nonlinear bending moments was between 1500 and 3750. In addition, Dietz *et al.* (2004) had to apply curve fitting

techniques to address the issues associated with using a finite number of simulations to calculate Eq. (1.5). This approach alone cannot generate the distribution of extreme responses for a given exposure time. Later in the paper, Dietz *et al.* (2004) addressed this limitation by stating that it might be possible using the generalized extreme value distribution of order statistics, but did not present a result. In fact, it would be possible to calculate the distribution of extreme responses for a given exposure time if the above two questions were to be addressed properly. However, like Cassidy (1999), it will still not be possible to resolve the distribution directly into the individual extreme responses and corresponding inputs, because the information has been lost in the construction of the distribution.

1.3.5 Random Experiments

Another way of summarizing and understanding the literature reviewed from Sec. 1.3.1 to Sec. 1.3.4 is to consider several different random experiments (or Monte Carlo simulations):

- Random Experiment I: Simulate random seaways representing a given sea spectrum, and collect the short wave profiles around an a priori extreme crest height. By continuing this experiment, an ensemble average of the short wave profiles around the given crest height can be obtained.

- Random Experiment II: Simulate a dynamic marine system in random seaways representing a given sea spectrum and an operational condition, and continuously collect the peaks/troughs of the response. Order statistics can then be used to present the collected maxima/minima in a cumulative distribution function (CDF) plot. There is no explicit condition on the length of the simulation time in this experiment. As the length of the simulation increases, the maximum CDF value out of this experiment will converge to 1.

- Random Experiment III: Simulate a dynamic marine system for T hours in random seaways representing a given sea spectrum and an operational condition and find the extrema of the response. By repeating this experiment multiple times, the extreme value distribution of the largest response in T hours and the corresponding wave inputs can be calculated.

The results of Random Experiment I is what the New Wave approach in Sec. 1.3.1 aims to approximate. Specifically, Random Experiment I should be compared

with Tromans *et al.* (1991). If the additional condition about the instantaneous frequency is added in Random Experiment I, Friis-Hansen & Nielsen (1995) would be recovered. Of course, each short wave profile around an a priori extreme crest height should be comparable to Taylor *et al.* (1995). The response conditioned approach in Sec. 1.3.2 is essentially identical to the New Wave, except that it is applied to the response of a system under the assumption of a linear system. The associated incident wave profile is back-calculated, which can then be plugged into nonlinear simulators. The FORM approach by Jensen (2008, 2009) can also be substituted for Random Experiment I, which is not sufficient to complete a design process directly without further assumptions. Moreover, a single time series, whether it represents an ensemble average or the most likely wave profile, will not be sufficient to capture all the randomness associated with the response of the system.

Sec. 1.3.4 explained how Cassidy (1999) attempted to address Random Experiment III based on Random Experiment I. Dietz *et al.* (2004) followed a similar path. While Dietz *et al.* (2004) is essentially centered on Random Experiment I, a mathematical equation to model Random Experiment II based on Random Experiment I is also proposed with some results. Moreover, the possibility of approximating Random Experiment III based on Random Experiment II was suggested, but no attempt was made to show any results.

Random Experiment III is crucial to the sound design of a marine system, because it relates to the lifetime of the system and the randomness associated with the time period. Alford (2008) showed the possibility of reducing the time required to conduct Random Experiment III. However, as mentioned previously, this version of the DLG process was incomplete in the sense that the matching between the theoretical extreme value distribution and the distribution of the DLG responses was not so good. Naturally, the current research draws on the insights obtained from Alford (2008), which will be examined carefully in Chapters II $\sim$ III.

This dissertation will demonstrate that Random Experiment III can be extremely useful to statistically bound even highly nonlinear responses, such as extreme midship whipping responses or hull impact pressures, in Chapters VI $\sim$ VII.

1.4 Overview of Current Thesis

As indicated earlier, the current dissertation presents the development of the DLG process. In addition, the application of the process to a few important types of ship responses will be introduced. In Chapter I, the previous research on how to find a

design wave profile has been examined. Although the previous studies reported in the literature review bear some resemblance to DLG, there exists a critical difference as elaborated in Sec. 1.3.5. Chapter II starts by introducing a Gaussian random process, and proceeds to the extreme value theory of the process based on order statistics. In other words, the extreme value theory of a Gaussian process is the basis of the current research. A formulation of the problem is presented in Chapter III, followed by a new solution scheme developed for the current research. This solution method permits, for the first time, a numerically accurate representation of the extreme value distribution based on an ensemble of short time series. Chapter IV extends the solution in Chapter II to multidirectional cases and shows that the current formulation of DLG can be applied to address, for instance, the extreme response statistics of a system under a bidirectional or even short-crested seaway. Important in the current DLG model is the nonlinear time domain simulations, for which the Large Amplitude Motion Program (LAMP) is used. Therefore, the LAMP program is introduced with its post-processors in Chapter V. Explained simultaneously in this chapter is how to execute a typical statistical extrapolation based on short-term time domain simulations. The remaining chapters are devoted to presenting the results of the current formulation of DLG applied to the estimation of extreme midship bending moments (Chapter VI) and extreme impact-induced hull pressures (Chapter VII). Chapter VIII then summarizes the dissertation with recommendations for future research.

CHAPTER II

Background

2.1 Gaussian Random Process

Consider a random process $x(t)$ that is expressed as the summation of cosine functions:

$$x(t) = \sum_{j=1}^{N} a_j \cos(\omega_j t + \epsilon_j) \tag{2.1}$$

where

$$a_j = \sqrt{2S(\omega_j)\Delta\omega_j} \tag{2.2}$$

and $S(\omega)$ is a single-sided spectrum representing the process, and the phase angles ϵ_j are uniformly distributed random variables between $-\pi$ and π. As N goes to infinity, the random variable X expressed by the random process $x(t)$ approaches the zero-mean Gaussian random variable due to a central limit theorem. Refer to, for example, Feller (1965) for the derivation of this version of the central limit theorem. The probability density function (PDF) of the random variable X, when N is sufficiently large, may still be approximated as a Gaussian distribution. Therefore, the PDF of X is

$$f_X(x) = \frac{1}{\sigma\sqrt{2\pi}}\ \mathrm{e}^{-x^2/(2\sigma^2)} \tag{2.3}$$

where the standard deviation of this zero-mean process, σ, can be calculated from Eq. (2.2) as

$$\sigma^2 = \int_0^\infty S(\omega)\,\mathrm{d}\omega \approx \sum_{j=1}^{N} S(\omega_j)\Delta\omega_j = \sum_{j=1}^{N} \frac{1}{2} a_j^2 \tag{2.4}$$

The cumulative distribution function (CDF) of X defined by Eq. (2.3) may be expressed using the CDF of the standard normal distribution $\Phi(\cdot)$ as

$$F_X(x) = \int_{-\infty}^{x} \frac{1}{\sigma\sqrt{2\pi}}\, \mathrm{e}^{-t^2/(2\sigma^2)}\, \mathrm{d}t = \int_{-\infty}^{x/\sigma} \frac{1}{\sqrt{2\pi}}\, \mathrm{e}^{-t^2/2}\, \mathrm{d}t = \Phi\Big(\frac{x}{\sigma}\Big) \tag{2.5}$$

A stochastic ocean seaway can be analyzed using this random process $x(t)$ (St. Denis & Pierson, 1953; Longuet-Higgins, 1957). The Gaussian model is somewhat limited in the sense that it is not able to capture, for example, a breaking wave or the nonlinear evolution of waves, which may affect the lifetime design loads of the system. However, as Ochi (1998) stated,

> *It has been verified through observations at sea as well as in laboratory tests that waves can be considered a Gaussian random process even in very severe seas if the water depth is sufficiently deep.*

Moreover, this model will produce a reliable first estimate of design loads especially during the concept design stage, where the fast and efficient investigation of the whole design space is most desired.

The response of a linear system under the Gaussian random wave input can also be expressed using Eq. (2.1) (St. Denis & Pierson, 1953). Unless specified otherwise, however, the random variable X denotes the target response of a system in this research. Hence, $S(\omega)$ in general should represent a response spectrum of the system.

One aspect that should be noted in using this model is that the number of harmonic components (or Fourier coefficients) N should be sufficiently large, not only because the central limit theorem requires an infinitely large N in Eq. (2.1), but also because the maximum value out of this model is bounded by $x_{\max}$ in Eq. (2.6). In other words, an insufficient N can corrupt the extreme value statistics of the response from this model.

$$x_{\max} = \sum_{j=1}^{N} a_j \tag{2.6}$$

In addition, Eq. (2.6) suggests that a set of a_j plays an important role, because $x_{\max}$ is determined by the set of a_j (or the shape of the response spectrum of the target process). The other reason why N has to be large enough is, of course, to maintain the variance of the process as close as possible to the theoretical value. A more detailed discussion of the effect of N is included in Appendix A.

2.2 Extreme Value Distribution

Consider a random experiment that simulates random seaways for a sea spectrum representing the given operational condition for T hours and finds the extreme of a response. By repeating this experiment multiple (say, m) times, the distribution of the extreme response for T hours can be obtained (i.e., Random Experiment III in Sec. 1.3.5). These experiments are analogous to finding the distribution of the extreme response that m identical marine systems (e.g., ship and/or offshore unit) would experience in T hours for the same operational condition. Although relatively straightforward, the experiments will take a significant amount of time as T and m increase if a typical Monte Carlo approach is chosen to get the distribution. How to obtain this distribution efficiently is one of the most important questions addressed in this dissertation.

This extreme value distribution answers, to a degree, one of the most important questions that naval architects or ocean engineers should raise during the design process of any marine system: how to determine the distribution of extreme responses of the system for a given time period T.

The extreme response, by definition, includes both extreme (positive/negative) maxima and minima of the response time histories. In order to determine the extreme of the positive maxima, for example, the PDF of the positive maxima needs to be obtained first, which can be derived in a dimensionless form (see e.g., Ochi, 1990):

$$f_{\Xi}(\xi) = \frac{2}{1+\sqrt{1-\varepsilon^2}}\left[\frac{\varepsilon}{\sqrt{2\pi}}\,\mathrm{e}^{-\xi^2/(2\varepsilon^2)} + \sqrt{1-\varepsilon^2}\;\xi\;\mathrm{e}^{-\xi^2/2}\;\Phi\left(\frac{\sqrt{1-\varepsilon^2}}{\varepsilon}\xi\right)\right] \tag{2.7}$$

where ξ is the normalized positive maxima $\tilde{x}/\sigma$, $\tilde{x}$ is the positive maxima. The broadness (or bandwidth) parameter ε is defined as

$$\varepsilon = \sqrt{1 - \frac{m_2^2}{m_0 m_4}} \tag{2.8}$$

where m_k is the k^{th} moment of the spectrum of the process defined as

$$m_k = \int_0^\infty \omega^k S(\omega)\,\mathrm{d}\omega \tag{2.9}$$

The derivation of a more general PDF that includes both positive and negative max-

ima was originally given in Cartwright & Longuet-Higgins (1956). Without loss of generality, however, the discussion below is limited to the extreme positive maxima.

If ε is zero, Eq. (2.7) becomes the PDF of the Rayleigh distribution. In dimensional form, the PDF and CDF or the Rayleigh distribution are

$$f_{\tilde{X}}(\tilde{x}) = \frac{\tilde{x}}{\sigma^2} \mathrm{e}^{-\tilde{x}^2/(2\sigma^2)} \tag{2.10}$$

$$F_{\tilde{X}}(\tilde{x}) = 1 - \mathrm{e}^{-\tilde{x}^2/(2\sigma^2)} \tag{2.11}$$

where the tilde notation emphasizes the fact that this random variable comes from the envelope process of $x(t)$. Specifically, the envelope process of a narrow-banded zero-mean Gaussian random process with a variance σ^2 follows the Rayleigh distribution given in Eqs. (2.10) $\sim$ (2.11).

Meanwhile, the largest value in m independent samples, when these samples follow an independent and identical PDF of $f_X(x)$ and CDF of $F_X(x)$, is also a random variable that may be designated as X_m. From the set of ordered samples $(x_1, x_2, x_3, \cdots, x_k, \cdots, x_m)$[1], the CDF of X_m can be calculated as

$$\begin{aligned} F_{X_m}(x) &= P(x_1 \le x, x_2 \le x, x_3 \le x, \cdots, x_m \le x) \\ &= P(x_1 \le x)P(x_2 \le x)P(x_3 \le x)\cdots P(x_m \le x) \\ &= F_X(x)F_X(x)F_X(x)\cdots F_X(x) = \big(F_X(x)\big)^m \end{aligned} \tag{2.12}$$

This equation is referred to as the exact distribution of extremes in Gumbel (1958). The derivative of Eq. (2.12) yields the PDF of X_m as

$$f_{X_m}(x) = m f_X(x) \big(F_X(x)\big)^{m-1} \tag{2.13}$$

A notable fact from Eq. (2.13) is that the most likely extreme value, termed as $\hat{x}$, is related back to the number of samples m associated with the extreme value distribution, which is

$$\frac{1}{m} \sim 1 - F_X(\hat{x}) \quad \text{as} \quad m \to \infty \tag{2.14}$$

Eq. (2.13) is a theoretical PDF of the largest value in m positive maxima, when Eq. (2.7) and the associated CDF are substituted for $f_X(x)$ and $F_X(x)$ respectively. For example, the distribution of the extreme values of n samples that follow the

[1] x_k indicates k^{th} value from the smallest sample in the set.

Rayleigh distribution, of which PDF and CDF are Eqs. (2.10) $\sim$ (2.11), has been widely used to model the distribution of, for example, extreme wave heights:

$$f_{\tilde{X}_n}(x) = n\left(\frac{x}{\sigma^2}\mathrm{e}^{-x^2/(2\sigma^2)}\right)\left(1-\mathrm{e}^{-x^2/(2\sigma^2)}\right)^{n-1} \tag{2.15}$$

In the mean time, an asymptotically identical extreme value distribution can be obtained from the Gaussian distribution. Specifically, when Eq. (2.13) is used, the largest value in m independent zero-mean Gaussian random samples is expressed as

$$f_{X_m}(x) = m\left(\frac{1}{\sigma\sqrt{2\pi}}\,\mathrm{e}^{-x^2/(2\sigma^2)}\right)\left(\Phi\left(\frac{x}{\sigma}\right)\right)^{m-1} \tag{2.16}$$

In order for Eq. (2.15) and Eq. (2.16) to be the same asymptotically, m and n should satisfy Eq. (2.14) for the same most likely extreme value $\hat{x}$. Hence, m is analogous to n and/or T in the sense that they all measure the exposure time inherent in the extreme value distribution.

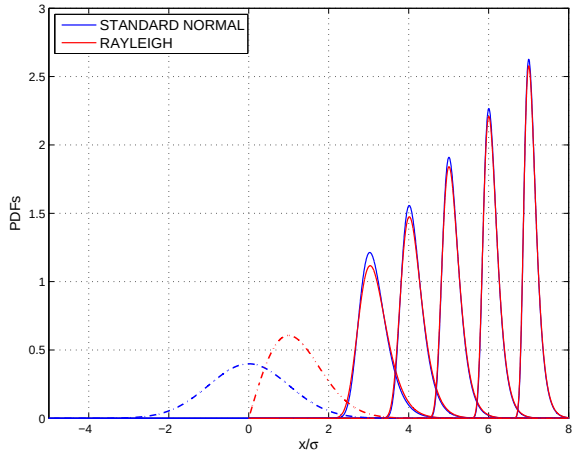

Figure 2.1: Asymptotically Equal Extreme Value Distributions Based on Gaussian Process and Based on Corresponding Rayleigh Process [TEV = 3, 4, 5, 6, and 7]

In Fig. 2.1, these two asymptotically identical extreme value distributions from Eq. (2.15) and Eq. (2.16) as well as the distributions of two original processes are given for five different Target Extreme Values (TEV), where TEV is defined as

$$\mathrm{TEV} = \frac{\hat{x}}{\sigma} \tag{2.17}$$

Table 2.1 shows n and m for several TEVs. Note that the numbers are rounded to the

TEV	m	n
3.0	741	90
3.5	4,299	457
4.0	31,574	2,981
4.5	294,219	24,959
5.0	3,488,556	268,337
5.5	52,660,508	3,704,282
6.0	1,013,594,635	65,659,969
6.5	24,900,406,809	1,494,413,991
7.0	781,332,343,402	43,673,174,852

Table 2.1: TEV and Corresponding Number of Samples of Gaussian Random Variable (m) and Rayleigh Random Variable (n)

nearest integer. It is evident that TEV is a scale closely related to the exposure time of the extreme events: a higher TEV represents a longer exposure time. Specifically, TEV can be converted to the exposure time and vice versa using the mean response period and the following relation as shown, e.g., in Ochi (1990).

$$\mathrm{TEV} = \left[2\ln\Big(\frac{2\sqrt{1-\varepsilon^2}}{1+\sqrt{1-\varepsilon^2}} n \Big) \right]^{1/2} \tag{2.18}$$

where ε is the broadness parameter and n is the expected number of peaks or troughs (i.e. comparable to the number of samples of the Rayleigh random variable when ε is zero) in the exposure time.

When TEV is 5, for example, the design event may be called a 5σ event. As Eq. (2.17) indicates, the most likely extreme values of the distribution would be five times the standard deviation of the process. However, it should be noted that the design event with a specific TEV in DLG is not a single realization that produces an extreme value, but an ensemble of realizations that produce a complete distribution of extreme values associated with a given exposure time

Although the Rayleigh distribution is much more straightforward to relate the exposure time T to the number of samples to be simulated, the current formulation of DLG is based on the Gaussian distribution due to the simplicity in numerical implementation. Following this approach, DLG is free of the additional requirement that the process needs to be narrow-banded, and the computation time required to calculate the derivatives of the time series. This is possible, as mentioned above, due to the inherent relation between the Gaussian random variable and the Rayleigh distribution. Therefore, the investigation of the maximum of the positive maxima of

the Gaussian process can be achieved by finding the maximum of the original process.

As for the accuracy of Eq. (2.13) as a basis of DLG, Fig. 2.2 shows a comparison between the histogram obtained from Monte Carlo simulations using a normally distributed psuedo-random number generator (NORMRND) and the theoretical extreme value distribution[2] of a Gaussian random variable (THEORY) given in Eq. (2.16). The number of total realizations N_{runs} obtained through Monte Carlo simulations is 50000, and each realization is the largest value in 3488556 normally distributed random samples. Therefore, the total number of Gaussian random samples generated for this figure is about 1.74×10^{11}.

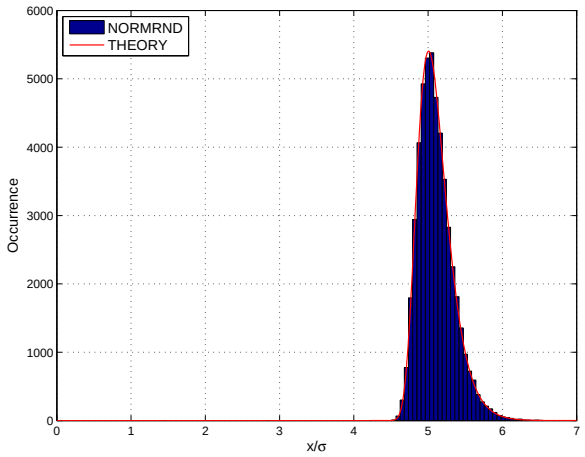

Figure 2.2: Comparison between Theoretical Extreme Value Distribution and Histogram from Gaussian Random Samples

2.3 Cell-Based Design

The extreme value distribution is important in the sense that it allows designers to determine the design event rationally. Specifically, the risk parameter α associated with using $\bar{x}_m$ as a design load is defined by

$$\int_{-\infty}^{\bar{x}_m} f_{X_m}(x)\mathrm{d}x = [F_X(\bar{x}_m)]^m = 1 - \alpha \tag{2.19}$$

[2]Strictly speaking, this is not a PDF but a histogram expressed in terms of the expected number of occurrence (or frequency) for each bin. However, it is often called as a distribution or a PDF in this dissertation for the purpose of simplicity.

Instead of the risk parameter α, the probability of non-exceedance (PNE) defined by Eq. (2.20) is often used to represent the risk level.

$$\text{PNE} = 1 - \alpha \tag{2.20}$$

This parameter, either α or PNE, is a useful metric to evaluate the reliability of a system, which is essentially the probability that no failure will occur in a given operation time interval.

In order to perform a typical loads analysis using this approach, the total operational life of a ship (D_T) is typically divided into a finite number (M) of "cells" wherein ship speed and heading are held constant, and wave conditions are stationary and ergodic. In this approach, the variability of the ocean environment is approximated by a collection of independent stationary process. This cell-based approach does not, however, imply that all events associated with a cell occur consecutively.

The frequencies of occurrence of speed, heading, and sea condition are determined by oceanographic observations and by log book analyses. These frequencies of occurrence and the assumed total operational life of the ship serve to determine the expected length of time (D_i) that a ship spends in each operational cell:

$$D_T = \sum_{i=1}^{M} D_i \tag{2.21}$$

A formal application of probability theory requires that the extreme value probability distributions be determined for each cell. Combining the M extreme values for each cell based on the frequency of occurrence will then allow the distribution of lifetime design respons to be calculated as explained in Richardson (2007).

$$F_L(x) = \prod_{i=1}^{M} F_{Ci}(x) \tag{2.22}$$

where $F_{Ci}(x)$ is the CDF of the extreme load from i^{th} cell and $F_L(x)$ is the CDF of the lifetime extreme response. Therefore, $F_L(l)$ is the lifetime probability of the extreme response not exceeding the load level l, or the PNE associated with the lifetime design load l. The exposure time (operation period) for each cell is accounted for in the estimation of the CDF. The CDF, the extreme value distribution of the response from a given cell, or equivalently $F_{Ci}(x)$. What the DLG approach can produce is the extreme value distribution of the response from a given cell, or equivalently $F_{Ci}(x)$.

Given that the total number of operational cells M may reach 2000 or more, previ-

ous experience is often used to determine which operational cells need to be examined in detail. In fact, limited resources and constrained testing schedules frequently dictate that the lifetime load is based on the distribution of maxima of a few few cells. Mathematically, $F_{Ci}(x)$ from many cells will not come into play in the calculation of $F_L(x)$ for a value in the upper tail, because the CDF asymptotically goes to 1 as x goes to infinity. Even so, the calculation of $G_{Ci}(x)$ using a high-fidelity load computation tool is a formidable task. Accordingly, as mentioned in Sec. 1.1, statistical extrapolation techniques are often used.

As explained so far, the extreme value distribution expressed in Eq. (2.16) is very important, but it has a critical limitation in that the shape of $x(t)$ around X_m has been lost. This is a crucial limitation for any time domain computational effort. In order to reconstruct the shape of $x(t)$ around X_m, a set of ϵ_j in Eq. (2.1) should be preserved, which can be accomplished through Monte Carlo simulations similar to Fig. 2.2. Nevertheless, if this histogram is to be generated based on Eq. (2.1) with TEV and N being 5 and 201, respectively, the total number of uniformly distributed random samples exceeds 3.51×10^{13}. Considering the fact that a typical design operation time for each cell of a marine system is roughly located between TEV = 4 and TEV = 6, there are multiple cells to be investigated for each mode of response, and the computational load to generate and handle the astronomical number of random samples is onerous, an approach through typical Monte Carlo simulations is not a feasible option.

How to overcome this challenge is the focus of the current dissertation. The natural next step to address the challenge is to study the set of phase angles ϵ_j as random variables, because X_m itself is a random variable. Hence, the PDF of ϵ_j should be investigated if the reconstruction of an ensemble of $x(t)$ associated with the extreme value distribution is desired, which is a topic of the next section.

2.4 Non-Uniform Phase Distribution

Consider that a realization of the Gaussian process ${}^1x(t)$, the record length of which is T, reaches its maximum at an arbitrary time $t = t_1$. The short time series around the extreme response from Eq. (2.1) can be linearly transformed such that the extreme occurs at $t = 0$, and the short time series can still be modeled by Eq. (2.1) as

$$ {}^1x_m(0) = \sum_{j=1}^{N} a_j \cos({}^1\epsilon_{m_j}) \tag{2.23} $$

By definition of the random process, the maximum from another random realization, e.g., ${}^2x(t)$, will almost certainly be different from that of ${}^1x(t)$. By repeating this random experiment, an ensemble of short time series around $t = 0$ can be collected. Note that the superscript notation is used to denote the number of samples in the ensemble. In addition, two random variables X'_m and E_{m_j}, that model the maximum at $t = 0$ (${}^kx_m(0)$) and the associated set of of phase angles (${}^k\epsilon_{m_j}$) may be approximated:

$$X'_m : {}^1x_m(0), {}^2x_m(0), {}^3x_m(0), \ldots, {}^kx_m(0) \tag{2.24}$$

$$E_{m_j} : {}^1\epsilon_{m_j}, {}^2\epsilon_{m_j}, {}^3\epsilon_{m_j}, \ldots, {}^k\epsilon_{m_j} \tag{2.25}$$

where the prime notation is added to X_m to differentiate it from the theoretical value defined by Eq. (2.13), the subscript m is due to the fact that the distribution of the maximum (i.e., the largest positive maxima) in T is asymptotically equal to the distribution of the largest of m Gaussian samples, as demonstrated in Sec. 2.2. Note that ${}^k\epsilon_{m_j}$ is not a single random number but a set of N random phase angles, as j takes a value between 1 and N

As k increases, the random variable X'_m should assume a certain distribution. Specifically, the PDF of X'_m follows Eq. (2.16) asymptotically as m increases. In a similar way, as k increases, E_{m_j} should assume single/multiple distribution(s), too. If the distribution(s) of the phase angles ϵ_{m_j} is known, the shape of the time series around $x(0)$ in a short window can be determined. Moreover, assuming a linear system, the incident wave profile can be reverse-calculated, as mentioned in Sec. 2.1, which facilitates the use of even fully nonlinear hydrodynamic simulators during the concept design stage.

Therefore, roughly speaking, the core of DLG is to find the distribution(s) of phase angles ϵ_{m_j} associated with the distribution of X'_m. In order to address the distribution(s) of E_{m_j}, Alford (2008) hypothesized that the set of phase angles ϵ_{m_j} associated with X'_m are independent and non-identically distributed (*inid*) for each j (or $E_{m_1}, E_{m_2}, \ldots, E_{m_N}$ are mutually independent and non-identically distributed). In addition, Alford (2008) modeled ϵ_{m_j} using a modified Gaussian distribution of which parameter is λ_j based on the observation from a series of numerical experiments. The modified Gaussian distribution was defined as

$$f_{E_{m_j}}(z) = \frac{1}{\lambda_j\sqrt{2\pi}}\, \mathrm{e}^{-z^2/(2\lambda_j^2)} + \frac{1}{2\pi}\left(1 - \mathrm{erf}\left(\frac{\pi}{\lambda_j\sqrt{2}}\right)\right), \quad -\pi \le z < \pi \tag{2.26}$$

where z, not ϵ_{m_j}, is used as an argument to simplify the equation, and $\mathrm{erf}(\cdot)$ is the

standard error function defined as

$$\mathrm{erf}(x) = \frac{2}{\sqrt{\pi}} \int_0^x \mathrm{e}^{-t^2}\,\mathrm{d}t \tag{2.27}$$

Using Eq. (2.26), λ_j was assumed to be positive, but less than or equal to 10 in Alford (2008). This is because as λ_j increases, the modified Gaussian distribution almost becomes a uniform distribution as shown in Fig. 2.3. Hence stopping at $\lambda_j = 10$ made little difference in terms of the shape of the distribution, saving a significant amount time spent on the solution process. Although the approximation of ϵ_{m_j} using the modified Gaussian distribution introduces some error, the effect of which will be discussed visually in Sec. 3.3, the fact that the distribution is expressed as a single parameter is highly beneficial.

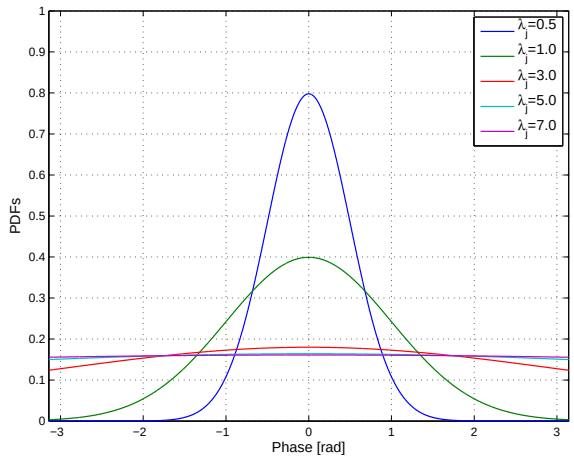

Figure 2.3: Modified Gaussian Distributions with Parameter λ_j

2.5 Characteristic Function of Extreme Value Distribution

In probability theory, the characteristic function of a random variable X is defined as

$$\psi(s) = E[\mathrm{e}^{isX}] = \int_{-\infty}^{\infty} f_X(x)\ \mathrm{e}^{isx}\,\mathrm{d}x, \quad -\infty < s < \infty \tag{2.28}$$

which is essentially the Fourier transform of the PDF of the random variable X. Therefore, once the characteristic function is determined, the PDF of the corresponding random variable can be uniquely determined by calculating the inverse Fourier

transform of the characteristic function. From this point on, the domain of the characteristic function will be omitted for simplification, unless required for clarity.

Since the PDF of X_m is given as Eq. (2.16), the characteristic function of the theoretical extreme value distribution of the Gaussian process can be determined by calculating

$$E[\mathrm{e}^{isX_m}] = \int_{-\infty}^{\infty} \frac{m}{\sigma\sqrt{2\pi}}\, \mathrm{e}^{-x^2/(2\sigma^2)} \left(\Phi\left(\frac{x}{\sigma}\right)\right)^{m-1}\, \mathrm{e}^{isx}\, \mathrm{d}x \tag{2.29}$$

This function should be identical to the characteristic function of X'_m. Alford (2008) used this fact to derive the equation to be solved, based on the hypothesis that the phase angles are *inid* and the PDF of ϵ_{m_j} is defined by Eq. (2.26). That is

$$\begin{aligned}
&\int_{-\infty}^{\infty} \frac{m}{\sigma\sqrt{2\pi}}\, \mathrm{e}^{-x^2/(2\sigma^2)} \left(\Phi\left(\frac{x}{\sigma}\right)\right)^{m-1}\, \mathrm{e}^{isx}\, \mathrm{d}x \\
&\stackrel{?}{=} \prod_{j=1}^{N} \int_{-1}^{1} \frac{\mathrm{e}^{ia_j sy}}{\pi\lambda_j\sqrt{1-y^2}} \left\{\sqrt{2\pi}\, \mathrm{e}^{-(\arccos y)^2/(2\lambda_j^2)} - \lambda_j\, \mathrm{erf}\left(\pi/(\lambda_j\sqrt{2})\right) + \lambda_j\right\} \mathrm{d}y
\end{aligned} \tag{2.30}$$

The derivation of the right-hand side of the above equation, the characteristic function of X'_m, is elaborated again in Apendix B due to its importance in the generalization of Eq. (2.1) for short-crested seaways, which is the topic of Chapter IV.

Since Eq. (2.30) is a highly nonlinear equation without a known exact solution, Alford (2008) used an optimization scheme developed by Rowan (1990) to find a set of the parameters λ_j that would minimize the L1 norm of the difference between the left hand side and the right hand side of Eq. (2.30). The question mark on top of the equal sign in Eq. (2.30) is to indicate that, as mentioned in Chapter I, Alford (2008) was not successful at finding a satisfactory solution, but only an approximate engineering solution. While a more detailed explanation of Alford (2008) will be covered in the next chapter, the new developments and improvements made in the current research will be the focus of the chapter.

CHAPTER III

Problem Formulation

3.1 Governing Equation

As stated in Eq. (2.30), the governing equation of DLG can be expressed as

$$\psi_{X_m}(s; m, \sigma) = \psi_{X'_m}(s; a_1, a_2, \ldots, a_N, \lambda_1, \lambda_2, \ldots, \lambda_N) \tag{3.1}$$

where ψ_{X_m} and $\psi_{X'_m}$ are defined as

$$\psi_{X_m}(s; m, \sigma) = \int_{-\infty}^{\infty} \frac{m}{\sigma\sqrt{2\pi}}\, \mathrm{e}^{-x^2/(2\sigma^2)} \left(\Phi\left(\frac{x}{\sigma}\right)\right)^{m-1}\, \mathrm{e}^{isx}\, \mathrm{d}x \tag{3.2}$$

and

$$\begin{aligned}&\psi_{X'_m}(s; a_1, a_2, \ldots, a_N, \lambda_1, \lambda_2, \ldots, \lambda_N)\\ &= \prod_{j=1}^{N} \int_{-1}^{1} \frac{\mathrm{e}^{ia_j sy}}{\pi\lambda_j\sqrt{1-y^2}} \left\{\sqrt{2\pi}\, \mathrm{e}^{-(\arccos y)^2/(2\lambda_j^2)} - \lambda_j\, \mathrm{erf}\left(\pi/(\lambda_j\sqrt{2})\right) + \lambda_j\right\} \mathrm{d}y\end{aligned} \tag{3.3}$$

The equal sign in Eq. (3.1) dictates that the extreme value distribution of the target Gaussian random process should be equal to that of the extreme value distribution that DLG generates. The question mark on top of the equal sign appeared in Eq. (2.30) is temporarily removed, but will be discussed again in Sec. 3.3.

The left-hand side of the governing equation ψ_{X_m} defined in Eq. (3.2) is the characteristic function of the extreme value distribution of a zero-mean Gaussian random process with variance σ^2, while the right-hand side of the governing equation $\psi_{X'_m}$ as defined in Eq. (3.3) is the characteristic function of the extreme value distribution that the DLG process would generate when the phase angles are sampled according to the modified Gaussian distribution determined by $\boldsymbol{\lambda}$. The set of parameters $\boldsymbol{\lambda}$ is the unknown to be solved in Eq. (3.1) and defined as

$$\boldsymbol{\lambda} = (\lambda_1, \lambda_2, \ldots, \lambda_N) \tag{3.4}$$

On the other hand, the parameters m, σ and $\boldsymbol{a}$ are all inputs to DLG and completely determined once the output spectrum and TEV are both known. The set of input Fourier coefficients $\boldsymbol{a}$ is defined as

$$\boldsymbol{a} = (a_1, a_2, \ldots, a_N) \tag{3.5}$$

To date, the question of whether there exists a solution—and further a unique solution—to Eq. (3.1) has not been answered. As an alternative to solving this governing equation analytically, Alford (2008) utilized an optimization routine to find $\boldsymbol{\lambda}$ that minimizes the L1 norm of the difference between ψ_{X_m} and $\psi_{X'_m}$ of Eq. (3.1) at a finite number of points on the s axis. In other words, the objective function (or cost function) used in Alford (2008) was

$$f_{\text{objective}} = \sum_{k=1}^{N_s} \left| \psi_{X_m}(s_k; m, \sigma) - \psi_{X'_m}(s_k; \boldsymbol{a}, \boldsymbol{\lambda}) \right| \tag{3.6}$$

where s was discretized between $-s_{\max}$ and $s_{\max}$ and the maximum N_s applied was set at 101 due to time constraints. In addition, $s_{\max}$ was set at $4\pi/x_{\max}$, where $x_{\max}$ was determined by Eq. (2.6). When ψ_{X_m} and $\psi_{X'_m}$ are calculated inside the optimization[1], Alford (2008) applied a standard trapezoidal integration scheme. In the application of the trapezoidal integration, special care had to be taken to handle the singularity at $y = -1$ and $y = +1$ in $\psi_{X'_m}(s)$.

The optimization routine did not succeed in finding $\boldsymbol{\lambda}$ that satisfies the equality condition in Eq. (3.1). The biggest reason is due to the fact that the *inid* assumption from which Eq. (3.1) has been derived is not entirely correct. This means that the extreme responses from Alford (2008) could not perfectly follow the theoretical extreme value distribution of the Gaussian random variable. Although the optimal solution from the optimization did generate only an approximate distribution, the mean of which was very close to the mean of the theoretical extreme value distribution, the mismatch in the tail regions made it almost impossible to assess the risk associated with the use of the extreme value distribution from this process as a design value. The other shortcoming was that it took a great deal of time (on the order of a few hours when $N = N_s = 101$) to obtain the approximate distribution using

[1]From this point on, in expressing ψ_{X_m} and $\psi_{X'_m}$, the parameters, i.e., m, σ, $\boldsymbol{a}$, and $\boldsymbol{\lambda}$, will be omitted for simplification, unless required for clarity.

the optimization routine. This is partly due to the characteristics of the problem—nonlinear and multidimensional. Moreover, as the number of wave coefficients N increased, the computation time needed to achieve a consistent level of accuracy increased significantly. More specifically, the fact that the computation of $\psi_{X'_m}$ required a considerable amount of time presented difficulties in increasing N and N_s. Overcoming the aforementioned shortcomings in Alford (2008) is one of the aims of the current research.

3.2 A New Approach

In the current research, the complexity of $\psi_{X'_m}$ is first reduced to increase the efficiency of the computation. As can be seen in Eq. (3.3), $\psi_{X'_m}$ is the multiplication of N functions, each of which consists of three components. Although highly nonlinear, these three components can be simplified by introducing a new variable θ such that $y = \cos\theta$. Specifically,

$$\begin{aligned}\int_{-1}^{1} \frac{e^{ia_j sy} e^{-(\arccos y)^2/(2\lambda_j^2)}}{\sqrt{1-y^2}}\,\mathrm{d}y &= \int_{\pi}^{0} \frac{e^{ia_j s\cos\theta} e^{-\theta^2/(2\lambda_j^2)}}{\sqrt{1-\cos^2\theta}}(-\sin\theta)\,\mathrm{d}\theta \\ &= \int_{0}^{\pi} e^{ia_j s\cos\theta} e^{-\theta^2/(2\lambda_j^2)}\,\mathrm{d}\theta \end{aligned} \tag{3.7}$$

$$\begin{aligned}\int_{-1}^{1} \mathrm{erf}\left(\frac{\pi}{\lambda_j\sqrt{2}}\right)\frac{e^{ia_j sy}}{\sqrt{1-y^2}}\,\mathrm{d}y &= \mathrm{erf}\left(\frac{\pi}{\lambda_j\sqrt{2}}\right)\int_{\pi}^{0} \frac{e^{ia_j s\cos\theta}}{\sqrt{1-\cos^2\theta}}(-\sin\theta)\,\mathrm{d}\theta \\ &= \pi\mathrm{erf}\left(\frac{\pi}{\lambda_j\sqrt{2}}\right) J_0(a_j s) \end{aligned} \tag{3.8}$$

$$\begin{aligned}\int_{-1}^{1} \frac{e^{ia_j sy}}{\sqrt{1-y^2}}\,\mathrm{d}y &= \int_{\pi}^{0} \frac{e^{ia_j s\cos\theta}}{\sqrt{1-\cos^2\theta}}(-\sin\theta)\,\mathrm{d}\theta \\ &= \int_{0}^{\pi} e^{ia_j s\cos\theta}\,\mathrm{d}\theta = \pi J_0(a_j s) \end{aligned} \tag{3.9}$$

In the derivation of Eq. (3.8) and Eq. (3.9), the following definition of the first kind Bessel function $J_n(z)$ is utilized:

$$J_n(z) = \frac{i^{-n}}{\pi}\int_{0}^{\pi} e^{iz\cos\theta}\cos(n\theta)\,\mathrm{d}\theta \tag{3.10}$$

In addition, the application of an adaptive trapezoidal scheme allows Eq. (3.7) to be evaluated very accurately and efficiently. Moreover, the error function and the Bessel function in Eq. (3.8) and Eq. (3.9) can be computed using the standard library of any computational program. These modifications of $\psi_{X'_m}(s)$ greatly improve the efficiency of the computation of $\psi_{X'_m}(s)$.

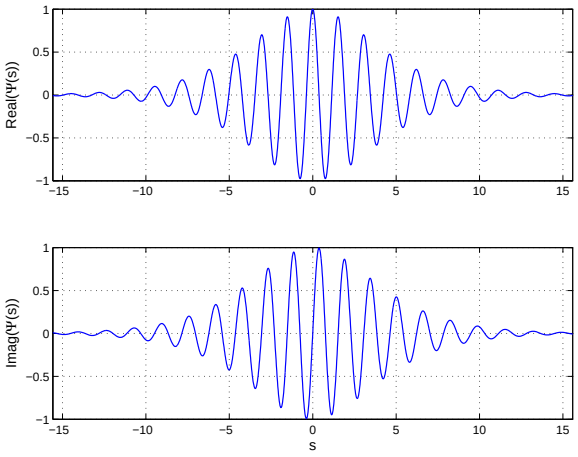

(a) TEV = 4.0, $\sigma = 1$

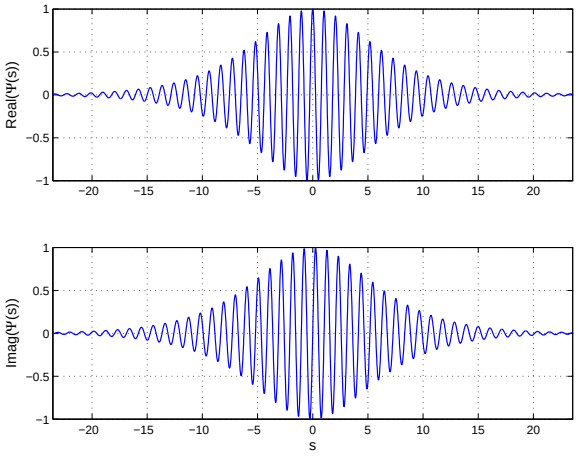

(b) TEV = 6.0, $\sigma = 1$

Figure 3.1: Example Characteristic Functions (ψ_{X_m}) of Extreme Value Distribution of Gaussian Process

Meanwhile, ψ_{X_m} is the characteristic function of the Gaussian extreme value distribution, which is a complex-valued function. This function can be efficiently calculated using a Fast Fourier Transform (FFT). Fig. 3.1 shows two examples of ψ_{X_m}, which suggest that the domain of s may be truncated at a certain level that depends on m.

In the current research, this level, termed as $s_{\text{threshold}}$, is set to be a point on the s axis, where the $|\psi_{X_m}|$ becomes less than 0.01.

The characteristic function of a random variable X defined by Eq. (2.28) always exists since $|e^{isX}|$ is a continuous and bounded function for all finite real values of s and X. In addition, the characteristic function has the following properties:

1. $\psi(0) = 1$
2. $|\psi(s)| \leq 1$
3. $\psi(-s) = \psi^*(s)$, where $\psi^*(s)$ denotes the complex conjugate of $\psi(s)$.

These properties are readily confirmed in Fig. 3.1. Due to the last property, considering only the positive s-domain reduces the computational workload by half again, compared to Alford (2008).

All of the aforementioned improvements contribute to the significant reduction in the computation time in the optimization routine, but they still do not remove the shortcoming that the extreme response from DLG failed to closely follow the theoretical extreme value distribution, or do not find the solution of Eq. (3.1) with an acceptable accuracy.

3.3 Existence of Solutions

The existence and the uniqueness of the solution of Eq. (3.1) are not clear at all, and a rigorous investigation is beyond the scope of this research. However, the graphical investigation of Eq. (3.1) can present a useful insight on this matter. For this purpose, a zero-mean Gaussian process with unit variance is considered without loss of generality. Because of the unit variance, Eq. (2.4) becomes

$$\sum_{j=1}^{N} a_j^2 = 2$$

which suggests that the maximum value a_j can take is $\sqrt{2}$ for a perfectly narrow banded process. As shown in Fig. 3.2, however, a_j is usually much smaller than $\sqrt{2}$ for the normalized case, depending on the broadness parameter or the number of Fourier coefficients. In Fig. 3.2, the number of Fourier coefficients N is 301.

For this normalized case, the summation of Eqs. (3.7) $\sim$ (3.9) for a few possible a_j and λ_j is illustrated in Fig. 3.3. The summation may be seen as a basis function of $\psi_{X'_m}(s)$, because the summation is $\psi_{X'_m}(s)$ when $N = 1$. Note also that the three

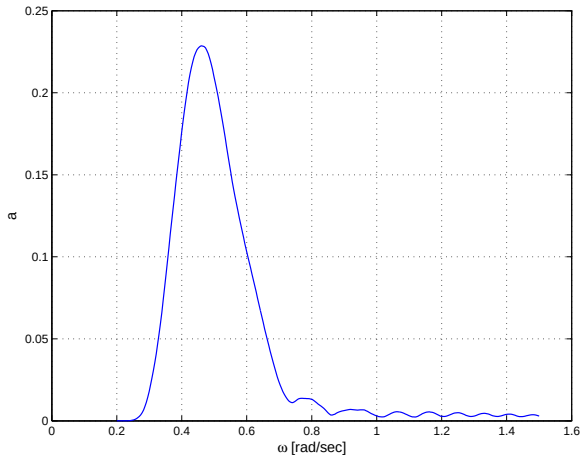

Figure 3.2: Example Set of Fourier Coefficients $\boldsymbol{a}$

properties of the characteristic function explained in the previous section are readily confirmed visually in Fig. 3.3.

At this point, Eq. (3.1) may be re-formulated to find $\boldsymbol{\lambda}$ such that the multiplication of N basis functions comes as close as possible to the known ψ_{X_m} of Eq. (3.1). However, a closer observation of Fig. 3.3 reveals that as λ_j and s increase, the basis functions decrease significantly. In addition, these basis functions are all less than 1, which means that $\psi_{X'_m}$ will decay very fast as N increases. Specifically,

$$|\psi_{X'_m}| \to 0 \quad \text{even when} \quad s \ll s_{\text{threshold}} \tag{3.11}$$

which strongly suggests that the existence of $\boldsymbol{\lambda}$ that satisfies the equality condition in Eq. (3.1) is not guaranteed. This line of reasoning is confirmed in Fig. 3.4, which shows a ψ_{X_m}, labeled as THEORY, for two different TEV cases of the Gaussian random process expressed by $\boldsymbol{a}$ in Fig. 3.2. Plotted simultaneously is $\psi_{X'_m}$, labeled as MCS and calculated based on $\boldsymbol{\lambda}$ obtained from the curve fitting of phase angles to the modified Gaussian distribution. The phase angles are associated with X'_m defined in Sec. 2.4. When s is around the origin, the comparison is very good. As s increases, however, $\psi_{X'_m}$ quickly diminishes to zero, while ψ_{X_m} slowly decays oscillating around zero. The discrepancy is due to the fact that the phase angles associated with the maximum in m samples are assumed to be *inid* in the calculation of $\psi_{X'_m}$. Limited simulations indicate that the phase angles are not exactly independent. On the contrary, they are slightly dependent. But the use of a multivariate phase PDF to resolve the discrepancy is not a viable option, because as N increases the amount of computation to identify

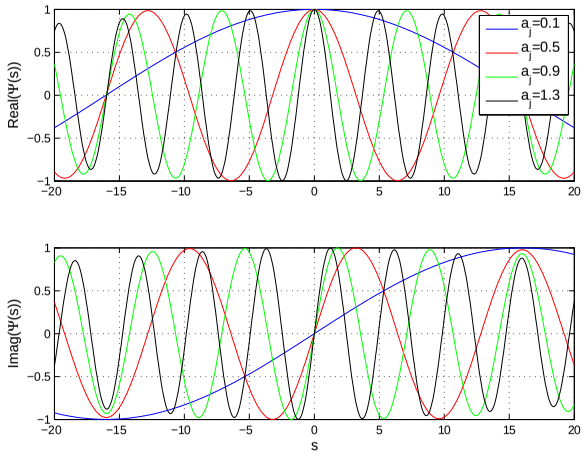

(a) $\lambda_j = 0.2$

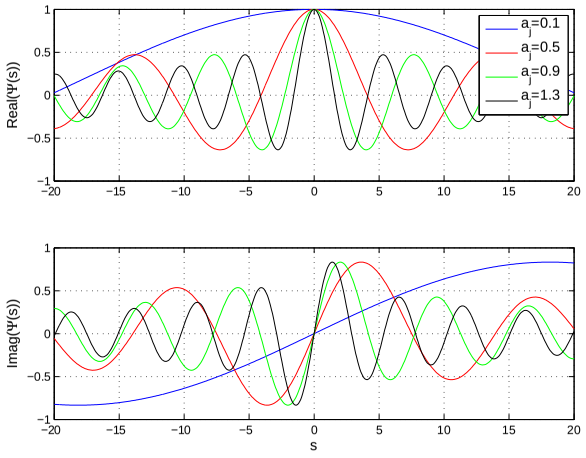

(b) $\lambda_j = 0.8$

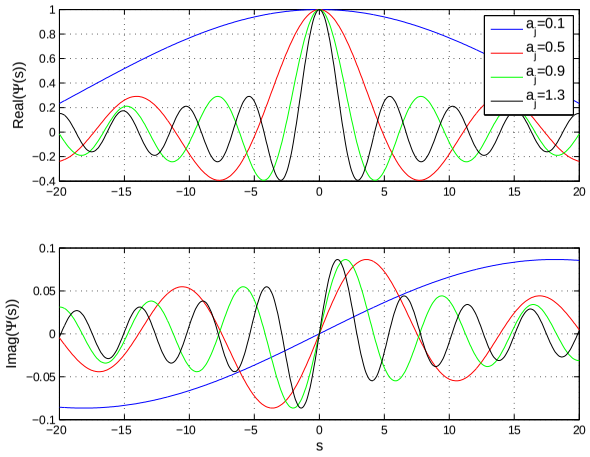

(c) $\lambda_j = 3.0$

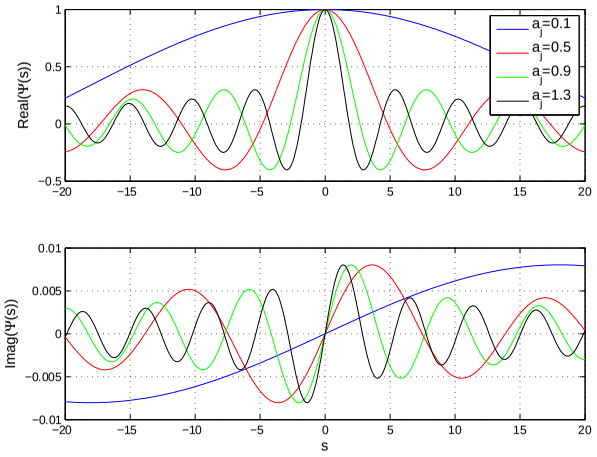

(d) $\lambda_j = 7.0$

Figure 3.3: Examples Characteristic Functions ($\psi_{X'_m}$) [$N = 1$]

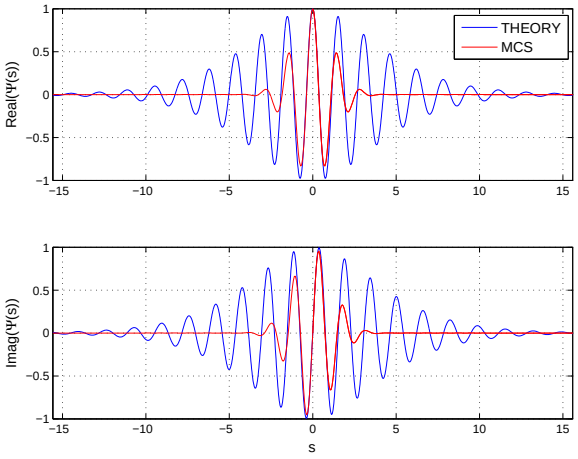

(a) TEV = 3.0

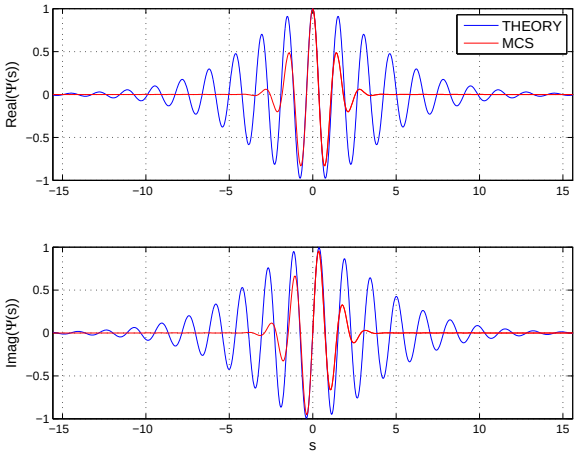

(b) TEV = 4.0

Figure 3.4: Example Comparisons: Characteristic Function of Theoretical Extreme Value Distribution of Standard Normal Distribution (ψ_{X_m}) and Characteristic Function of Corresponding Empirical Extreme Value Distribution from Monte Carlo Simulations ($\psi_{X'_m}$)

the phase PDF will become astronomical, not to mention the increased complexity in handling the new characteristic function.

The effect of the discrepancy on the extreme value PDF is illustrated again in Fig. 3.5. For this figure, $N_{\text{runs}} \times m \times N$ uniformly distributed random phase angles were generated first to find X'_m in Eq. (2.24). The N_{runs}, m and N used were 50000, 31574, and 201, respectively. Note that $m = 31574$ corresponds to TEV $= 4$. Although the comparison is somewhat worse than is seen in Fig. 2.2 due to a finite and

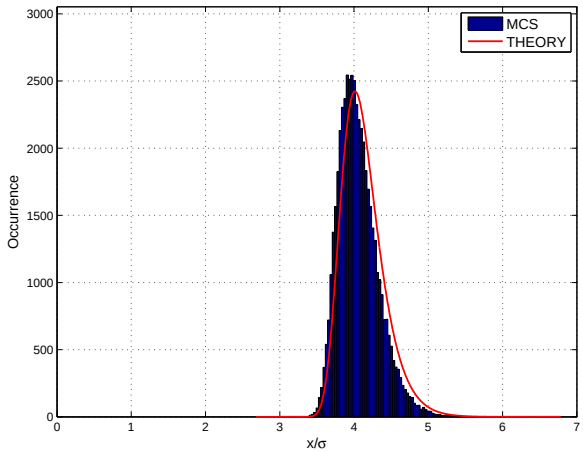

(a) Example Comparison between Empirical Extreme Value Distribution (MCS) and Theoretical Extreme Value Distribution (THEORY)

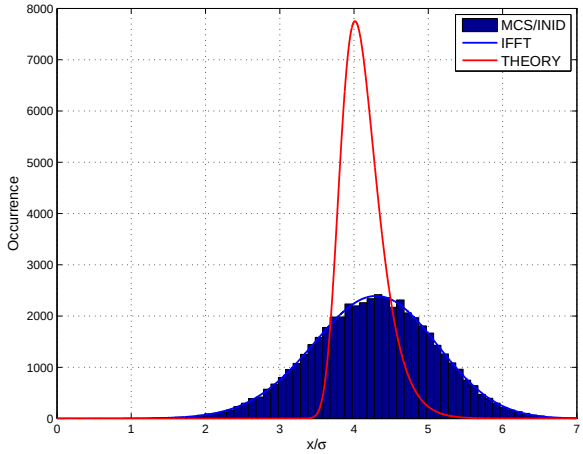

(b) Reconstructions of Extreme Value Distribution based on $\boldsymbol{\lambda}$ from Empirical Extreme Value Distribution (MCS/INID, IFFT)

Figure 3.5: Effect of *inid* Assumption

"insufficiently" large N, the histogram of X'_m still matches relatively well with that of the theoretical extreme value distribution as shown in Fig. 3.5(a). The matching will improve further as N increases for the reason detailed in Appendix A.

As stated previously, the fundamental idea behind DLG is to construct the extreme value distribution based on the distributions of the associated phase angles. In order to identify these phase distributions associated with X'_m, the method of least squares was used to find the optimized $\boldsymbol{\lambda}$, based on the *inid* assumption, such that the squared

difference between the modified Gaussian distribution defined by Eq. (2.26) and the distribution of E_{m_j} in Eq. (2.25) is at its minimum.

If the *inid* assumption is to reveal the truth about E_{m_j}, the random phase angles generated by Eq. (2.26) using the optimized $\boldsymbol{\lambda}$ should recover the original extreme value distribution shown in Fig. 3.5(a) within the error introduced by applying the least square method. However, the distribution from this recovery process (MCS/INID), as shown in Fig. 3.5(b), is much wider compared to the extreme value distribution of a Gaussian random variable (THEORY) of the same variance, where the N_{runs}, m and N used are identical to those in Fig. 3.5(a). In other words, the distributions of extreme values are quite different, even though the distributions of the phase angles are almost identical when expressed according to the *inid* assumption. Fig. 3.5(b) also shows the distribution directly calculated from the inverse Fourier Transform (IFFT) of $\psi_{X'_m}$ based on the optimized $\boldsymbol{\lambda}$. The fact that MCS/INID and IFFT match perfectly in Fig. 3.5(b) indirectly confirms the accuracy of the developments made in Sec. 3.3.

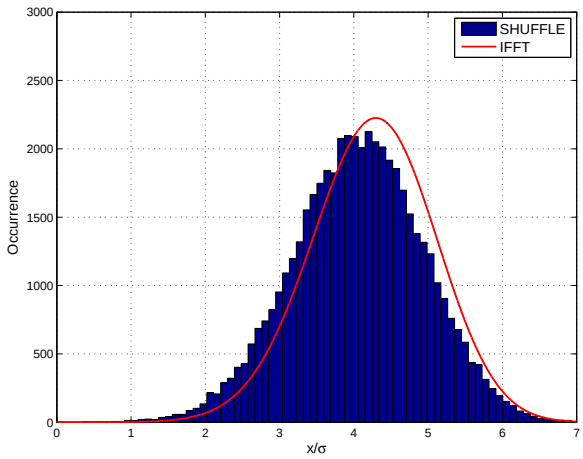

Figure 3.6: Evidence of Not Entirely Correct *inid* Assumption

Other evidence that the *inid* assumption is not entirely correct is presented in Fig. 3.6. In order to generate this figure, the phase angles collected from MCS in Fig 3.5(a) are shuffled randomly for each ω_j. This shuffling process should not change the distribution of E_{m_j} determined from the method of least squares. Specifically, designated as SHUFFLE in Fig. 3.6 is the extreme value distribution reconstructed from the shuffled phase angles, while IFFT is copied from Fig. 3.5(b). If *inid* is the correct hypothesis, the extreme value distribution reconstructed from the shuffled

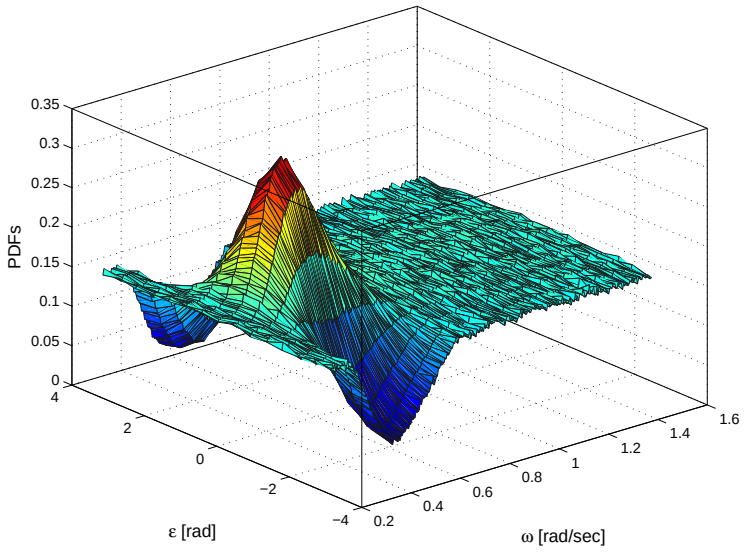

(a) Phase PDFs Associated with Empirical Extreme Value Distribution (MCS)

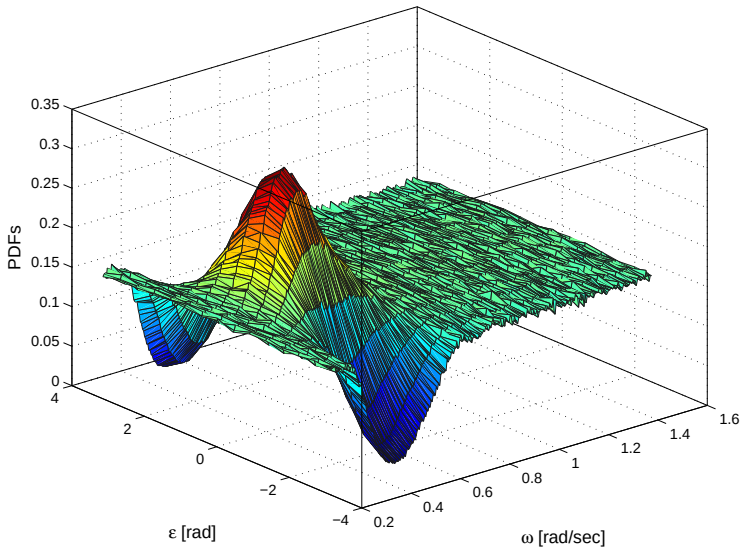

(b) Phase PDFs Utilized in Reconstruction of Extreme Value Distribution based on $\boldsymbol{\lambda}$ from Empirical Extreme Value Distribution (MCS/INID)

Figure 3.7: Approximation of Phase PDFs using Modified Gaussian Distribution

phase angles should recover the distribution identical to MCS in Fig. 3.5(a). But this is not the case, which again shows that the *inid* assumption is not entirely correct. The statement that *inid* is not "entirely" correct reflects the fact that, at the very

least, the mean values of SHUFFLE and IFFT are very close. For example, this assumption reflects reality more closely than the assumption that the phase angles are independent and identically distributed (*iid*) (Alford, 2008).

The difference between SHUFFLE and IFFT is most likely due to the approximation of phase angles using the modified Gaussian distribution. For example, Fig. 3.7(a) is the collection of the PDFs of E_{m_j} based on the sets of phase angles associated with X'_m from MCS, while Fig. 3.7(b) is the collection of the phase PDFs based on the sets of phase angles used in the reconstruction of MCS/INID in Fig. 3.5(b).[2] Although they look almost identical, there exists a deviation between the two figures when λ_j is small. The use of the least squares method to find the best fit from a finite number of phase samples is a salient issue, too.

As mentioned, there exists a significant deviation between MCS/INID (or IFFT) and THEORY in Fig. 3.5. When an optimization routine, instead of the Monte Carlo simulation, is applied, the comparison may be improved, as evidenced in Alford (2008). However, it will not be sufficient for obtaining an acceptable match in the tail regions of two PDFs. Naturally, how to fill this gap is the topic of next section. Specifically, a systematic approach to filtering out the sets of phase angles generated by the *inid* assumption such that they match well needs to be devised.

3.4 Acceptance-Rejection Algorithm

The Acceptance-Rejection (A-R) method is a scheme popular in probability theory and related fields, but it has never been given due attention in the fields of naval architecture and marine engineering. This algorithm, as explained in, for example, von Neumann (1951), is a powerful tool that can be a foundation for designing a numerical random number generator, when the inverse of the CDF of the target random variable is not available as an explicit form. Before elaborating how this scheme can be modified to remove the discrepancy due to the *inid* assumption, the standard A-R algorithm is explained first.

Assume that a numerical random number generator needs to be constructed to sample a random variable X, of which PDF is $f_X(x)$. If another random variable Y, of which PDF is $g_Y(x)$, can be sampled efficiently, and the condition that $f_X(x) \leq cg_Y(x)$ for some c and all x is satisfied, as shown in Fig. 3.8, then the A-R method can be applied in the following steps:

[2]The PDFs are prepared as if E_{m_j} is a continuous random variable, when the construction of the phase PDFs are done in a discrete sense. Note also that the PDFs in Fig. 3.7 are not the joint PDFs of ϵ and ω, but the PDFs of ϵ for each ω.

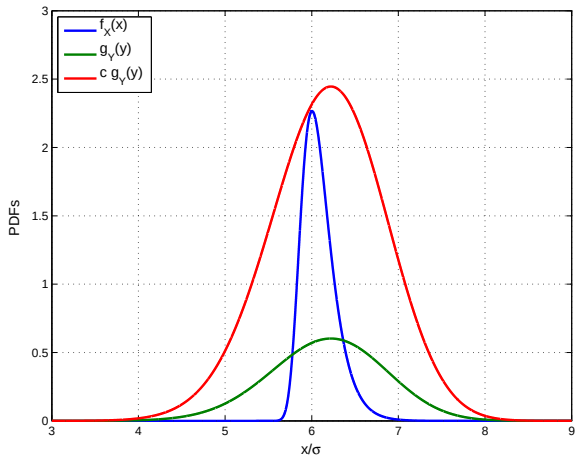

Figure 3.8: Schematic of Acceptance-Rejection Method [$c = 4.0614$]

1. Generate a random sample y from the random variable Y generator and a uniform random number u from $U(0,1)$. Note that $U(a,b)$ is a uniformly distributed random variable between a and b.

2. If $u \leq f_X(y)/cg_Y(y)$, accept y as a sample x from the random variable X. If not, return to the first step.

What needs to be proved in order to show that this procedure works as a random number generator of X is

$$P\{X \leq x\} = P\{Y \leq x \Big| U \leq f_X(y)/cg_Y(y)\} \tag{3.12}$$

Since Y and U are independent, the joint PDF of Y and U, which may be designated as $h_{Y,U}(y,u)$, can be expressed as

$$h_{Y,U}(y,u) = g_Y(y) \cdot 1 = g_Y(y) \tag{3.13}$$

In addition, by definition of the conditional probability, the right hand side of Eq. (3.12) is expressed using Eq. (3.13) as

$$P\{Y \leq x \Big| U \leq f_X(y)/cg_Y(y)\} = \Big[\int_{y \leq x} \int_{0 \leq u \leq f_X(y)/cg_Y(y)} g_Y(y) \mathrm{d}u\mathrm{d}y \Big] / K \tag{3.14}$$

where the denominator K is, by definition, the probability of a selected uniform

random number u satisfying $u \leq f_X(y)/cg_Y(y)$, which is

$$K = P\{U \leq f_X(y)/cg_Y(y)\} \tag{3.15}$$

Since the numerator of Eq. (3.14) can be simplified as

$$\begin{aligned}\int_{y\leq x}\int_{0\leq u\leq f_X(y)/cg_Y(y)} g_Y(y)\mathrm{d}u\mathrm{d}y &= \int_{-\infty}^{x}\int_{0}^{f_X(y)/cg_Y(y)} \mathrm{d}u g_Y(y)\mathrm{d}y \\ &= \int_{-\infty}^{x}\Big(f_X(y)/cg_Y(y)\Big)\cdot g_Y(y)\mathrm{d}y \\ &= (1/c)\int_{-\infty}^{x} f_X(y)\mathrm{d}y \end{aligned} \tag{3.16}$$

Eq. (3.12) becomes

$$P\{X \leq x\} = (1/cK)\int_{-\infty}^{x} f_X(y)\mathrm{d}y \tag{3.17}$$

Therefore, Eq. (3.17) is true if and only if

$$K = 1/c \tag{3.18}$$

The proof of Eq. (3.18) is readily available by applying the total probability theorem to Eq. (3.15).

$$\begin{aligned} K &= P\{U \leq f_X(y)/cg_Y(y)\} \\ &= \int_{-\infty}^{\infty} P(U \leq f_X(y)/cg_Y(y)\Big|Y = y)\cdot g_Y(y)\mathrm{d}y \\ &= \int_{-\infty}^{\infty}\Big(f_X(y)/cg_Y(y)\Big)\cdot g_Y(y)\mathrm{d}y = 1/c \end{aligned} \tag{3.19}$$

The number of iterations needed to collect the required number of realizations (m_r), designated as N_i, is a geometric random variable with the success probability $1/c$, as implied in Eq. (3.19). Hence, the expected value of N_i is m_r times c, which indicates that the constant c should be maintained as low as possible to minimize the expense of the A-R method.

The similarity between Fig. 3.5 and Fig. 3.8 strongly suggests that the approximated extreme value distribution based on the *inid* phase distribution can be a perfect candidate for $g_Y(x)$, while the extreme value distribution that DLG should generate is $f_X(x)$. In other words, the acceptance-rejection algorithm explained above can be implemented in DLG according to the following sequence:

1. Generate a random sample y from the random variable Y generator by producing a set of phase angle ϵ'_j that follows the modified Gaussian distribution based on $\boldsymbol{\lambda}$ that satisfies Eq. (3.1) approximately, and a uniform random number u from $U(0,1)$.

2. If $u \leq f_X(y)/cg_Y(y)$, accept y as a sample x from the random variable X and store the associated set of phase angle ϵ'_j. If not, return to the first step.

3. Repeat the above two steps until m_r sets of N phase angles are collected.

The question then arises whether the random variable Y generator is inexpensive. In other words, how can the sets of phase angle ϵ'_j be generated efficiently, given a_j and m? Before answering this question, it is necessary to address how to determine $g_Y(y)$ for an arbitrary target event with a given exposure time m.

3.5 Determination of $g_Y(y)$

The first task to utilize the A-R scheme is to determine $g_Y(y)$ in Fig. 3.8. For a small m, Monte Carlo simulations (MCS) are the fastest way to obtain $\boldsymbol{\lambda}$ from which $g_Y(y)$ can be calculated, as presented in Sec. 3.3. However, as m (or equivalently TEV) increases, the computation time will increase exponentially, which defeats the purpose of DLG and the A-R method.

A second option is to apply an optimization routine (OPT). As demonstrated by Alford (2008), OPT would generate $g_Y(y)$. However, this is still a time-consuming approach even with the improvements introduced in Sec. 3.1. Specifically, it is not clear how to increase m and N in the optimization without sacrificing the speed of the computation. What is very interesting is the combination of the first and the second option offers a viable solution. Assume that $g_Y(y)$ for a 6σ event (Target) is required. Finding $\boldsymbol{\lambda}$ that would generate $g_Y(y)$ from either MCS or OPT requires a significant amount of time. However, MCS for a 3σ event (Initial) can be done in a fraction of the time that the 6σ event would require, based on which an optimization problem can be formulated to determine $\boldsymbol{\lambda}$ for the 6σ event. Specifically, the characteristic function of 3σ can then be translated, in the s domain, using the shift property of

the Fourier transform:

$$\begin{aligned}\psi_{X'_m}(s)\Big|_{\text{Target}} &= \int_{-\infty}^{\infty} \mathrm{e}^{isx} f_{X'_m}(x - x_o)\,\mathrm{d}x \\ &= \int_{-\infty}^{\infty} \mathrm{e}^{is(x+x_o)} f_{X'_m}(x)\,\mathrm{d}x \\ &= \mathrm{e}^{isx_o}\,\psi_{X'_m}(s)\Big|_{\text{Initial}}\end{aligned} \tag{3.20}$$

where

$$x_o = \text{TEV}\Big|_{\text{Target}} - \text{TEV}\Big|_{\text{Initial}} \tag{3.21}$$

The objective of this translation is, of course, to find $g_Y(y)$ suitable for the target TEV event. An example of the characteristic function of $g_Y(y)$ calculated for the 6σ event by multiplying e^{isx_o} by the characteristic function of the 3σ event is presented in Fig. 3.9(a). In this figure, the deviation between the characteristic function of the 6σ theoretical extreme value PDF and the PDF translated to the 6σ event exists, too. However, as Fig. 3.9(b) shows, the shifted $g_Y(y)$ satisfies, for some c and all x, the necessary condition for applying the A-R method:

$$f_X(x) \le c g_Y(x) \tag{3.22}$$

A natural question then arises as to how big the difference would be between the characteristic function of $g_Y(y)$ for a higher TEV event from the shift property and the characteristic function for the higher TEV event from MCS alone. In Fig. 3.10(a), the characteristic function for a 3.0σ event from MCS is shifted to a 4.5σ event to be compared with that of a 4.5σ event obtained purely from MCS. They match relatively well. In Fig. 3.10(a), the characteristic function for a 4.0σ event from MCS is shifted to a 4.5σ event to be again compared with that of a 4.5σ event from pure MCS. The general matching becomes slightly better. Although this near-equivalency between SHIFT and MCS is expected to become weaker as x_o in Eq. (3.21) increases, the "mismatch" will not be a problem at all, because SHIFT will only be used as a target characteristic function of the optimization. Moreover, the optimization will find the set of lambda that will be much closer to MCS than SHIFT, which will be presented in Sec. 3.6.

The shift property is not directly validated against MCS for a much higher TEV event (e.g., 5.0σ or 6.0σ event) due to prohibitive cost. For example, the number of random samples m to be generated for a 5.5σ event alone is about 180 times more than that of a 4.5σ event for the same N_{runs} and N, as listed in Table 2.1. The increase

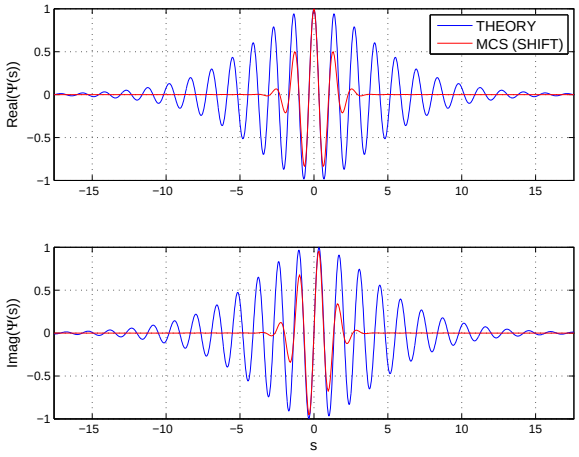

(a) Transformation of Characteristic Function of 3σ Event from Monte Carlo Simulations to that of 6σ Event, Compared to Theoretical Characteristic Function of 6σ Event

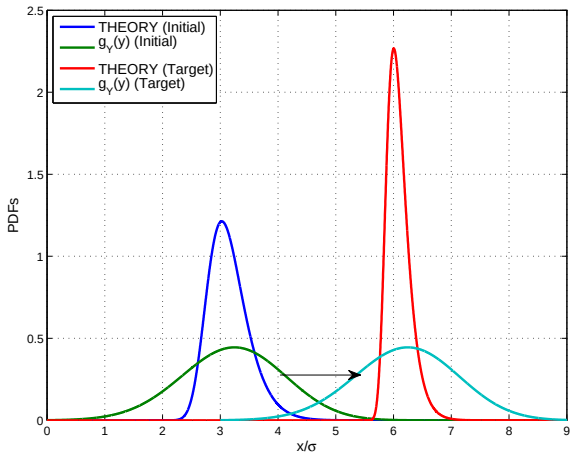

(b) Example SHIFT of 3σ Event to 6σ Event

Figure 3.9: Summary of Strategy to Find $g_Y(y)$ for Target TEV

in the computational cost due to the memory management will also be significant.

The remaining issue is how to find a new $\boldsymbol{\lambda}$ that will generate the shifted $g_Y(y)$. It is unclear whether the new $\boldsymbol{\lambda}$ associated with the translated 6σ event can be obtained analytically by comparing Eq. (3.3) and Eq. (3.20). However, as stated before, it is possible to convert the problem to a typical optimization problem where the new $\boldsymbol{\lambda}$ is calculated using an empirical relation between $\boldsymbol{a}$ and $\boldsymbol{\lambda}$. Specifically, this will be done by utilizing the relation between $\boldsymbol{a}$ and $\boldsymbol{\lambda}$ as TEV varies.

Before explaining the optimization using the empirical relation, the strategy ex-

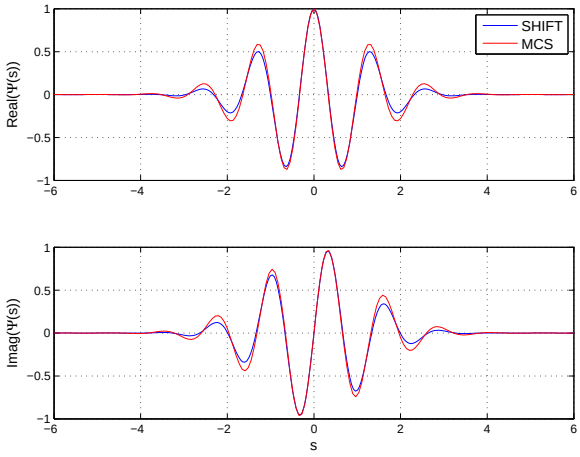

(a) SHIFT ($3.0\sigma \rightarrow 4.5\sigma$) vs. MCS ($4.5\sigma$)

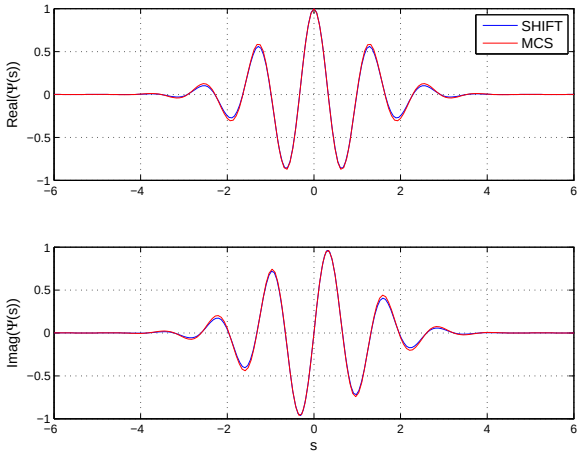

(b) SHIFT ($4.0\sigma \rightarrow 4.5\sigma$) vs. MCS ($4.5\sigma$)

Figure 3.10: Difference between Characteristic Function from Monte Carlo Simulations (MCS) and Characteristic Function from the Shift Property of Fourier Transform (SHIFT)

plained above may be summarized as

$$\boldsymbol{\lambda}_{\text{Initial}} \rightarrow g_Y(y)\Big|_{\text{Initial}} \rightarrow \text{SHIFT} \rightarrow g_Y(y)\Big|_{\text{Target}} \rightarrow \boldsymbol{\lambda}_{\text{Target}}$$

In other words, $\boldsymbol{\lambda}_{\text{Initial}}$ can be estimated based on MCS for a low TEV case initially (e.g., TEV=3), from which $g_Y(y)$ for the initial TEV can be calculated. Using the shift property of the Fourier transform, the initial $g_Y(y)$ can be translated to a new $g_Y(y)$ for the target TEV (e.g., TEV=6). How to calculate $\boldsymbol{\lambda}$ for the higher target

TEV (or $\boldsymbol{\lambda}_{\text{Target}}$) from the target $g_Y(y)$ will be the topic of the next section.

3.6 Optimization of $\boldsymbol{\lambda}$

The relation between $\boldsymbol{a}$ and $\boldsymbol{\lambda}$ for a few different TEVs is sought in this section. The objective of this investigation is to find whether $\boldsymbol{\lambda}$ for a higher TEV can be estimated based $\boldsymbol{\lambda}$ for a lower TEV. In the discussion below, instead of $\boldsymbol{a}$ and $\boldsymbol{\lambda}$, a_j and λ_j will be used where necessary to refer to each object in sets, because the relation between each object in $\boldsymbol{a}$ and $\boldsymbol{\lambda}$ is of interest.

In order to reveal the relation more clearly, two different sets of a_j are prepared, as shown in Fig. 3.11. The number of Fourier coefficients used to discretize ω is 201. The selection of two symmetric sets of a_j is intended to reveal the one-to-one relation between a_j and λ_j for a fixed TEV, where j can take any value between 1 and N.

For each set of a_j given in Fig. 3.11, the corresponding set of λ_j is calculated using MCS, as presented in Fig. 3.12(a) and Fig. 3.12(b), which shows the convergence of λ_j as N_{runs} increases. A few important tendencies are readily observed. First of all, as a_j increases, λ_j decreases. Second, the convergence rate is lower for a smaller a_j. Third, when two a_j are identical, two corresponding λ_j are very close, as can be seen, e.g., for two identical a_j at 0.8 [rad/sec] and 1.2 [rad/sec]. The very minor difference is considered to be due to the the random nature of the results. Last, but most important, the set of λ_j moves downward evenly, while maintaining its original shape as TEV increases, which is shown Fig. 3.12(c) and Fig. 3.12(d). This tendency is becoming somewhat weak as λ_j increases (or a_j decreases). However, this is expected because the modified Gaussian distribution does not change significantly as λ_j increases (say λ_j larger than 3), which was shown in Fig. 2.3.

This last tendency has a profound implication: it shows that a simple parameter λ_o can be introduced to find the set of new λ_j for the target TEV from the set of the initial λ_j. In other words, the problem now becomes a much simpler optimization where the objective function is to find the offset λ_o that minimizes the L2 norm of the difference between two corresponding characteristic functions for the target TEV event:

$$g_{\text{objective}}(\lambda_o) = \left[\sum_{k=1}^{N_s} \left| \mathrm{e}^{is_k x_o} \psi_{X'_m}(s_k; \boldsymbol{a}, \boldsymbol{\lambda}_{\text{Initial}}) - \psi_{X'_m}(s_k; \boldsymbol{a}, \boldsymbol{\lambda}_{\text{Initial}} - \boldsymbol{\lambda}_o) \right|^2 \right]^{1/2} \tag{3.23}$$

subject to

$$0 < \lambda_o < \min(\boldsymbol{\lambda}_{\text{Initial}}) \tag{3.24}$$

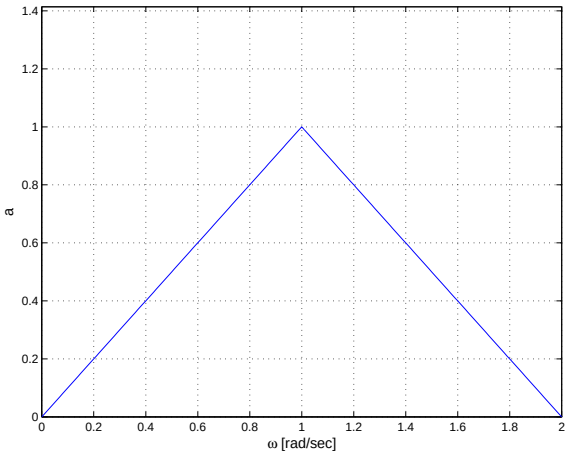

(a) Triangular Case

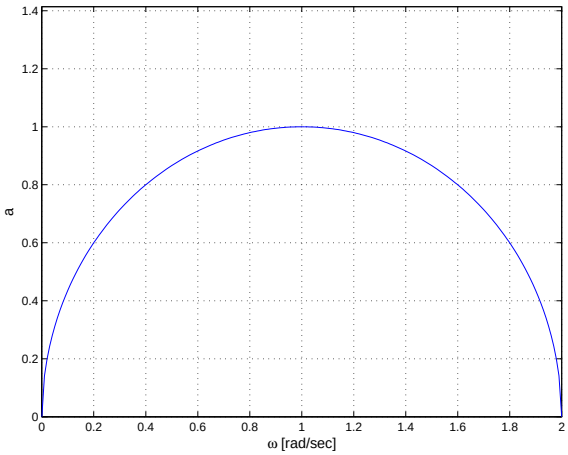

(b) Circular Case

Figure 3.11: Example Sets of Fourier Coefficients $\boldsymbol{a}$

where x_o is from Eq. (3.21), $\boldsymbol{\lambda}_{\text{Initial}}$ is from MCS for the initial TEV, $\boldsymbol{\lambda}_o$ is $(\lambda_o, \lambda_o, \ldots, \lambda_o)$, s is discretized between 0 and $s_{\text{threshold}}$, and N_s is typically around $40 \sim 60$ depending on TEV. Unlike $f_{\text{objective}}$ in Eq. (3.6), $g_{\text{objective}}$ in Eq. (3.23) is a single-variable optimization problem, which can be solved straightforwardly. The optimal λ_o from Eq. (3.23) can then be used to find the set of λ_j for the target TEV event.

$$\boldsymbol{\lambda}_{\text{Target}} = \boldsymbol{\lambda}_{\text{Initial}} - \boldsymbol{\lambda}_o \Big|_{\text{optimal}} \tag{3.25}$$

Fig. 3.13 shows the result of this optimization applied to two different cases: 4.5 and 6.0σ cases of the process defined by the Fourier coefficients shown in Fig. 3.2.

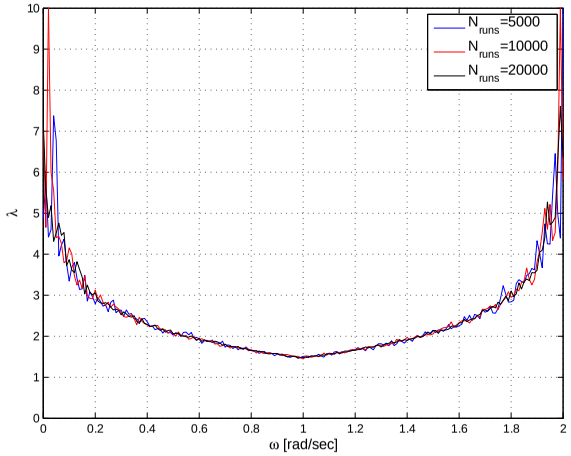

(a) Triangular Case (TEV = 4)

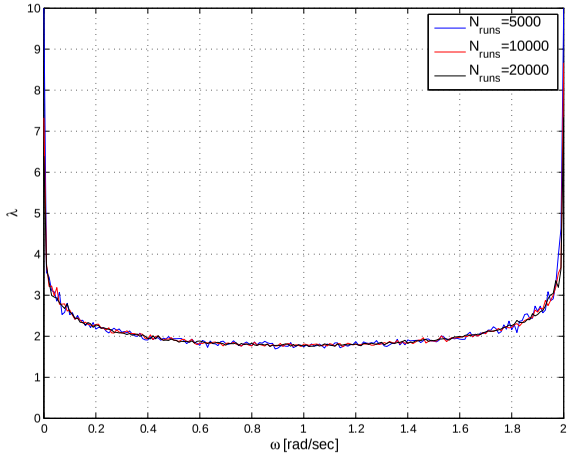

(b) Circular Case (TEV = 4)

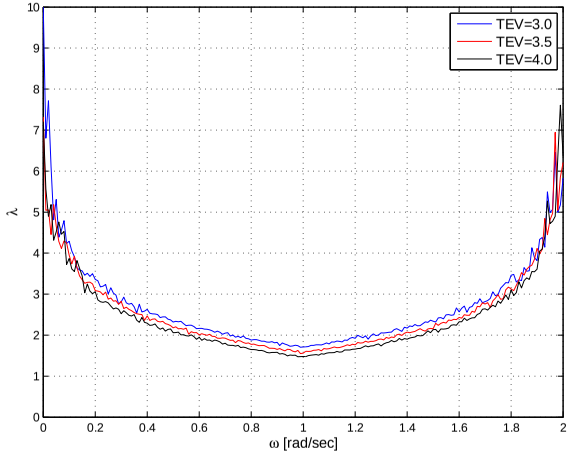

(c) Triangular Case ($N_{runs} = 20000$)

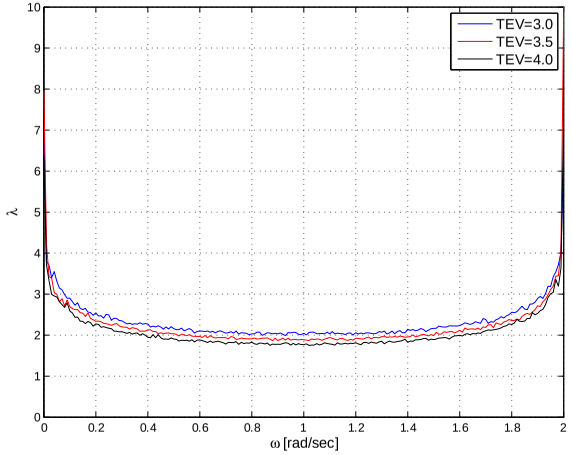

(d) Circular Case ($N_{runs} = 20000$)

Figure 3.12: $\boldsymbol{\lambda}$ Based on Monte Carlo Simulations, as N_{runs} or TEV Increases for Example Sets of $\boldsymbol{a}$

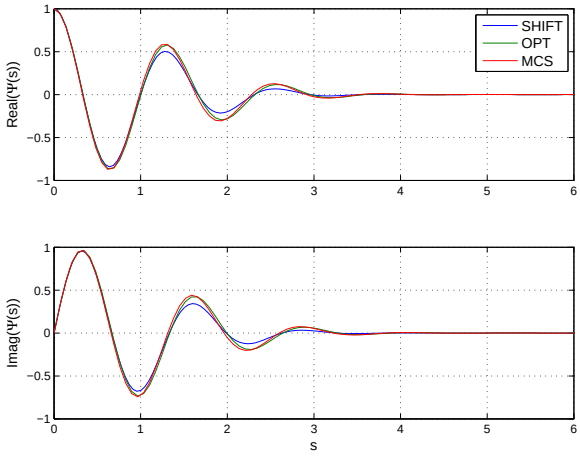

(a) TEV = 4.5

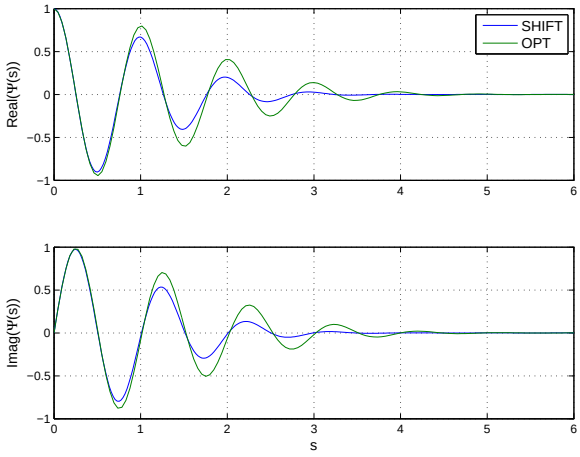

(b) TEV = 6.0

Figure 3.13: Two Example Results of Single-Variable Optimization

The characteristic functions for the two cases are obtained based on the characteristic functions for two sets of 10000 3.0σ realizations and the shift property. These characteristic functions are labeled as SHIFT. Plotted simultaneously are the characteristic functions based on the single-variable optimization formulated in Eqs. (3.23) and (3.25), which is labeled as OPT. For the 4.5σ case, a pure MCS is shown at the same time. Surprisingly, the matching between OPT and MCS is much better than that of OPT and SHIFT in Fig. 3.13(a), even though the objective function of the optimization was formulated using SHIFT. This observation strengthens the foundation of the optimization formulated in this section. Moreover, it suggests the

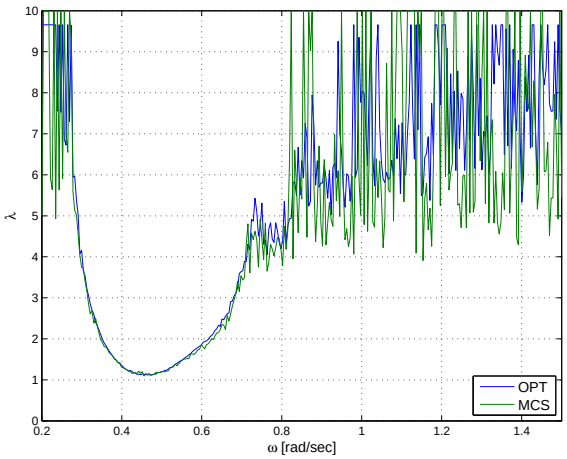

Figure 3.14: Comparison between $\boldsymbol{\lambda}$ from Single-Variable Optimization (OPT) and from Monte Carlo Simulations (MCS) [TEV = 4.5 and $N_{\text{runs}} = 50000$]

phase distributions between MCS and OPT will be very close in Fig. 3.13(b) at least under the *inid* assumption, which is one of the necessary conditions to guarantee the statistical equivalency between the ensembles of the time series from DLG and MCS. Specifically, as shown in Fig. 3.14, the comparison between $\boldsymbol{\lambda}$ from OPT and $\boldsymbol{\lambda}$ from MCS for the same N_{runs} is excellent, considering their statistical natures. The "mismatch" where λ_j is bigger than, say, 4 is statistically negligible as mentioned before, because the modified Gaussian distribution does not change its shape significantly when λ_j is approximately greater than 4.

The results in Figs. 3.13(a) and 3.14 are remarkable, especially when the fact that MCS takes significantly more time is taken into account. For example, MCS needs an order of 400 times more samples than OPT, even when the number of N_{runs} used to estimate $\boldsymbol{\lambda}_{\text{Initial}}$ in OPT is identical to the number of extreme samples of X'_m in MCS. Extensive simulations show that the N_{runs} to be used to estimate $\boldsymbol{\lambda}_{\text{Initial}}$ can be reduced to 5000, or even fewer, without changing the statistics significantly, as suggested in Figs. 3.12(a) and 3.12(b). The cost associated the approximation of $\boldsymbol{\lambda}_{\text{Initial}}$ at this level of N_{runs} is almost trivial, because the initial TEV can be set to 3. It is true that there will be an additional cost associated with the A-R method. However, this cost is practically negligible compared to the savings associated with maintaining N_{runs} constant, as long as c in Eq. (3.19) remains smaller than around 10, which was shown to be possible in Fig. 3.9(b). As TEV increases, the computational time required to execute MCS will increase almost exponentially, as Table 2.1 suggests, while the

computational time to finish OPT is not influenced by TEV. The increase in the total computation time due to the increase in N is at least linear with MCS, while the increase is less than linear with OPT. In summary, the absolute time savings achieved by choosing OPT over MCS is tremendous especially when TEV is bigger than, say 4.5. The savings will increases even more as TEV, N, or N_{runs} increase.

The very last question raised at the end of Sec. 3.4 can finally be answered: $g_Y(y)$ for the target TEV in the A-R method and the sets of the associated phase angle ϵ'_j can be generated very efficiently using the strategy and the optimization problem developed in Secs. 3.5 $\sim$ 3.6. In others words, OPT will be used to obtain $g_Y(y)$, which will then be fed into the A-R algorithm to generate the sets of phase angles. These sets of phase angles can be considered as ${}^k\epsilon_{m_j}$ associated with X'_m, defined in Sec. 2.4. These phase angles will then be used in the construction of an ensemble of short input wave profiles, which will be the topic of the next section.

3.7 Construction of Incident Wave Profiles

An irregular seaway may be expressed as the summation of N Fourier coefficients:

$$\zeta(x, y, t) = \sum_{j=1}^{N} b_j \cos(k_j(x \cos\beta_j + y \sin\beta_j) - \omega_j t + \psi_j) \tag{3.26}$$

where b_j is a set of Fourier coefficients obtained from Eq. (2.2) using the input wave spectrum representing the seaway, x and y are distances from the origin in a global reference frame, and β_j is the heading angle of the corresponding wave coefficients. Without loss of generality, y may be assumed zero. In this case, the wave elevation at a point $(\bar{x}, 0)$, which moves from the origin of the global reference frame at $t = 0$ with a constant velocity U, is expressed as,

$$\begin{aligned}
\zeta(\bar{x}, 0, t) &= \sum_{j=1}^{N} b_j \cos(k_j \bar{x} \cos\beta_j - \omega_j t + \psi_j) \\
&= \sum_{j=1}^{N} b_j \cos(k_j U t \cos\beta_j - \omega_j t + \psi_j) \\
&= \sum_{j=1}^{N} b_j \cos(-\omega_{e_j} t + \psi_j) = \zeta(t)
\end{aligned} \tag{3.27}$$

where ω_{e_j} is the encounter wave frequency defined as

$$\omega_{e_j} = \omega_j - Uk_j \cos\beta_j \tag{3.28}$$

and ψ_j is the phase angles typically distributed between $-\pi$ and π.

Given the response amplitude operator $H(i\omega_e;\beta_j)$ at an arbitrary target point on ship with respect to the incident wave measured at $(\bar{x},0)$, the response time history $x(t)$ measured at the target point is determined as

$$\begin{aligned} x(t) &= \sum_{j=1}^{N} |H(i\omega_e;\beta_j)| b_j \cos(-\omega_{e_j} t + \psi_j + \phi_j) \\ &= a_j \cos(-\omega_{e_j} t + \psi_j + \phi_j) \end{aligned} \tag{3.29}$$

where a_j can be calculated from the response spectrum of the process $S(\omega;\beta_j)$ as

$$a_j = \sqrt{2S(\omega_{e_j};\beta_j)\Delta\omega_{e_j}} = \sqrt{2S(\omega_j;\beta_j)\Delta\omega_j} \tag{3.30}$$

and ϕ_j is the argument (or phase angle) of the response amplitude operator $H(i\omega_e;\beta_j)$ with respect to the incident wave measured at $(\bar{x},0)$. Comparing Eq. (2.1) with Eq. (3.29) shows the relation between ψ_j and ϵ_j.

$$\psi_j = -\epsilon_j - \phi_j \tag{3.31}$$

Therefore, the conversion of ϵ_{m_j} to ψ_j is straightforward, because the phase angles of the response amplitude operator $H(i\omega_e;\beta_j)$ is just a known input parameter to the DLG process. The short incident wave profiles around $t = 0$ from Eq. (3.27) can then be fed into high-fidelity nonlinear hydrodynamic loads computation systems, to find the corresponding nonlinear responses. This is an important part of the DLG process, which will be a topic of Chapter V.

3.8 Summary of DLG Process

In the DLG process, an ensemble of short random wave trains generated by the linear summation of a finite number of spectral coefficients is tailored to produce the distribution of extreme responses during a specified exposure time in the neighborhood of the extreme responses. By applying non-uniform phase distributions of the random extreme event, wave elevations leading to the distribution of extreme

responses can be calculated via linear theory and subsequently used as input to high fidelity nonlinear hydrodynamic computation codes. Fig. 3.15 is a graphical summary of the DLG process

In more detail, the DLG method devised for calculating design responses for a given exposure time and the associated wave elevations takes the following steps.

1. Choose the response of interest (e.g., vertical bending moment, relative motion, or relative velocity).

2. Calculate the input spectrum (e.g., the ITTC Sea Spectrum) and the Response Amplitude Operator (RAO) of the target response to produce the response spectrum.

3. Determine the exposure time the system (e.g., vessel or offshore unit) will spend in a cell, which produces Target Extreme Value (TEV).

4. Check for sufficient number of Fourier coefficients N. In other words, TEV should be sufficiently lower than the maximum attainable response given in Eq. (2.6), or N should be big enough not to limit the maximum from the process artificially.

5. Conduct a quick Monte Carlo simulation for a initial TEV to determine λ_j for the initial TEV.

6. Solve an optimization problem to determine the phase PDFs that is statistically equivalent to those from Monte Carlo simulations of the target TEV. This produces λ_j that corresponds to the target TEV.

7. Generate the sets of phases ϵ_j based on λ_j using the Modified Gaussian distribution.

8. Calculate an ensemble of design responses using linear superposition. Conduct the Acceptance-Rejection procedure described in Sec. 3.4 until the desired number of sets of N phase angles are collected.

9. Calculate corresponding short incident wave profiles using linear systems theory.

10. Calculate an ensemble of extreme nonlinear responses to short wave records using a high fidelity seakeeping program such as CFD codes or time domain potential codes to collect the distribution of extreme nonlinear responses.

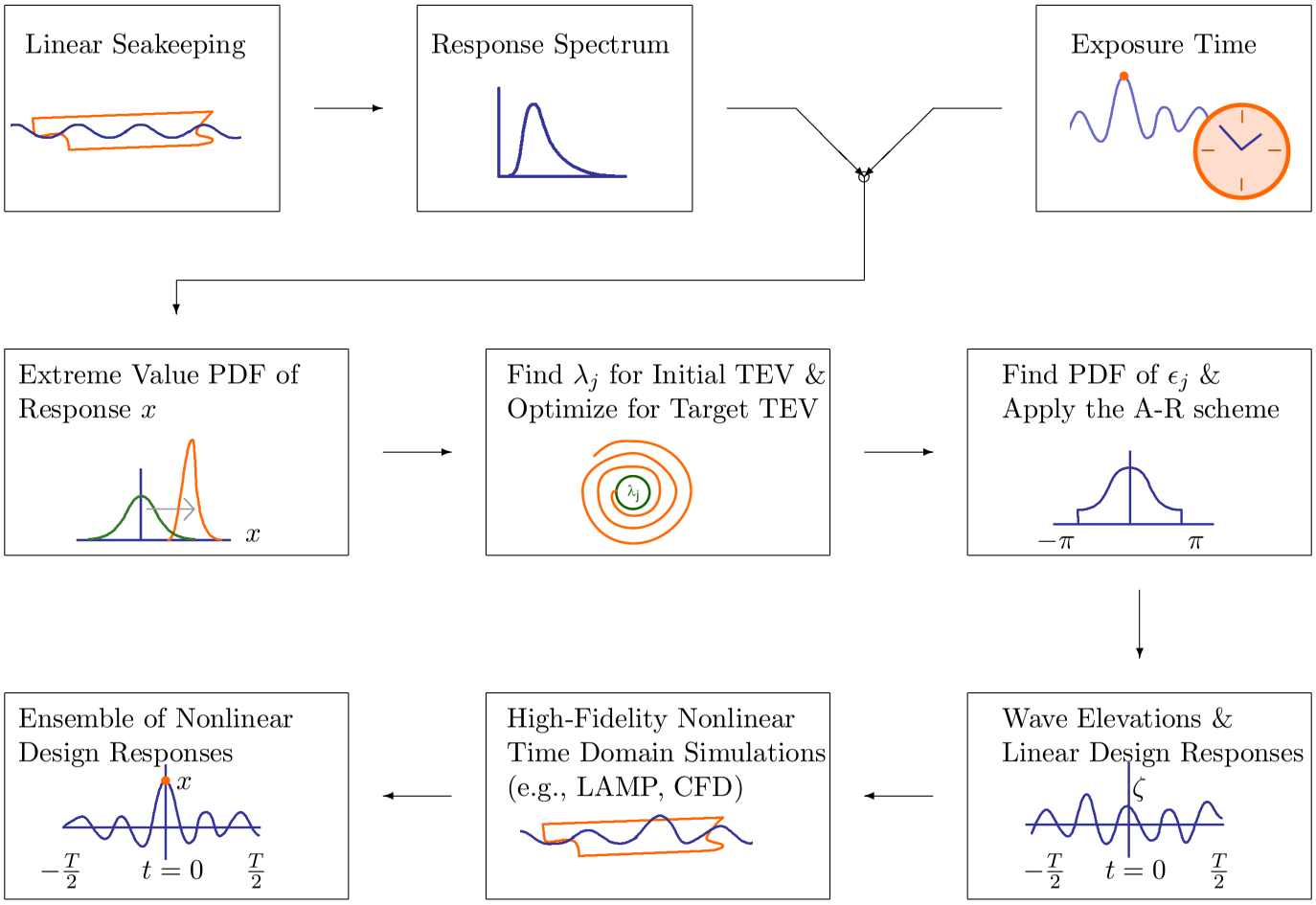

Figure 3.15: Schematic Diagram of Design Loads Generator Approach

CHAPTER IV

Expansion of Problem Formulation

4.1 Sum of Two Gaussian Processes

Implicitly assumed in the development of DLG in Chapters II $\sim$ III are long-crested seaways. Specifically, Eq. (2.1) represents the response of a system that occurs when the incident wave is coming into the system primarily from one direction. A natural question then arises whether the current formulation of DLG can be extended to more general cases. For example, will it be possible to apply DLG to the extreme response under short-crested seaways? To answer these questions, as an initial approximation of short-crested seaways, the response of a system under bi-directional seaways measured at a fixed point is first investigated:

$$x_{\mathrm{bi}}(t) = \sum_{j=1}^{N} {}^{1}a_j \cos({}^{1}\omega_j t + {}^{1}\epsilon_j) + \sum_{k=1}^{N} {}^{2}a_k \cos({}^{2}\omega_k t + {}^{2}\epsilon_k) \tag{4.1}$$

where

$${}^{1}a_j = \sqrt{2S_1({}^{1}\omega_j)\Delta {}^{1}\omega_j} \tag{4.2}$$

$${}^{2}a_k = \sqrt{2S_2({}^{2}\omega_k)\Delta {}^{2}\omega_k} \tag{4.3}$$

and $S_1({}^{1}\omega_j)$ and $S_2({}^{2}\omega_k)$ are two single-sided spectrums, and ϵ_j and ϵ_k are two mutually uncorrelated uniformly distributed (between $-\pi$ and π) random phase vectors. Without loss of generality, the same number of Fourier coefficients N is used to discretize the response spectra. As N goes to infinity, the random variable X_{bi} expressed by the random process $x_{\mathrm{bi}}(t)$ in Eq. (4.1) also goes to a zero-mean Gaussian random variable due to the central limit theorem. In addition, similar to Eq. (2.4), the variance of the random variable can be approximated as

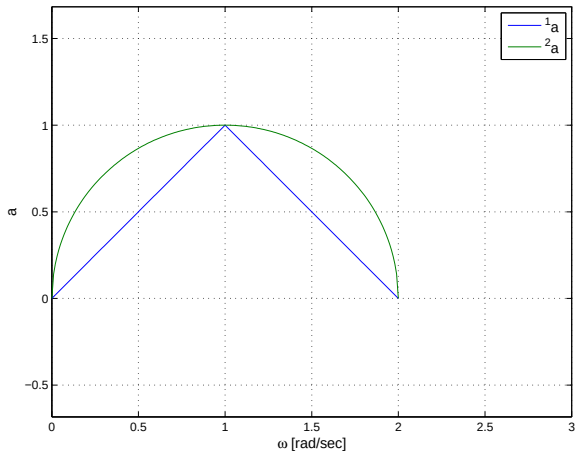

(a) LF + LF Case

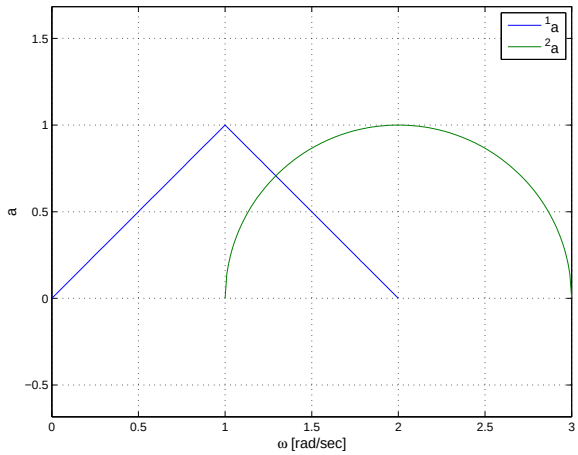

(b) LF + HF Case

Figure 4.1: Two Example Sets of Fourier Coefficients ${}^{\mathbf{1}}\boldsymbol{a}$ and ${}^{\mathbf{2}}\boldsymbol{a}$ [$N = 201$]

$$\sigma_{\text{bi}}^2 \approx \frac{1}{2}\sum_{j=1}^{N}({}^1a_j)^2 + \frac{1}{2}\sum_{k=1}^{N}({}^2a_k)^2 \tag{4.4}$$

The response of a system under bi-directional seaways composed of swells and wind-generated waves with different directionality fits into this model. Instead of more realistic spectrums suitable for swells and wind-generated waves, however, two sets of artificial Fourier coefficients in Fig. 4.1 are selected to show that the development in Chapter III can be extended to the response under bi-directional seaways. These two examples may be viewed as the summation of two different low frequency (LF)

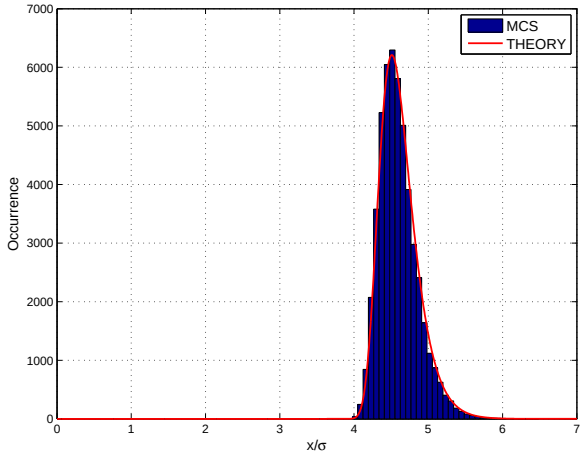

(a) LF + LF Case

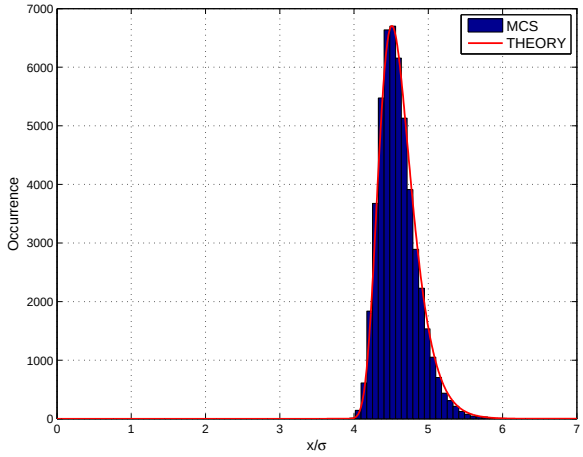

(b) LF + HF Case

Figure 4.2: Extreme Value Distribution from Monte Carlo Simulations (MCS) and Theoretical Extreme Value Distribution (THEORY) for Two Example Sets of Fourier Coefficients [TEV = 4.5 and $N_{\text{runs}} = 50000$]

spectra, and the summation of a low frequency (LF) spectrum and a high frequency (HF) spectrum. From this point, the subscript "bi" will be dropped and the set notation, as defined in Eqs. (3.4) $\sim$ (3.5) will be used at the time same for simplicity.

First of all, the maximum of m samples generated from X, as described in Sec. 2.4, should also follow the theoretical extreme value distribution of a zero-mean Gaussian random variable with variance expressed by Eq. (4.4). Fig. 4.2 confirms that they do actually match, where 50000 realizations of X_m (MCS) are compared with the theoretical extreme value distribution (THEORY). The matching is in fact better

than the comparison in Fig. 3.5(a), which is due to the increased number of Fourier coefficients. Note that the effective number of Fourier coefficients is now doubled to 400. The expected occurrence from THEORY for each cell differs slightly between Fig. 4.2(a) and Fig. 4.2(b), because the number of bins, not the width of bins, in the two histograms is kept constant.

In order to use the current construction of DLG, it is assumed that modified Gaussian distribution can still be used to model the phase PDFs. Under this assumption, Eq. (3.3) can be expanded to Eq. (4.5) as shown in Appendix. B. The characteristic function of the theoretical extreme value distribution does not change from Eq. (3.2) except that the variance of the bidirectional process in Eq. (4.4) should be used.

$$\begin{aligned}&\psi_{X'_m}(s;{}^1\boldsymbol{a},{}^1\boldsymbol{\lambda},{}^2\boldsymbol{a},{}^2\boldsymbol{\lambda})\\&=\prod_{k=1}^{2}\prod_{j=1}^{N}\int_{-1}^{1}\frac{\mathrm{e}^{i\,{}^k a_j s y}}{\pi({}^k\lambda_j)\sqrt{1-y^2}}\left\{\sqrt{2\pi}\;\mathrm{e}^{-0.5\arccos^2 y/\,{}^k\lambda_j^2}-\lambda_j\;\mathrm{erf}\left(\pi/({}^k\lambda_j\sqrt{2})\right)+{}^k\lambda_j\right\}\mathrm{d}y\end{aligned} \tag{4.5}$$

Since two sets of Fourier coefficients are involved in $x(t)$ for each case, two sets of λ_j, here designated as ${}^1\boldsymbol{\lambda}$ and ${}^2\boldsymbol{\lambda}$, need to be determined for each case. Similar to what has been done for Fig. 3.7(a), the phase angles associated with the maximum in m samples are first collected. The least squared method is then used to find the optimized ${}^1\boldsymbol{\lambda}$ and ${}^2\boldsymbol{\lambda}$ such that the squared difference between the modified Gaussian distribution in Eq. (2.26) and the distribution of the phase angles for each set of Fourier coefficients is minimized. Figs. 4.3 and 4.4 show the results of this procedure, which confirms that the convergence of ${}^1\boldsymbol{\lambda}$ and ${}^2\boldsymbol{\lambda}$ as N_{runs} increases for both cases. In addition, found again are the tendencies observed in Fig. 3.12, from which the optimization problem is formulated in Sec. 3.6. What is the most important is that, even for this bi-directional process, ${}^1\boldsymbol{\lambda}$ and ${}^2\boldsymbol{\lambda}$ move downward evenly, while maintaining their original shape as TEV increases. Due to this highly advantageous property, all the developments used for the directional seaways, as explained in Chapter III, can very easily be adapted for the current bi-directional process. Specifically, the optimization problem now becomes one of finding $\boldsymbol{\lambda}_o$ that minimizes the following

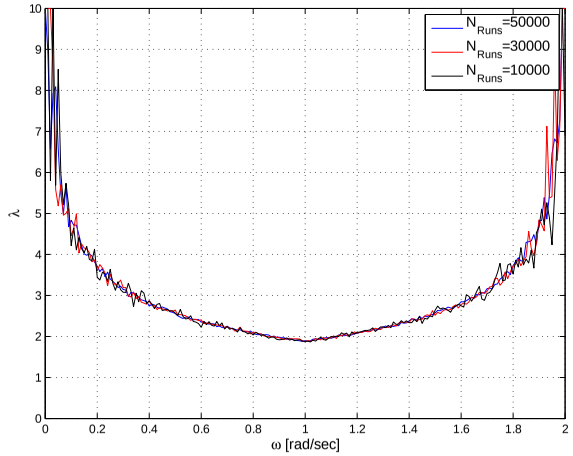

(a) Estimated ${}^1\boldsymbol{\lambda}$ for ${}^1\boldsymbol{a}$ when TEV = 4.5

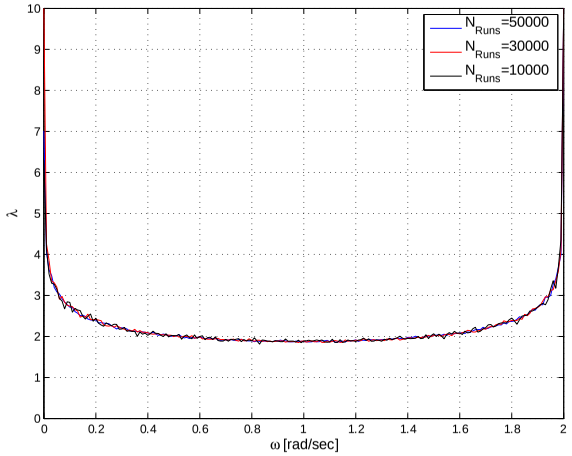

(b) Estimated ${}^2\boldsymbol{\lambda}$ for ${}^2\boldsymbol{a}$ when TEV = 4.5

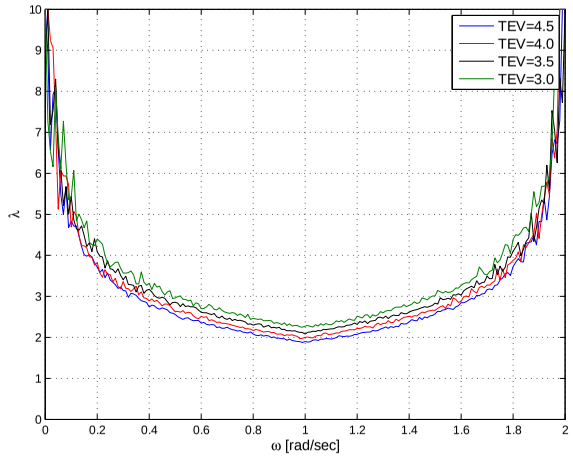

(c) Estimated ${}^1\boldsymbol{\lambda}$ for ${}^1\boldsymbol{a}$ when $N_{\text{runs}} = 50000$

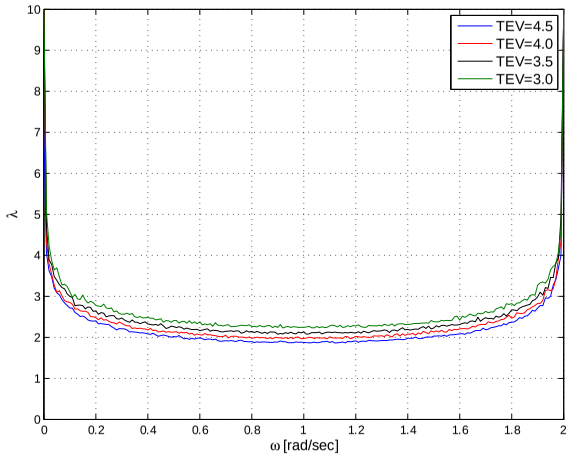

(d) Estimated ${}^2\boldsymbol{\lambda}$ for ${}^2\boldsymbol{a}$ when $N_{\text{runs}} = 50000$

Figure 4.3: $\boldsymbol{\lambda}$ Based on Monte Carlo Simulations (MCS), as N_{runs} or TEV Increases [LF + LF Case]

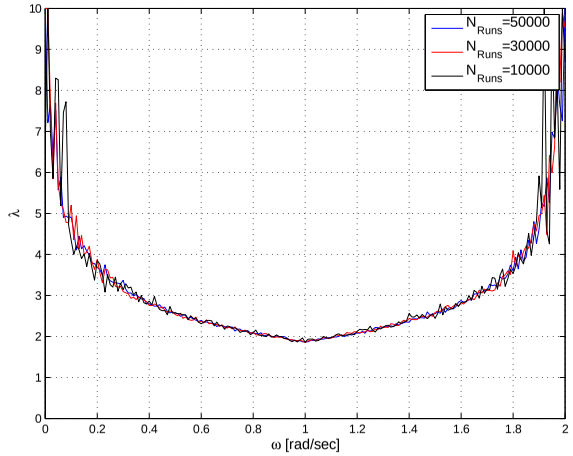

(a) Estimated ${}^1\boldsymbol{\lambda}$ for ${}^1\boldsymbol{a}$ when TEV = 4.5

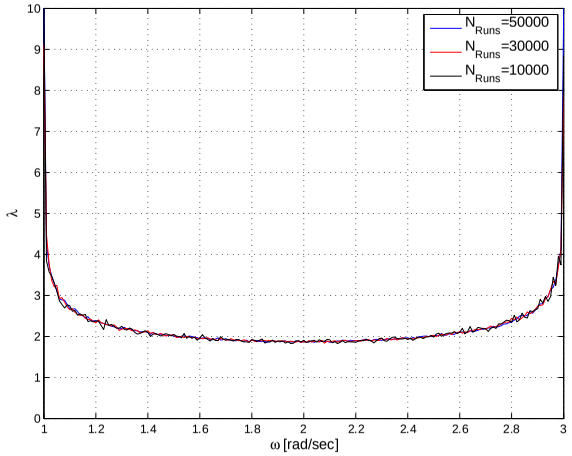

(b) Estimated ${}^2\boldsymbol{\lambda}$ for ${}^2\boldsymbol{a}$ when TEV = 4.5

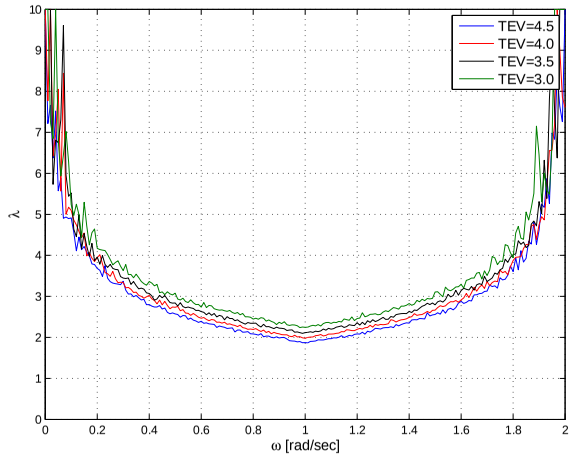

(c) Estimated ${}^1\boldsymbol{\lambda}$ for ${}^1\boldsymbol{a}$ when $N_{\text{runs}} = 50000$

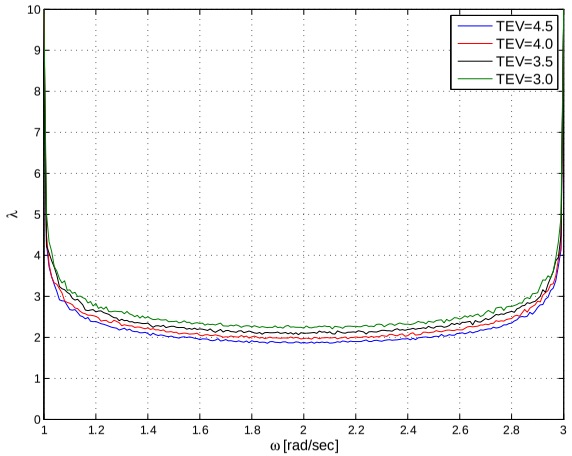

(d) Estimated ${}^2\boldsymbol{\lambda}$ for ${}^2\boldsymbol{a}$ when $N_{\text{runs}} = 50000$

Figure 4.4: $\boldsymbol{\lambda}$ Based on Monte Carlo Simulations (MCS), as N_{runs} or TEV Increases [LF + HF Case]

objective function:

$$g_{\text{objective}}(\lambda_o) = \left[\sum_{l=1}^{N_s} \left| \mathrm{e}^{is_l x_o} \psi_{X'_m}(s_l; {}^1\boldsymbol{a}, {}^2\boldsymbol{a}, {}^1\boldsymbol{\lambda}_{\text{Initial}}, {}^2\boldsymbol{\lambda}_{\text{Initial}}) \right. \right.$$
$$\left. \left. - \psi_{X'_m}(s_l; {}^1\boldsymbol{a}, {}^2\boldsymbol{a}, {}^1\boldsymbol{\lambda}_{\text{Initial}} - \boldsymbol{\lambda}_o, {}^2\boldsymbol{\lambda}_{\text{Initial}} - \boldsymbol{\lambda}_o) \right|^2 \right]^{1/2} \tag{4.6}$$

subject to

$$0 < \lambda_o < \min({}^1\boldsymbol{\lambda}_{\text{Initial}}, {}^2\boldsymbol{\lambda}_{\text{Initial}}) \tag{4.7}$$

where ${}^1\boldsymbol{\lambda}_{\text{Initial}}$ and ${}^2\boldsymbol{\lambda}_{\text{Initial}}$ are from MCS for the initial TEV, x_o is the difference between the initial TEV and the target TEV as defined in Eq. (3.21), $\boldsymbol{\lambda}_o$ is $(\lambda_o, \lambda_o, \ldots, \lambda_o)$, s is discretized between 0 and $s_{\text{threshold}}$, and N_s varies depending on TEV. The operator min finds the smallest element of ${}^1\boldsymbol{\lambda}_{\text{Initial}}$ and ${}^2\boldsymbol{\lambda}_{\text{Initial}}$. The optimal λ_o from Eq. (4.6) can then be used to find the two sets of λ_j for the target TEV event.

$${}^k\boldsymbol{\lambda}_{\text{Target}} = {}^k\boldsymbol{\lambda}_{\text{Initial}} - \boldsymbol{\lambda}_o \Big|_{\text{optimal}} \quad \text{where} \quad k = 1, 2 \tag{4.8}$$

Compared to the uni-direction process analyzed in Chapter III, the computation time to obtain ${}^1\boldsymbol{\lambda}_{\text{Initial}}$ and ${}^2\boldsymbol{\lambda}_{\text{Initial}}$, by solving Eqs. (4.6) and (4.8), increases approximately twofold. However, the increase in the absolute computation time is almost trivial, compared to the savings achieved by applying the current strategy rather than MCS. This is mostly because Eqs. (4.6) and (4.8) can be solved very efficiently. Therefore, the total saving in computational expense over MCS increases approximately twofold, compared to the saving observed in the uni-directional process.

Similar to Fig. 3.13, the results of this optimization applied to two different cases—4.5 and 6.0σ cases of the process defined by the Fourier coefficients shown in Fig. 4.2(b)—are given in Fig. 4.5. The characteristic functions for these two cases are obtained from the characteristic functions of two 3.0σ realizations using the shift property. These characteristic functions are labeled as SHIFT. Plotted simultaneously are the characteristic functions based on the single-variable optimization formulated thorugh Eqs. (4.6) and (4.8), which are labeled as OPT. For the 4.5σ case, a pure MCS is shown at the same time. Similar to Fig. 3.13, the matching between OPT and MCS is slightly better than that of OPT and SHIFT, even though the objective function of the optimization was formulated using SHIFT. This observation shows that the optimization developed for the bi-directional process works as expected, and the A-R method can be applied in the same manner.

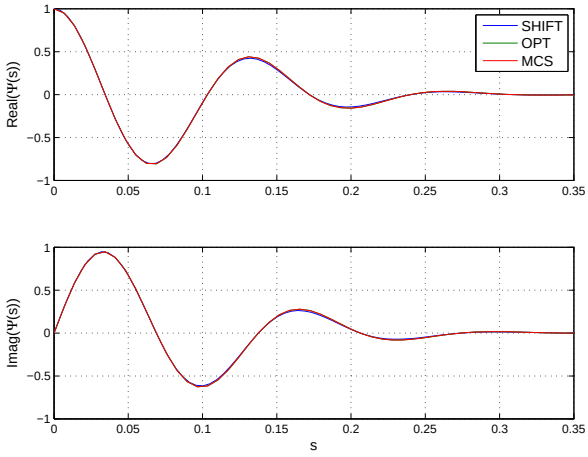

(a) TEV = 4.5

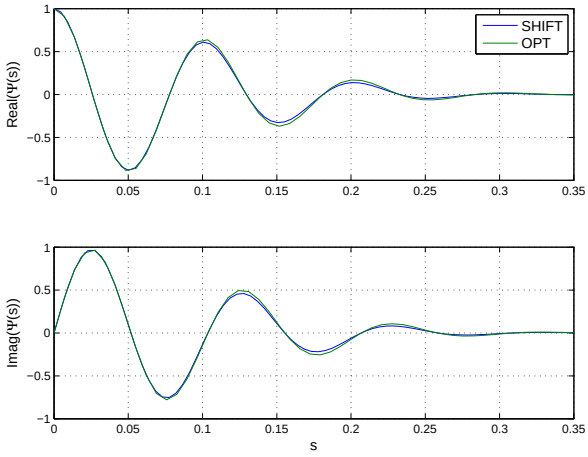

(b) TEV = 6.0

Figure 4.5: Two Example Results of Single-Variable Optimization [LF + HF Case]

For the 6.0σ case, a pure MCS has not been obtained due to prohibitive[1] cost. However, the result so far strongly suggests the phase distributions between MCS and OPT will still be very close, at least under the *inid* assumption, if MCS for the 6.0σ case were available.

[1]It really is prohibitive. The expected computational time for the task with a highly optimized code under the best machine available, at the time of writing, to the author is at least an order of 38 years. This is an estimation linearly scaled, according to Table 2.1, from the actual computational time measured for the 4.5σ case. A well-designed pseudo-random number generator with the implementation of a parallel processing algorithm could reduce the computational cost, but it is unfortunately beyond the scope of the current research.

4.2 Multidirectional DLG

The observation that $\boldsymbol{\lambda}$ moves downward evenly, while maintaining its original shape as TEV increases makes the optimization developed in this research very powerful as shown in Sec. 4.1. Moreover, the optimization problem can be expanded for multidirectional or short-crested seaways, which is the topic of the current section. The response in the short-crested seaways can be expressed as:

$$x(t) = \sum_{k=1}^{h} \sum_{j=1}^{N} {}^{k}a_j \cos({}^{k}\omega_j t + {}^{k}\epsilon_j) \tag{4.9}$$

where

$${}^{k}a_j = \sqrt{2S_k({}^{k}\omega_j)\Delta {}^{k}\omega_j} \tag{4.10}$$

and h is the number of wave spectra. In other words, these equations are the generalization of Eqs. (2.1) $\sim$ (2.2), and Eqs. (4.1) $\sim$ (4.3). Similar to Eq. (4.4), the variance of the process that combines h different processes can also be expressed as

$$\sigma^2_{\text{short}} \approx \frac{1}{2} \sum_{k=1}^{h} \sum_{j=1}^{N} ({}^{k}a_j)^2 \tag{4.11}$$

While the characteristic function of the theoretical extreme value distribution does not change from Eq. (3.2) except that the variance from Eq. (4.11) should be used, the characteristic function of the response that DLG should generate becomes, as explained in Appendix B,

$$\begin{aligned}
&\psi_{X'_m}(s; {}^{1}\boldsymbol{a}, {}^{1}\boldsymbol{\lambda}, {}^{2}\boldsymbol{a}, {}^{2}\boldsymbol{\lambda}, \cdots, {}^{h}\boldsymbol{a}, {}^{h}\boldsymbol{\lambda}) \\
&= \prod_{k=1}^{h} \prod_{j=1}^{N} \int_{-1}^{1} \frac{\mathrm{e}^{i({}^{k}a_j)sy}}{\pi({}^{k}\lambda_j)\sqrt{1-y^2}} \left\{ \sqrt{2\pi}\ \mathrm{e}^{-0.5 \arccos^2 y/ {}^{k}\lambda_j^2} - \lambda_j\ \mathrm{erf}\left(\pi/({}^{k}\lambda_j\sqrt{2})\right) + {}^{k}\lambda_j \right\} \mathrm{d}y
\end{aligned} \tag{4.12}$$

Moreover, the relation between $\boldsymbol{\lambda}$ and TEV shown in Sec. 4.1 remains valid even for multidirectional seaways, which means that the problem now becomes the minimization of the following objective function:

$$g_{\text{objective}}(\lambda_o) = \left[\sum_{l=1}^{N_s} \left| \mathrm{e}^{is_l x_o} \psi_{X'_m}(s_l; {}^1\boldsymbol{a}, {}^1\boldsymbol{\lambda}_{\text{Initial}}, {}^2\boldsymbol{a}, {}^2\boldsymbol{\lambda}_{\text{Initial}}, \cdots, {}^h\boldsymbol{a}, {}^h\boldsymbol{\lambda}_{\text{Initial}}) \right. \right.$$
$$\left. \left. - \psi_{X'_m}(s_l; {}^1\boldsymbol{a}, {}^1\boldsymbol{\lambda}_{\text{Initial}} - \boldsymbol{\lambda}_o, {}^2\boldsymbol{a}, {}^2\boldsymbol{\lambda}_{\text{Initial}} - \boldsymbol{\lambda}_o, \cdots, {}^h\boldsymbol{a}, {}^h\boldsymbol{\lambda}_{\text{Initial}} - \boldsymbol{\lambda}_o) \right|^2 \right]^{1/2} \tag{4.13}$$

subject to

$$0 < \lambda_o < \min({}^1\boldsymbol{\lambda}_{\text{Initial}}, {}^2\boldsymbol{\lambda}_{\text{Initial}}, \cdots, {}^h\boldsymbol{\lambda}_{\text{Initial}}) \tag{4.14}$$

where ${}^1\boldsymbol{\lambda}_{\text{Initial}}$, ${}^2\boldsymbol{\lambda}_{\text{Initial}}$, $\cdots$, ${}^k\boldsymbol{\lambda}_{\text{Initial}}$ are from MCS for the initial TEV, x_o is the difference between the initial TEV and the target TEV as defined in Eq. (3.21), $\boldsymbol{\lambda}_o$ is $(\lambda_o, \lambda_o, \ldots, \lambda_o)$, s is discretized between 0 and $s_{\text{threshold}}$, and N_s varies depending on TEV. The operator min() returns the smallest element among ${}^1\boldsymbol{\lambda}_{\text{Initial}}$, ${}^2\boldsymbol{\lambda}_{\text{Initial}}$, $\cdots$, ${}^k\boldsymbol{\lambda}_{\text{Initial}}$. Once the optimized solution for λ_o is determined, ${}^k\lambda_j$ for the target TEV can be calculated as

$${}^k\boldsymbol{\lambda}_{\text{Target}} = {}^k\boldsymbol{\lambda}_{\text{Initial}} - \boldsymbol{\lambda}_o \Big|_{\text{optimal}} \quad \text{where} \quad k = 1, 2, \cdots, h \tag{4.15}$$

The optimized solution, whether it is derived from a bidirectional process or a multidirectional process, can only produce $g_Y(y)$ in Sec. 3.5. The acceptance-rejection algorithm explained in Sec. 3.4 should be used to generate h sets of phase angles, from which the response time histories and the corresponding incident wave profiles can readily be obtained.

4.3 Example DLG Simulation

As an example DLG simulation, a 5σ event of the incident wave profile at a fixed location is investigated in this section, where a penta-directional seaway is assumed. Specifically, the directional sea spectrum $S(\omega, \beta)$ is calculated from the cosine directional spreading as explained in, for example, Kim (2008):

$$S(\omega, \theta) = S(\omega) D(\theta) \tag{4.16}$$

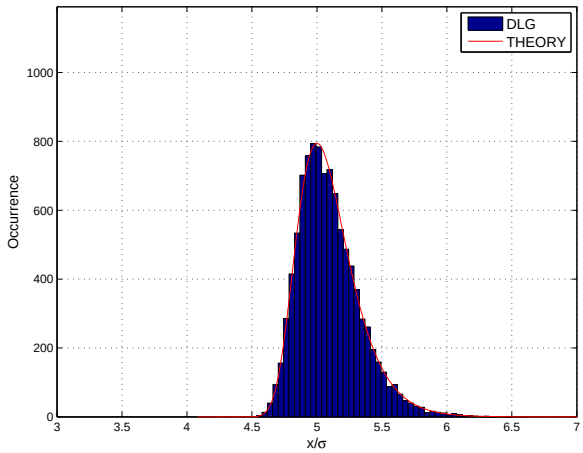

(a) Histogram from 10000 Realizations (TEV=5, $N = 301$, $h = 5$)

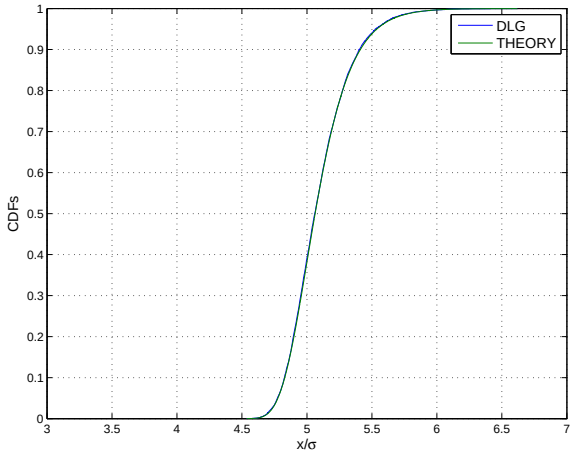

(b) CDF

Figure 4.6: Example Comparisons between 5σ Penta-Directional DLG Realizations and Theoretical Extreme Value Distribution

where

$$D(\theta) = \begin{cases} \dfrac{2}{\pi}\cos^2\theta & \text{when} \quad -\pi/2 \le \theta \le \pi/2 \\ \\ 0 & \text{otherwise} \end{cases} \tag{4.17}$$

As a demonstration, θ is discretized into five different angles: -30, -15, 0, 15, and 30 degrees. For the point spectrum $S(\omega)$, the Bretschneider spectrum with the significant wave height $H_s = 3.25$ [m] and modal wave period $T_p = 9.7$ [sec] is used.

Fig. 4.6(a) shows that the histogram of 10000 realizations generated by the multi-

directional DLG matches the theoretical extreme value distribution. Any realization in the histogram is a possible extreme wave peak amplitude in about 800 hours under the same seaway, considering Table 2.1. The realizations in the histogram are converted into CDF to be compared with the theoretical CDF of the corresponding Gaussian process as shown in Fig. 4.6(b). The application of the A-R method results in very good matching.

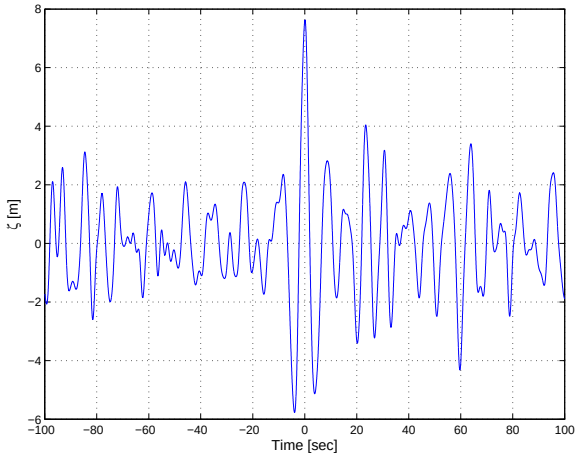

Figure 4.7: Example Time History Recorded at X=Y=0 from 5σ Penta-Directional DLG Realizations

An example realization from the 10000 realizations in Fig. 4.6(a) is presented as a time history in Fig. 4.7. Due to a rather coarse discretization, the loss in the variance is significant. Even compared with the variance of the original point spectrum, the extreme crest height at $t = 0$ exceeds the common criteria of rogue waves (Dysthe *et al.*, 2008).

The DLG model is based on a linear model and it should not be used to analyze ocean rogue waves, even though there is no concensus of theories suitable for rogue waves. However, Fig. 4.7 is not inconsistent with extreme wave examples observed from actual radar measurements as shown in e.g., Lehner (2004). Fig. 4.8(a) shows the seaway captured at $t = 0$. Fig. 4.8(b) is the associated contour plot that shows wave elevations at the same time step.

The DLG process in this case is applied to the incident wave, not the response of a system. Applying the DLG model to the response of a system under a penta-directional seaway is no different from the current example, as discussed in Sec. 3.7. Increasing the number of heading angles to $10 \sim 20$ directions, is very possible.

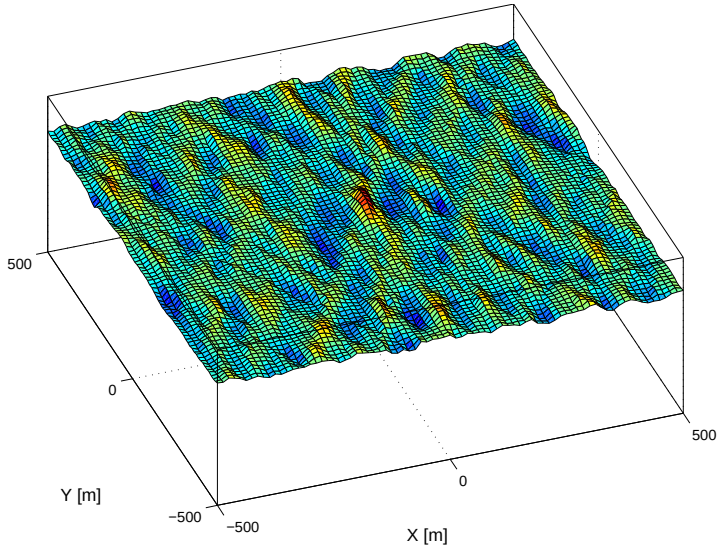

(a) Seaway at $t = 0$

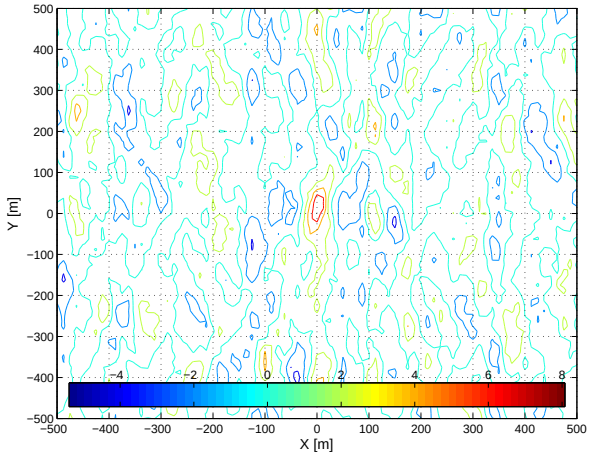

(b) Corresponding Contour Plot of the Seaway at $t = 0$

Figure 4.8: Example Seaway and Corresponding Contour Plot from 5σ Penta-Directional DLG Realizations

Under the cell-based design approach introduced in Sec. 2.3, a long-crested seaway is often assumed. However, applying a short-crested seaway to the cell-based approach is straightforward. Moreover, there are a few problems that can take full advantage of the multidirectional DLG. For example, the bi-directional seaways composed of waves coming from two different directions may be crucial in springing analysis of a vessel, as demonstrated in Vidic-Perunovic (2005) or offshore applications as shown

in, for example, ABS (2010).

As mentioned in Sec. 1.3.2, the most likely wave profile conditioned on a fixed maximum value at $t = 0$ under the short-crested seaway has been discussed in Pastoor (2002). Compared to Pastoor (2002), which is essentially the generalization of Tromans *et al.* (1991), the current multidirectional DLG can capture the variability of the irregular random waves associated with a given exposure time. Thus, the DLG approach is much more suitable for realistic design problems as explained in Chapter I.

CHAPTER V

Nonlinear Time Domain Simulations

5.1 Large Amplitude Motions Program

Numerical time domain simulations are performed using the Large Amplitude Motions Program (LAMP). The program can provide both linear and nonlinear solutions to the seakeeping problem at various levels, and may be considered as a high-fidelity hydrodynamic computation tool that has been verified and validated extensively (Shin *et al.*, 2003).

LAMP is a time domain simulation model developed specifically for computing the motions and loads of a ship in rough seas. LAMP uses a time-stepping approach in which all forces and moments acting on the ship, including those due to wave-body interaction, appendages, control systems, and green water on deck, are computed at each time step. The forces and moments are used to solve the equations of the motion at each time step. In addition to ship motions, LAMP computes the main hull-girder loads using either a rigid or elastic beam model, and includes an interface for developing finite element load data from the three-dimensional pressure distribution. Various post-processors are available to calculate, for example, impact-induced bending moments (or whipping) based on the rigid hull computation, or surface pressure due to impacts. The following description of the program suite is taken from the manual (Lin *et al.*, 2008).

- LAMP1 (Body linear solution): Both perturbation potential and hydrostatic and Froude-Krylov forces are solved over the mean wetted hull surface.
- LAMP2 (Approximate body nonlinear solution): The perturbation potential is solved over mean wetted hull surface while the hydrostatic and Froude-Krylov forces are solved over the instantaneous wetted hull surface.

- LAMP3 (Approximate body nonlinear solution allowing large lateral motions): The perturbation potential is solved over the mean wetted surface while the hydrostatic/Froude-Krylov forces are solved over the instantaneous wetted hull surface. LAMP3 is different from LAMP2 in the sense that LAMP3 can handle large lateral motions.

- LAMP4 (Body nonlinear solution): Both the perturbation potential and the hydrostatic and Froude-Krylov forces are solved over the instantaneous wetted hull surface.

The most practical level is the approximate body-nonlinear LAMP2 solution, as it captures a significant portion of nonlinear effects in most ship-wave problems at a fraction of the computation effort for the general body-nonlinear formulation. Although DLG does not dictate the use of LAMP, all nonlinear time domain computation results reported in the current research, including the results from Monte Carlo simulations, are based on LAMP. Specifically, the approximate body-nonlinear LAMP2 version of the code is used.

5.2 LAMP Post-Processors

The prediction of two important impact-induced loadings, whipping bending moment and impact pressure, are presented in Chapter VI $\sim$ VII. These two loading are rapidly varying and hard to calculate accurately. LAMP is capable of generating these two loadings using the post-processors introduced in this section. Although LAMP has been verified and validated quite extensively in general, the calculation of these two highly nonlinear transient loadings (especially impact pressure) need further research. The DLG model will still remain valid.

5.2.1 LMPOUND

To account for the whipping loads, several options are available within LMPOUND. This LAMP post-processor does calculate slamming loads and the resulting main-girder structural response (i.e., whipping). The hydrodynamic impact forces are calculated using two dimensional approaches. Specifically, ships are modeled by a collection of 2-D sections or stations that are created by making cuts of the LAMP input geometry. The motion of each cut with respect to the incident wave free surface is computed from the 6-DOF ship motion history and the incident wave profiles. Impact forces are then calculated, at each time step, on the sections where the relative

velocity is negative and the bottom point of the section is submerged. The structural response is calculated based on these impact force calculations. This means that the impact forces and vibrations are decoupled from the motions of the ship and other hydrodynamic forces computed by main LAMP runs, and the number and the location of stations are two important input parameters to LMPOUND.

In LMPOUND, four different options are available to calculate the impact force. Of four different approaches, The results presented in this research are primarily based on SLAM2D and WEDGE options.

- SLAM2D: a generalized Wager solution where the exact body boundary condition is satisfied on the body surface.
- WEDGE: a semi-empirical formula based on a semi-empirical wedge approximation, where sectional forces are calculated via the changing added mass of an equivalent two-diminutional wedge.

LMPOUND calculates the structural response using a finite element analysis via either direct integration or modal superposition. The direct integration is mainly used in the current research.

To find out the best approach is not of interest in the current research. However, it is noted that different options and input parameters may produce significantly different results. Therefore, special care is taken to use the same option and parameters, when a comparison is made.

LMPOUND also calculates the impact pressure at a node point. This pressure, combined with the summation of three different types of pressure in LMPRES, is termed as the total pressure P_{tot} in Chapter VII

5.2.2 LMPRES

LMPRES is another important post-processor that computes the surface pressure due to the three different potentials. In other words, the total pressure from LMPRES is a summation of three different components:

$$P_T = P_{FK} + P_{HS} + P_{PF} \tag{5.1}$$

where P_{FK} is the Froude-Krylov pressure, which is due to the linear components of the incident wave; P_{HS} is the hydrostatic pressure; and P_{PF} is the perturabtion pressure, which includes the effects of radiation, diffraction, forward speed and nonlinear terms in the incident wave potential. But the perturbation pressure from LMPRES does not

include the impact pressure. On the contrary, the impact pressure can be calculated from LMPOUND, as mentioned above. So the "real" total pressure may be defined as

$$P_{TOT} = P_T + P_I \tag{5.2}$$

where P_T is the total pressure from LMPRES and P_I is impact pressure from LMPOUND.

In LAMP2, the perturbation potential is computed about the mean wetted surface, as mentioned in Sec. 5.1. Therefore, the perturbation pressure is *mapped* onto the instantaneous water surface.

5.3 Statistical Extrapolation from Nonlinear Simulations

Arguably, extensive Monte Carlo simulation in time domain is the correct way to define the design events. However, one of the critical limitations with the Monte Carlo approach is its high implementation cost. In most design applications, the extreme value comparable to the lifetime extreme cannot be found through Monte Carlo simulations alone. Hence, additional statistical techniques are often used in addition to short term Monte Carlo simulation.

The typical approach used to statistically predict lifetime maximum loads is based on Weibull analysis techniques, assuming the responses collected during full-scale trials and model tests may follow a Weibull distribution.

Regardless of whether model testing or computer simulation is used, the general rule of thumb for analyzing a specific sea state/ship speed/heading combination (i.e., a cell) is to collect 30 minutes of data for linear ordinary wave-induced loads and 60 minutes for nonlinear responses such as combined wave plus whipping loads. The resulting time histories can then be statistically analyzed to estimate extreme values for a specified PNE, provided a sufficient number of samples are collected for a given sea state, speed, and relative heading.

The general three-parameter Weibull cumulative distribution function (CDF) is expressed as follows:

$$F_X(x) = \begin{cases} 1 - \exp\Big[- \Big(\dfrac{x - x_{\text{threshold}}}{\eta - x_{\text{threshold}}} \Big)^{\beta} \Big] & \text{if } x > x_{\text{threshold}} \\ 0 & \text{if } x \leq x_{\text{threshold}} \end{cases} \tag{5.3}$$

where

F_X: the cumulative distribution function of a Weibull random variable X

β: a shape (or slope) parameter

$x_{\text{threshold}}$: a threshold value below which there is no measurable data

η: a characteristic value which corresponds to the x value with a cumulative probability of $1 - \mathrm{e}^{-1}$ (or approximately 0.632)

$\eta - x_{\text{threshold}}$: a scale factor

To use the Weibull distribution to extrapolate the target extreme, the CDF of each observed sample should be calculated, for which order statistics can be utilized:

$$F = F_X(x_k) = \frac{k}{n+1} \tag{5.4}$$

where n is the total number of observed samples (i.e., peaks or troughs), and k is the order of the numbers with $k = 1$ being the smallest value and $k = n$ being the largest value. Based on Eq. (5.4), the CDF value of DLG realizations can also be calculated, which will be necessary to compare the results from DLG with the results from Monte Carlo simulations. In this case, the expected number of observations from Eq. (2.18) is used instead of the total number of observed samples n.

Depending on the Weibull shape parameter, β, the distribution can be the exponential ($\beta = 1$) or the Rayleigh ($\beta = 2$) with many other distributions possible. The condition that $x = \eta$ occurs at the same cumulative probability (i.e., $1 - \mathrm{e}^{-1}$) on every Weibull distribution, and is independent of the slope parameter. This condition is called the characteristic value. Some amplitude data can contain values that are relatively small, and in such cases the threshold parameter, $x_{\text{threshold}}$, may be assumed zero.

If a random variable X follows the Weibull distribution, the measurement of the random variable X will form a straight line in Weibull space defined by $\big(\ln(x - x_{\text{threshold}}), \ln\big(-\ln(1 - F_X(x))\big)\big)$. The slope of the straight line is the shape parameter β and the y-intercept is $-\beta\ln(\eta - x_{\text{threshold}})$. Subsequently, the analysis essentially becomes the estimation of the Weibull parameters to extrapolate the lifetime extreme response from observed samples.

A natural approach to find the Weibull parameters from the sampled data is linear regression. The ordered linear regression method provides an easy graphical means of

assessing the data and determining the Weibull parameters. However, linear regression has two major shortcomings. The ranking of the individual peak magnitudes and the assigning of probability terms to each peak present potential errors, unless the measured data population is very large. In addition, in plotting the data, the slope and intercept terms are biased to the lower magnitudes by the nature of logarithmic plots. The more important data are the higher magnitude peaks, which have lesser weighting using the linear regression approach. This can result in the linear regression providing a better fit to the lower magnitudes and distorting the Weibull parameters for the higher magnitudes that are of much greater interest.

One method to address this limitation in determining the Weibull parameters is based on calculating the mean and variance of the data set, and estimating the characteristic value. For a three-parameter Weibull distribution, as explained in e.g., Bishop & Price (1979), the analysis is essentially to solve the following two equations for β, and x_o:

$$\mu_{sample} = (\eta - x_{\text{threshold}})\Gamma(1 + \frac{1}{\beta}) + x_{\text{threshold}} \tag{5.5}$$

and

$$\sigma^2_{sample} = (\eta - x_{\text{threshold}})^2 \left[\Gamma(1 + \frac{2}{\beta}) - (\Gamma(1 + \frac{1}{\beta}))^2\right] \tag{5.6}$$

where μ_{sample} and σ_{sample} are just the mean and the variance of the observed data, and η is estimated from the observed data by finding the sample with the CDF of $1 - \mathrm{e}^{-1}$.

Compared to a simple linear regression method, this so-called moment method provides a better fit to the entire data distribution, in the sense that the lower magnitude data are not weighted. In the study of the high speed sealift vessel, both the linear regression and the moment method are applied. The results that provided the best fit are used for comparisons in Chapters VI $\sim$ VII.

Given η, β, and $x_{\text{threshold}}$, the extreme value can be estimated by the extrapolation for the expected length of time D_i, or equivalently, the number of samples n (i.e., the number of peaks or troughs) in each operational cell. Specifically, when the CDF of extrema from Eq. (5.3) is combined with the definition of PNE in Eq. (2.19), the lifetime maximum for an operational cell corresponding to a specific PNE may be calculated as

$$\bar{x}_n\big|_{\text{PNE}} = x_{\text{threshold}} + (\eta - x_{\text{threshold}})(-\ln(1 - \text{PNE}^{1/n}))^{1/\beta} \tag{5.7}$$

Although this approach is a de facto standard, there are a few important limitations. One of them is the uncertainty associated with the insufficient number of samples. For example, the statistical extrapolation of nonlinear loads based on just one hour's worth of data can result in very large uncertainties. Another limitation is that the approach is based on the validity of the Weibull distribution. For example, while it is reasonable to assume that a certain limit exists for physical responses, the method itself can not capture it. These limitations will be discussed again in the following chapters.

5.4 Test Hull Form: Joint High Speed Sealift (JHSS)

The nonlinear time domain simulation is an important part of the DLG process as emphasized several times. In the research, as a test vessel of the DLG process, a Joint High Speed Sealift (JHSS) hull from is chosen. The JHSS is a potential future logistic ship of the US Navy, whose feasibility is currently being evaluated. The JHSS concept is expected to perform as a future inter-theater connector supporting sea-based operations. The principal dimensions and the numerical hull model of the JHSS are shown in Table 5.1 and Fig. 5.1, respectively.

Table 5.1: Principal Dimensions of JHSS

Parameter	Value
LOA	303 m
Beam	32.0 m
Draft	8.65 m
Displacement (mass)	35122 tonnes
Model Number	5663

In this research, a limited amount of experimental results[1] are also presented. The experimental model of the JHSS is shown in Fig. 5.2. The model as constructed is a segmented model which entails six shell sections connected to a structurally-scaled, continuous aluminum back-spline beam that is instrumented with strain gages at each segment cut to provide measurable responses from combined quasi-static and dynamic seaways loads. For primary hull girder loads data, a sampling rate of 200 Hz is used to collect the data. Following standard practice, the sampling rate is approximately 20 times the lowest hull natural frequency (Dinsenbacher & Engle, 2011).

[1]Experimental results shown in this dissertation have been previously presented in Kim *et al.* (2011)

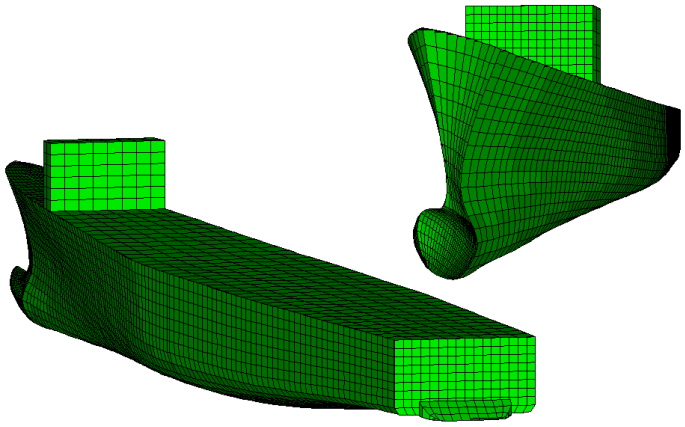

Figure 5.1: LAMP Geometry of Joint High Speed Sealift Segmented Model

In order to conduct the most rigorous experiments/LAMP comparison possible, the experimental incident wave profile, measured at a point forward of the model, was projected to the midship position of the model using linear gravity-wave theory. This profile was then used as input to LAMP simulations, which will be introduced in the following chapters.

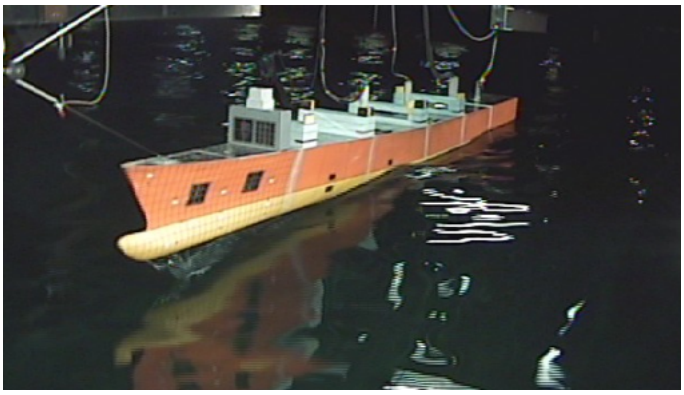

Figure 5.2: Joint High Speed Sealift Segmented Model (Dinsenbacher & Engle, 2011)

While experimental pressures for the JHSS are unavailable for comparison, it is noted that the LAMP motions calculation, which has been extensively validated, requires accurate force (or potential pressure) calculation. However, the calculation of the impact pressure that will be presented in the following chapters is, without a doubt, of a topic of further research. It is assumed that LAMP is capable of generating reasonably accurate impact pressures, based on, for example, reasonably accurate impact-induced midship bending moment predictions.

CHAPTER VI

Application I: Estimation of Extreme Bending Moments

6.1 Midship Bending Moments

One of the most important hull loadings of any ship is the hull girder vertical bending moment. Especially important is the midship bending moment, which is used in the scantlings of structural members at midship and become the basis of designing the entire hull structure. The midship bending moments may be decomposed into still-water bending moment, wave induced-bending moment, and impact-induced (or whipping) bending moment. In this chapter, as a validation of DLG, the estimation of long-term wave-induced bending and impact-induced bending for a Joint High Speed Sealift (JHSS) type hull is studied numerically and experimentally.

One of the most important tasks in the structural design process is to find the lifetime maximum load with the desired level of confidence. To do so, the identification of design events for each operational cell is a most critical step. The "design event" encompasses the stochastic wave field, the vessel dynamic response, and the subsequent hydrodynamic loading, all of which contribute to the combined wave and whipping design bending moment for a single operational condition.

As mentioned in Sec. 2.3, once M design events in Eq. (2.21) have been determined, the lifetime maximum loads of each cell may be calculated using statistical extrapolation techniques. The lifetime maximum load of a vessel is the combination of the lifetime maximum loads of each cell, as dictated by Eq. (2.22). However, engineering expediency may restrict the investigation of the lifetime load to a small number of operational cells, as the reduced number of cells still requires a significant amount of computation. Instead of attempting the calculation of the lifetime maximum combining all cells, which is beyond the scope of the dissertation, the lifetime

maximum loads of a small number of cells are studied using the numerical data calculated from the LAMP program introduced in Sec. 5.1 and the experimental data available from Kim *et al.* (2011). The realizations from DLG are compared with the results from the statistical extrapolation techniques and two long-term Monte Carlo simulations. The environmental and operating conditions of the cells tested in this chapter are summarized in Table 6.1.

Table 6.1: Environmental & Operation Conditions of Bending Moment Test Examples

Sea State (SS)	H_s [m]	T_{modal} [sec]	Wave Heading [deg]	Speed [knots]
5	3.26	9.7	180	15
7	7.5	14	180	15
8	11.5	16.4	180	23
Hurricane Camille	12.2	13.4	180	15

As explained in Kim *et al.* (2011), all experimental results introduced in this dissertation were performed in random seas, utilizing a Bretschneider wave spectrum. Data was collected for a minimum of 30 minutes, full scale. For operational conditions where nonlinear effects were expected, a minimum of 60 minutes of equivalent full scale data was recorded. For all test conditions, ship motions, accelerations, global and local loads were measured. In addition, all wave time histories were recorded at a location in front of the model. The recorded data was then used in conjunction with linear wave theory such that the actual waves encountered by the model ship could be determined and used in any subsequent time domain LAMP simulations.

6.2 LAMP for Weibull Extrapolation

Although nonlinear time domain simulation such as LAMP simulation is an important part of the DLG process, the validation of the numerical simulation code is not the topic of the current research. Rather, the purpose of this research is to develop DLG, to show the application of DLG, and to validate DLG to the extent possible. However, a few different comparisons from LAMP simulations and model tests will strengthen the credibility of the results shown in this chapter, which is the topic of the current section.

As shown in Fig. 6.1, it is possible to reasonably accurately express the incident wave profile measured in the model tests with a finite number of wave components.

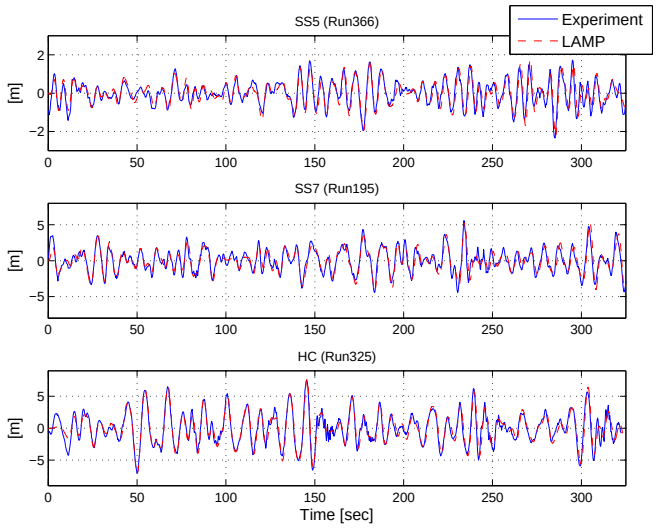

Figure 6.1: Comparison of Incident Wave Time Histories for Example Cases

Extensive test/simulations using these "almost" equivalent incident wave profiles confirm that the match between the LAMP results and the model tests is very accurate in most cases. As can be seen in Table 6.2, for example, a very good comparison is obtained from the LAMP results up to sea state 7. However, the JHSS simulations in Hurricane Camille (HC) at 15 knots and head seas do not show the same level of agreement. The time domain comparison in Fig. 6.2 shows that the LAMP program is able to predict pitch responses even in HC at 15 knots, but not so successfully predict the impact-induced vertical bending moment[1] that occurred at approximately 25 seconds. The LAMP simulated time history results in a shape parameter of just under 2.0 (the Rayleigh distribution), whereas the response time history generated by the model test results in a value of approximately 1.5 (closer to the Exponential distribution). If this trend is representative of other operational cells, it may result in a significant deviation in the estimation of the lifetime maximum load. Thus, this example illustrates one of the potential shortcomings inherent in the statistical extrapolation mentioned in Sec. 5.3. Nevertheless, it is noted that the overall comparison is quite good even for HC.

[1]The sign convention in Fig. 6.2 is following the convention of the experimental results, which is opposite of the LAMP convention. In LAMP, the positive bending represents sagging.

Table 6.2: Summary Comparison of Model Tests Data vs. LAMP Results for Joint High Speed Sealift Hull Form [Midship Wave-Induced + Whipping Bending Moments]

Parameters	Sea State 5		Sea State 7		Hurricane Camille	
	LAMP	Model	LAMP	Model	LAMP	Model
β	2.05	2.08	1.75	1.71	1.96	1.30
η [Nm]	2.49E+08	2.75E+08	8.95E+08	8.75E+08	1.93E+09	1.44E+09
# of Peaks	230	190	244	259	393	504
μ_{sample} [Nm]	2.21E+08	2.44E+08	7.98E+08	7.81E+08	1.71E+09	1.33E+09
σ_{sample} [Nm]	1.13E+08	1.23E+08	4.66E+08	4.69E+08	9.10E+08	1.03E+09
Minimum Sample [Nm]	5.62E+05	7.29E+06	9.70E+06	3.72E+06	4.75E+05	4.09E+06
Maximum Sample [Nm]	6.27E+08	5.55E+08	2.81E+09	2.70E+09	5.10E+09	6.37E+09

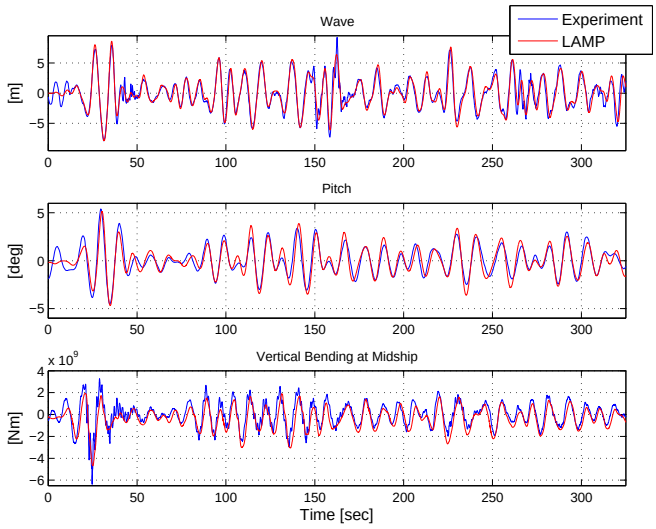

Figure 6.2: Example Incident Wave Profile and Corresponding Pitch and Midship Bending Time Histories [Hurricane Camille, 15 knots, Run 332]

6.3 Monte Calo Simulations

As mentioned in Sec. 5.3, the Monte Carlo approach is arguably one of the best approaches to study a complex nonlinear system with uncertainty in input. However, in general, empirically derived extreme value histograms (or distributions) based on Monte Carlo simulations are not feasible for high-fidelity hydrodynamic computation programs. To illustrate the value of DLG to the extent possible in this research, extensive Monte Carlo simulations are conducted using LAMP2. That is, two relatively "long-term" LAMP2 Monte Carlo simulations are conducted to validate the DLG process: an ensemble of 5 minute and 15 minute random incident wave profiles are generated by using sets of 300 uniformly distributed random phase angles in Eq. (2.1). The 5 minute time histories represent SS8, and the 15 minute time histories represent SS7 defined in Table 6.1. By keeping any one record length relatively short, self-repetition of the incident wave profiles due to the finite number of Fourier coefficients N is prevented, as suggested, e.g., in Belenky (2005).

The associated linear midship bending wave profiles can readily be calculated using the corresponding response amplitude operators. An example time series from this process is illustrated in Fig. 6.3. When this process is repeated 288 times and 3000 times for SS8 and SS7 respectively, the extrema of linear midship bending moments from 24 hours' and 750 hours' worth of Monte Carlo simulations are collected. Specif-

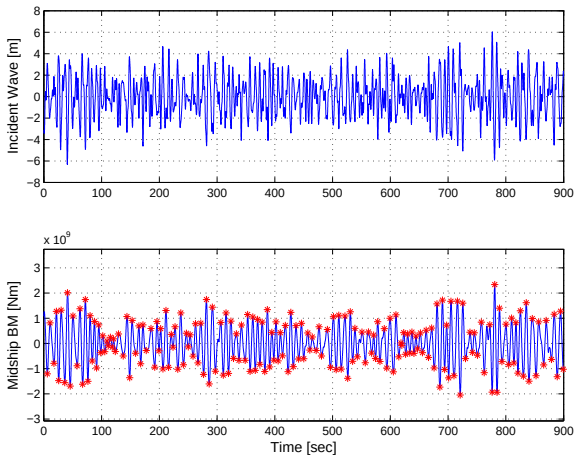

Figure 6.3: Example Incident Wave Profile and Linear Midship Bending Time History [Sea State 7, 15 knots, Head Seas]

ically, the peaks and troughs in the zero-upcrossing cycles of the bending moment time histories are collected to be presented in a Weibull space. The peaks and troughs will form a straight line if they follow the Weibull distribution perfectly. Moreover, the slope parameter β of the line should be close to 2, as shown in Fig. 6.4, because the results are based on linear theory. As expected, there is no significant difference between the positive bending moments (SAGGING) and the negative bending moments (HOGGING). Note that F in this figure comes from Eq. (5.4).

The incident wave time histories of the composite Monte Carlo simulations are next simulated in LAMP2 to calculate the nonlinear JHSS wave-induced midship bending moments and combined midship bending moments. One set of example time histories of the LAMP simulation is presented in Fig. 6.5. The LAMP bending moments represent the dynamic portion of the raw outputs from LAMP, while the combined bending moment moments are defined as the summation of rigid wave-induced midship bending moments and the impact-induced midship bending moments from LMPOUND. To identify peaks and troughs, the zero-upcrossing period is again used. Note that the lengths of the total time series are slightly under 24 hours and 750 hours, due to the initial transients and incomplete cycles at the end of the record.

Unlike Fig. 6.4, the difference between the positive bending moments and the negative bending moments is in general distinct, as shown in Fig. 6.6. Since the sagging bending moments can be significantly larger than the hogging, the sagging bending moments are of greater interest. However, the hogging bending moments

will also be discussed in Sec. 6.8.

The difference between the linear bending moments and the nonlinear bending moments can also be quite significant, and these differences show the necessity of including nonlinearities in the estimation of design loads. For small peaks/troughs, duplicated samples are found due to an artificial low limit of the LAMP bending moments, which occurs because LAMP uses a single-precision floating format for printing out the bending moments. In order to prevent the duplicates and to reduce to numerical "noise" about the mean value, samples smaller than a threshold value (2 percent of the maximum value) are filtered out. This operation slightly changes the denominator of Eq. (5.4). After this operation, the mean period of LAMP2 time histories becomes closer to the mean period calculated from the response spectrum of the process, while the effects on the estimation of the Weibull parameters, especially when based on the momentum method, are negligible.

Fig. 6.6 shows that the assumption of even wave-induced bending moments following the Weibull distribution can be a risky one, which illustrates another shortcoming inherent in the statistical extrapolation mentioned in Sec. 5.3. A bigger problem is that this limitation may not be recognized easily, when the length of the simulation is, for example, $0.5 \sim 3$ hour. More specifically, in Fig. 6.7, the linear extrapolation based on a subset (1 hour) of the 24 hour Monte Carlo simulations seems not unreasonable. But it will result in a significant over-prediction as suggested by Fig. 6.6.

This shortcoming may be viewed in a different way, using the 750 hour composite

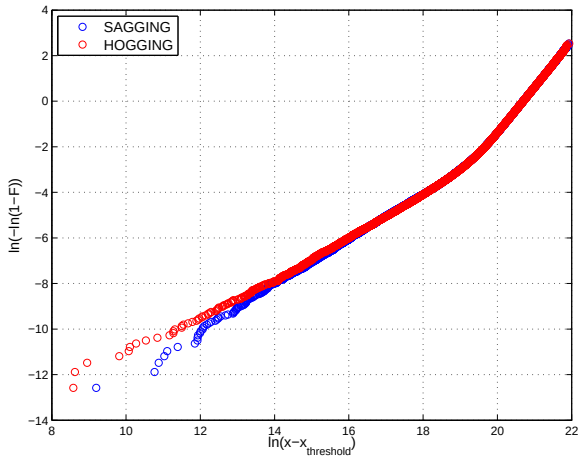

Figure 6.4: 750 Hour Composite Monte Carlo Simulation of Linear Midship Bending Moments in Weibull Space [Sea State 7, 15 knots, Head Seas]

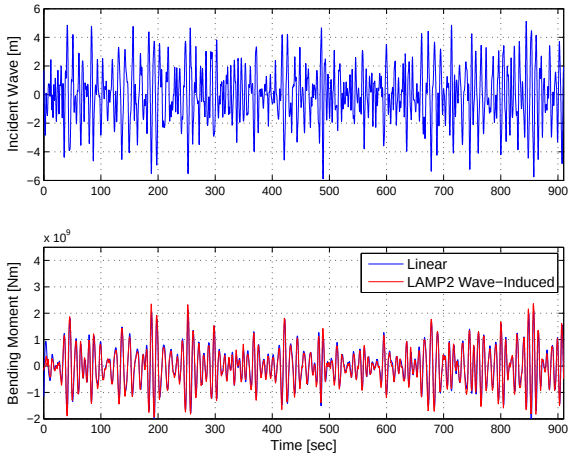

(a) Incident Wave and Wave-Induced Bending

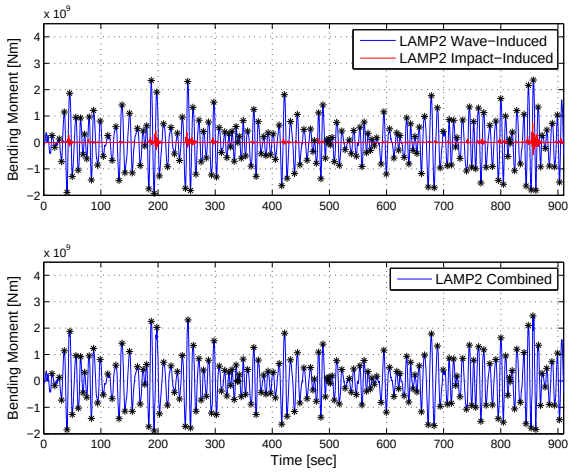

(b) Wave-Induced Bending, Impact-Induced Bending, and Combined Bending

Figure 6.5: Example Nonlinear Monte Carlo Simulations [Sea State 7, 15 knots, Head Seas]

Monte Carlo simulations. Specifically, the total simulation is divided into 200 segments such that the single segment represents 3.75 hour Monte Carlo simulations. The set of the maximum in 200 segments is illustrated as a histogram, as shown in Fig. 6.8. The ratio of the maximum sample to the minimum sample in the histogram is approximately 1.6935 to 1. This ratio will somewhat decrease as the exposure time increases from 3.75 hours to, for example, 750 hours, but the variability can be still quite significant. Similar to the deviation in Table 6.2, this variability can result in a significant difference when extrapolated to relatively long-term extreme values. This

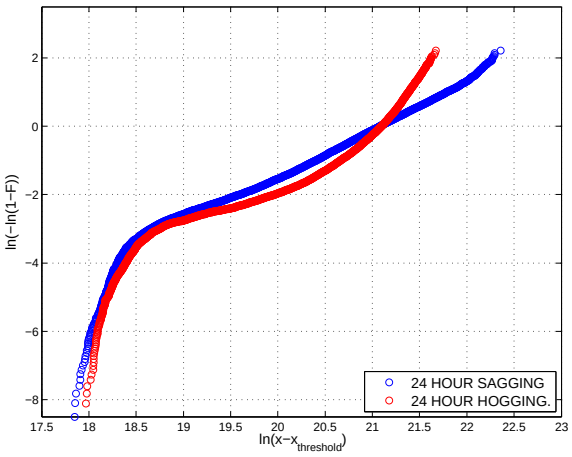

Figure 6.6: 24 Hour Composite Monte Carlo Simulation of LAMP2 Nonlinear Wave-Induced Midship Bending Moments in Weibull Space [Sea State 8, 23 knots, Head Seas]

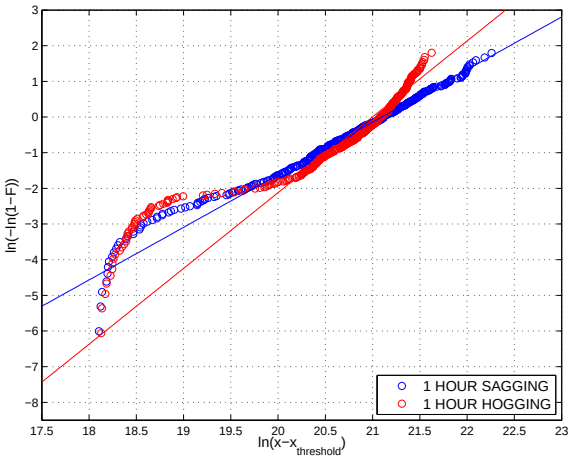

Figure 6.7: 1 Hour Composite Monte Carlo Simulation for Nonlinear Wave-Induced Midship Bending Moments [Sea State 8, 23 knots, Head Seas; Sagging: $\beta = 1.475, \eta = 1.453 \times 10^9$ [Nm], $x_{\text{threshold}} = 0$; Hogging: $\beta = 2.126, \eta = 1.314 \times 10^9$ [Nm], $x_{\text{threshold}} = 0$]

variability has been explained using the idea of PNE in Sec. 2.3, and the variability is what the DLG model does capture. Thus, the shortcomings associated with the Monte Carlo approach can be removed or minimized with the DLG approach, which will be presented in the next section.

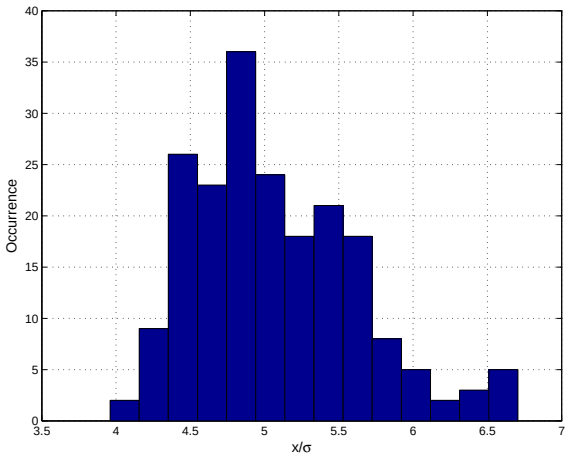

Figure 6.8: Histogram of Maximum in 3.75 Hour Composite LAMP2 Monte Carlo Simulations of Wave-Induced Midship Bending Moments [Sea State 8, 23 knots, Head Seas; $x_{\text{threshold}} = 0$]

6.4 DLG Simulations

The Monte Carlo simulation results introduced in the previous section are processed in various ways such that they can be compared with the DLG results, and eventually validate the DLG results to the extent possible. The DLG results in this section are derived from the LAMP2 simulations of the short incident wave profiles identified by DLG. These results are simply denoted as DLG, because the Monte Carlo simulation results are also based on LAMP2. However, when necessary, the results are denoted as DLG+LAMP, too. For example, Fig. 6.9 shows an example 5σ DLG realization.

To show an overall comparison, the 24 hour composite Monte Carlo simulation discussed in the previous chapter is presented in Weibull space with the DLG results of four different TEVs (3.5, 4.25, 5.0, and 5.25) in Fig. 6.10. For each TEV case, 30 realizations are collected (a total of 120 DLG realizations) through a process illustrated in Fig. 6.9. Here, the standard deviation of the linear rigid body midship bending is denoted as σ. According to Eq. (2.18), the 3.5σ, 4.25σ, 5.0σ, and 5.25σ values correspond to the design bending values for approximately 1 hr, 21 hr, 667 hr, and 2399 hr exposure times, respectively. The averages of the 30 DLG sagging results of 3.5σ and 4.25σ are close to the actual Monte Carlo simulations. Judging by the overall tendency, it is not unreasonable to assume that the longer Monte Carlo simulation would pass the points close to the averages of the 30 DLG sagging of

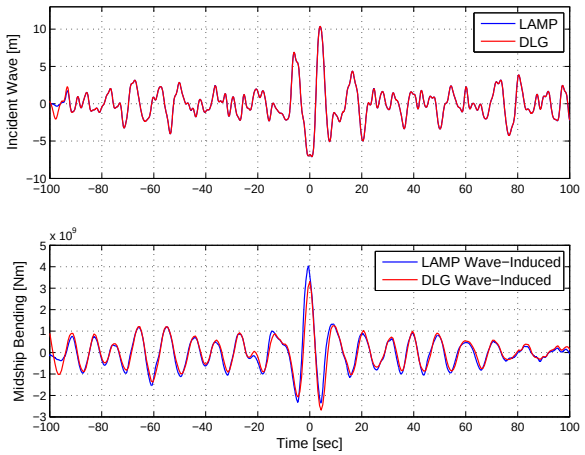

(a) Incident Wave and Wave-Induced Bending

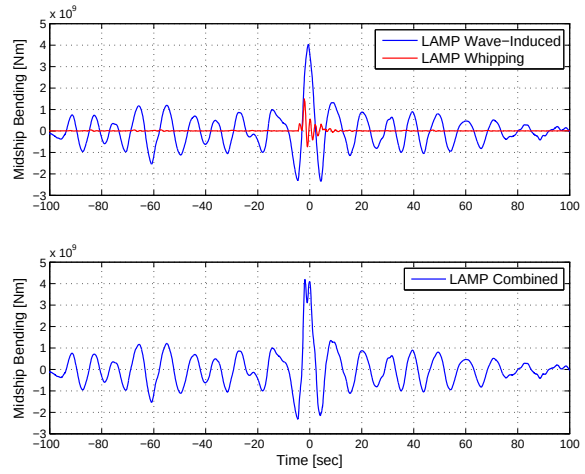

(b) Wave-Induced Bending, Impact-Induced Bending, and Combined Bending

Figure 6.9: Example DLG realization of 5.0σ Event and Corresponding LAMP2 Calculation [Sea State 7, 15 knots, Head Seas]

3.5σ and 4.25σ as well. However, the linear extrapolation of a short term (e.g., one hour) Monte Carlo simulation in Weibull space is likely to over-predict the extreme wave-induced bending moments for this operational condition.

The DLG hogging results are lower than the Monte Carlo results because the DLG realizations are obtained from an ensemble of short-time wave environments that produce extreme sagging moments, as opposed to hogging moments. These results should be understood as a lower bound of the "true" hogging extreme values, which will be discussed again in Secs. $6.7 \sim 6.8$.

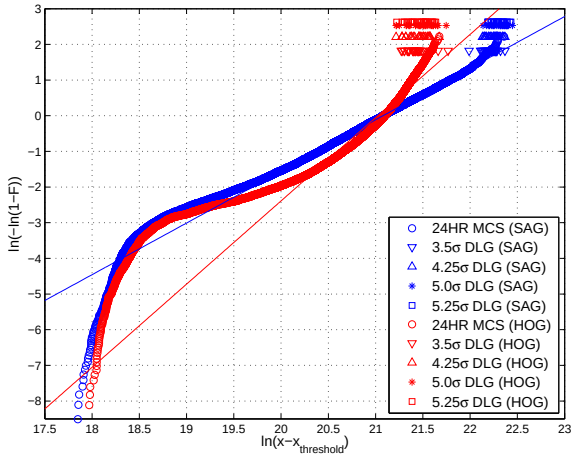

(a) Weibull space

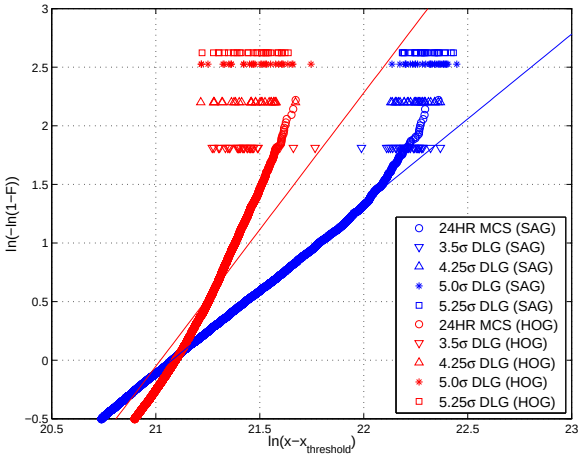

(b) Enlargement

Figure 6.10: DLG Predictions and 24 Hour Monte Carlo Simulation (MCS) for Rigid Hull Midship Bending [Sea State 8, 23 knots, Head Seas; Sagging: $\beta = 1.448, \eta = 1.426 \times 10^9$ [Nm], $x_{\text{threshold}} = 0$; Hogging: $\beta = 2.334, \eta = 1.349 \times 10^9$[Nm], $x_{\text{threshold}} = 0$]

The whipping bending moment is also calculated for the 24 hour Monte Carlo simulation to be compared with the whipping bending moment of the 120 DLG realizations, as shown in Fig. 6.11. The effect of whipping for this operational condition is shown to be significant. Specifically, the maximum combined bending during the 24 hour Monte Carlo simulation is approximately 1.45 times the value realized solely through rigid wave-induced bending. As in the case of rigid hull bending, the combined wave bending and whipping Monte Carlo results are in the very range of the

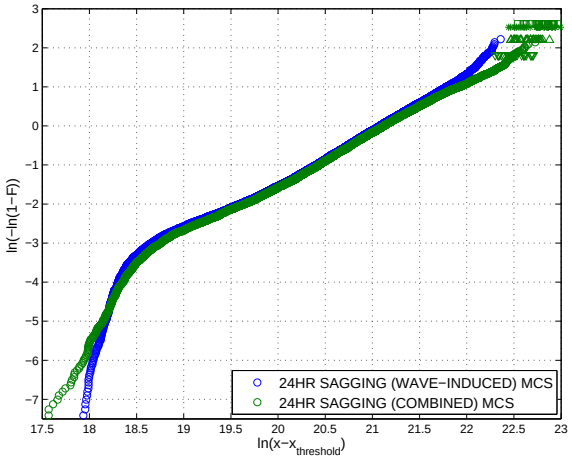

(a) Weibull space

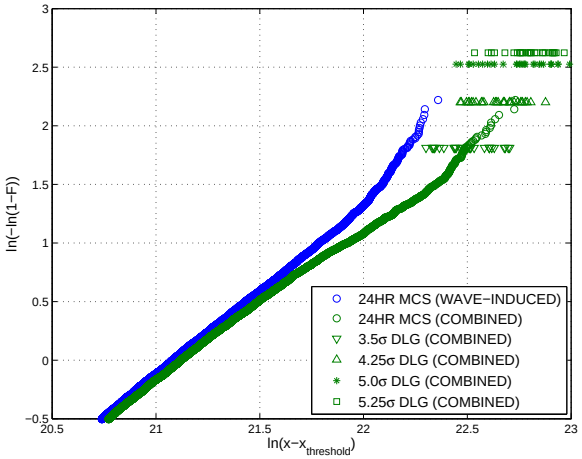

(b) Enlargement

Figure 6.11: DLG Predictions and 24 Hour Monte Carlo Simulation (MCS) for Combined Midship Bending [Sea State 8, 23 knots, Head Seas; $x_{\text{threshold}} = 0$]

DLG predicted values, while the statistical extrapolation based on one hour Monte Carlo simulation would result in a significant over-prediction.

6.5 Lifetime Extreme Loads of A Cell

In this section, the lifetime extreme load of the SS7 condition defined in Table 6.1 is studied in three different ways: the Weibull extrapolation, the DLG analysis, and the Monte Carlo simulations. As an example of the Weibull extrapolation, a 1 hour model test introduced in Table 6.2 is extrapolated, using Eq. (5.7), to the estimated

length of time (D_i = 954 hours) the JHSS is expected to spend in this operational cell in its lifetime. The extrapolated value generated by Eq. (5.7) corresponds to a given PNE value. Three PNE values (i.e., 0.368, 0.990, and 0.999) are used in the extrapolation. As explained in Sec. 5.3, the PNE of 0.368 is close to e^{-1}, which corresponds to the modal value of the theoretical extreme value distribution.

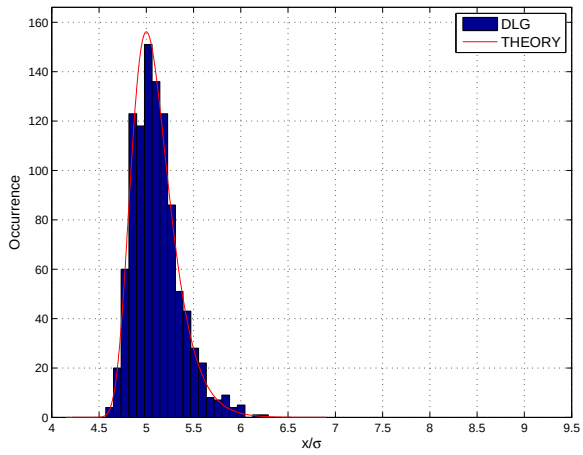

Figure 6.12: Comparison between Histogram from 1000 DLG Realizations and Theoretical Extreme Value Distribution of 5σ Event [Sea State 7, 15 knots, Head Seas]

Collected together are the DLG realizations that represent the same exposure time. The exposure time D_i = 954 is approximately equivalent to TEV = 5 in this cell, when the mean period and the broadness parameter of the linear response spectrum are used in Eq. (2.18). Before applying LAMP to DLG realizations, the comparison between the theoretical extreme value distribution and the histogram of the 1000 DLG realizations is examined, as shown in Fig. 6.12. Due to the development made in Chapter III, the DLG realizations now exactly follow the theoretical extreme value distribution in the limit of infinite realizations. The wave-induced bending and the combined bending moments associated with these 1000 DLG realizations are then obtained as shown in Fig. 6.9. The results of the process are presented as two histograms in Fig. 6.13. Note that the bin widths used in Figs. 6.12 $\sim$ 6.13 are identical.

The results obtained so far are summarized in Table 6.3. The DLG+LAMP results indicate that bending moments are higher, for each PNE, than those from the extrapolated value (Weibull Based Prediction). Since two results are subject to dif-

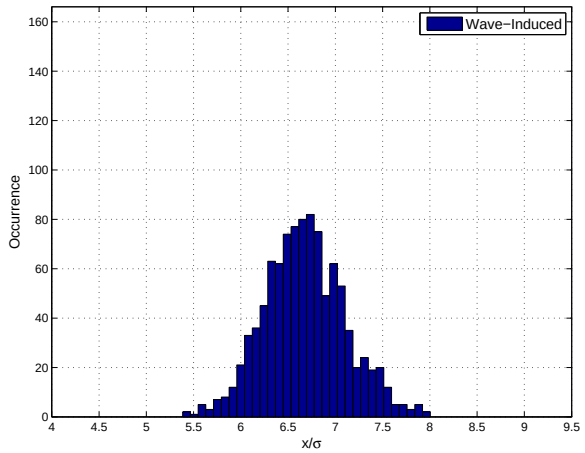

(a) Wave-Induced Bending

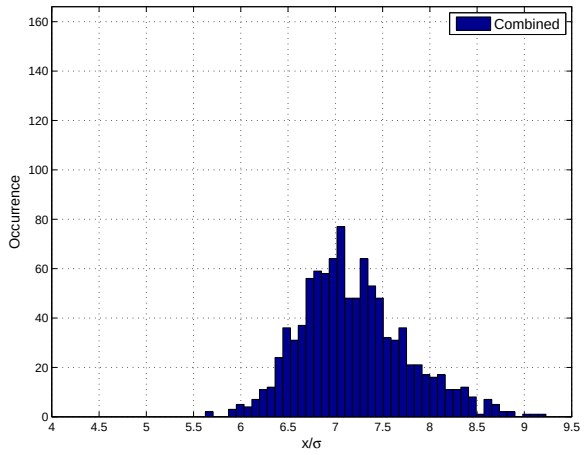

(b) Combined Bending via LMPOUND

Figure 6.13: Histograms from 1000 DLG Realizations of 5σ Event [Sea State 7, 15 knots, Head Seas]

Table 6.3: Comparison of Model Test Predictions from Weibull Analysis (954 Hours) with 5σ DLG Predicted Maximum [Midship Bending [Nm], Sea State 7, 15 knots, Head Seas]

Weibull Based Predictions			DLG+LAMP Based Predictions		
PNE	Wave-Induced	Combined	PNE	Wave-Induced	Combined
0.368	3.56E+9	3.82E+9	0.368	4.50E+9	4.80E+9
0.990	4.25E+9	4.57E+9	0.990	5.37E+9	5.97E+9
0.999	4.57E+9	4.94E+9	0.999	5.51E+9	6.33E+9

ferent uncertainties, it is hard to pinpoint the source of the deviation exactly. For the Weibull extrapolation, as Table 6.2 shows, 259 peaks were recorded in the model test corresponding to an exposure time of approximately 60 minutes in full scale. Based on this relatively short record, four Weibull parameters were determined, as presented in Table 6.2. Then, assuming that the process and the contributing physics remain unchanged, extreme values associated with an exposure time of 954 hours were extrapolated. The results may have been influenced by the shortcomings of the statistical extrapolation, which will be discussed again in Sec. 6.6. The issue with DLG+LAMP relates to the ability of the LAMP program to accurately capture the physics of a vessel experiencing a 5.0σ event. The graphic display of a representative DLG+LAMP simulation shows steep non-breaking waves, excessive water-on-deck, and large bow emergence followed by severe impact. Both of these issues potentially affect the accuracy of extreme value predictions. Although LAMP in general has been shown to generate reliable and consistent results, it remains the subject of continued research. The uncertainties notwithstanding, the comparison in general may be viewed as favorable. Unlike the Weibull predictions where the physics associated with the extreme values has been lost, the DLG simulations, have produced 1000 complete pressure maps under irregular seaways, which may be used in subsequent Finite Element (FE) structural analysis.

Notwithstanding the differences between the two methods, it may be possible to draw qualitative conclusions regarding the contributions of nonlinearities and of whipping to extreme bending moments for the operational cell in Table 6.3. This is because the observation is consistent between the Weibull Based Predictions and the DLG + LAMP simulations. The histogram in Fig. 6.13 is the basis for the statistics shown in the DLG+LAMP columns of Table 6.3. Noting again that the standard deviation σ for the DLG ensemble associated with the TEV = 5 design event is about 6.89×10^8 [Nm], the most probable (i.e., modal value) DLG extreme wave-induced bending moment, based on linear theory, is about 3.44×10^9 [Nm]. The modal value of the histogram based on the nonlinear LAMP2 simulations shown in Fig. 6.13 is about 4.6×10^9 [Nm], which means that the ratio of the most probable 954 hour LAMP2 wave-induced bending moment to the 954 hour DLG wave-induced bending moment is approximately 1.34, a 34% increase due to the nonlinearities captured by the LAMP2 model. Under this operational condition, whipping does not play as important a role as when the vessel is subjected to the operational condition illustrated in Fig. 6.11.

The 750 hour composite Monte Carlo simulation introduced previously can also be used to validate two previously mentioned results. Specifically, the results summarized

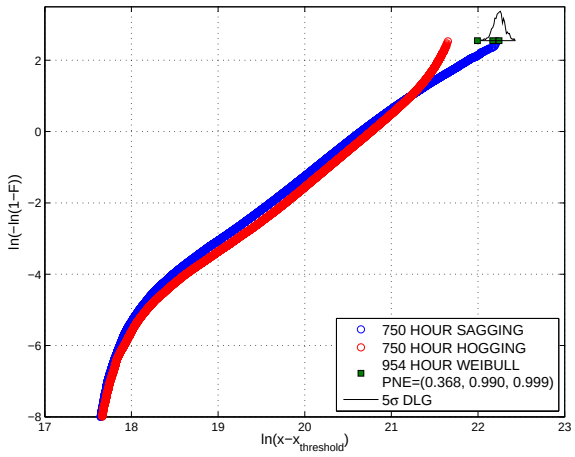

(a) Weibull Space

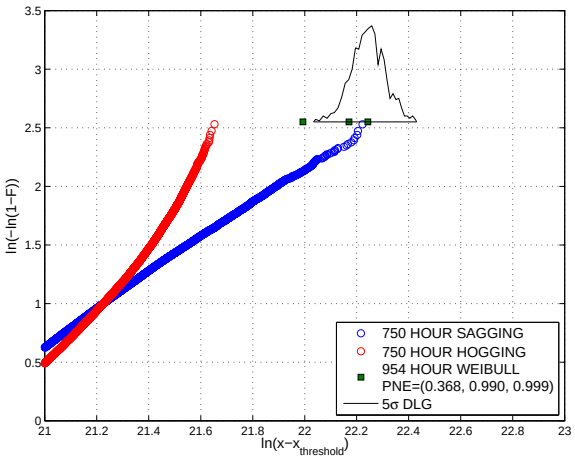

(b) Enlargement

Figure 6.14: Comparison of LAMP2 Wave-Induced Bending Moments from 750 Hour Composite Monte Carlo Simulation, Weibull Extrapolation from 1 Hour Experiment, and 1000 5σ DLG Realization [Sea State 7, 15 knots, Head Seas; $x_{\text{threshold}} = 0$]

in Table 6.3 and illustrated in Fig. 6.13 are compared with the Monte Carlo simulation in Figs. 6.14 $\sim$ 6.15. In this figure, the maximum in a single 750 hour (composite) Monte Carlo simulation is larger than the value that corresponds to the PNE of 0.99 of the 954 hour extrapolated extreme value. However, the maximum value is consistent with the distribution from the DLG 5σ extreme value distribution in the sense that the maximum of the 750 hour is approaching the most likely value from the 1000 DLG realizations for both wave-induced bending moments and combined bending

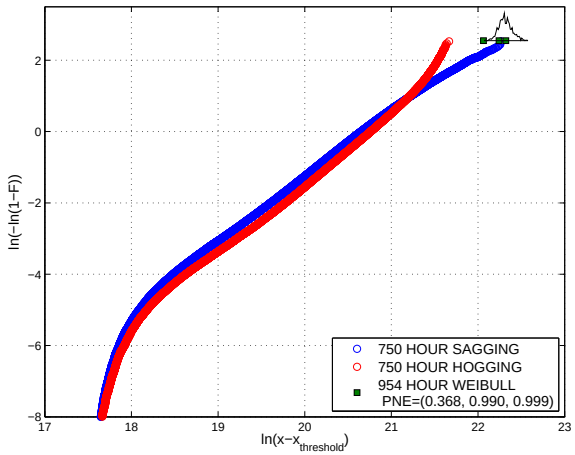

(a) Weibull Space

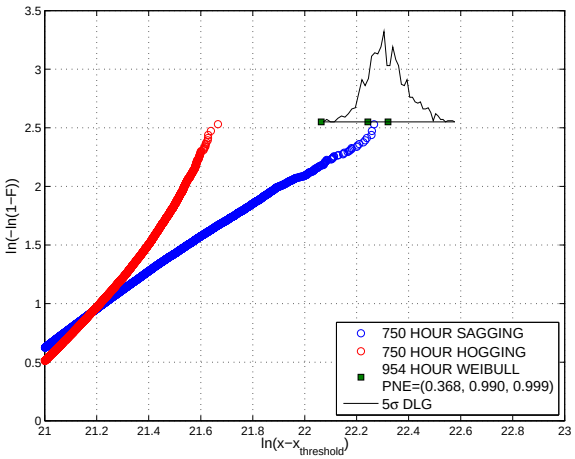

(b) Enlargement

Figure 6.15: Comparison of LAMP2 Combined Bending Moments from 750 Hour Composite Monte Carlo Simulation, Weibull Extrapolation from 1 Hour Experiment, and 1000 5σ DLG Realization [Sea State 7, 15 knots, Head Seas; $x_{\text{threshold}} = 0$]

moments. This suggests that the DLG process works as designed. Figs. 6.14 $\sim$ 6.15 show that the shortcomings inherent in the statistical extrapolation can be reduced or even overcome by the DLG approach.

6.6 Validation of DLG

The ultimate question to be addressed in the chapter is whether the distribution of the nonlinear extreme responses associated with DLG realizations is statistically comparable to the distribution obtained from Monte Carlo simulations. In other words, do the nonlinear extrema found in the vicinity of the linear extrema in a exposure time (DLG+LAMP) closely match the "true" nonlinear extrema (MCS) in the same exposure time?

The challenge with this task is that the extreme value distribution of a high TEV case is very difficult to obtain from MCS. For example, the 1000 realizations of a 5σ event discussed in Sec. 6.5 are equivalent to almost 1 million hours of MCS. Considering that LAMP2 runs much slower than real time, this is clearly beyond the scope of this dissertation. But for a relatively moderate TEV (e.g. TEV $= 3.5 \sim 4$), using the 750 hours' worth MCS introduced in Sec. 6.3, comparing DLG+LAMP with MCS is possible.

To be more specific, the 750 hour composite Monte Carlo simulation is divided into 100 segments and 375 segments such that one segment represents approximately 7.5 hours' and 2 hours' worth simulation, respectively. The maximum in each segment is retrieved to obtain the empirical CDF of extreme values in 2 hours and 7.5 hours. This process is repeated for linear, LAMP2 wave-induced, and combined bending moments, respectively. The results are given as MCS in Figs. 6.16–6.18. Presented simultaneously in each figure are the CDFs from the 500 DLG realizations of which TEV levels are approximately 3.63 and 3.98. These TEV levels correspond to the exposure time of 2 hours and 7.5 hours, according to the mean wave period and the broadness parameter of the response spectrum. The bending moments are all normalized by the variance of linear wave-induced bending moments. The number of samples used to construct the CDFs of DLG results is 500, which is larger than those of MCS. For this reason, the CDFs of DLG results exhibit much smoother shapes.

In general, the DLG generated linear responses match the extreme value distribution of linear bending moments from MCS very well in Fig. 6.16. It should be noted though that DLG slightly over-predicts THEORY for the same CDF level. As the number of samples increases, the matching in this plot will definitely improve, as explained in Chapter III.

The overall comparisons between DLG and MCS for both wave-induced bending and combined bending moments are also very good, as evidenced in Fig. 6.17(a) and Fig. 6.18(a). The excellent matching in the upper tail is significant, because this

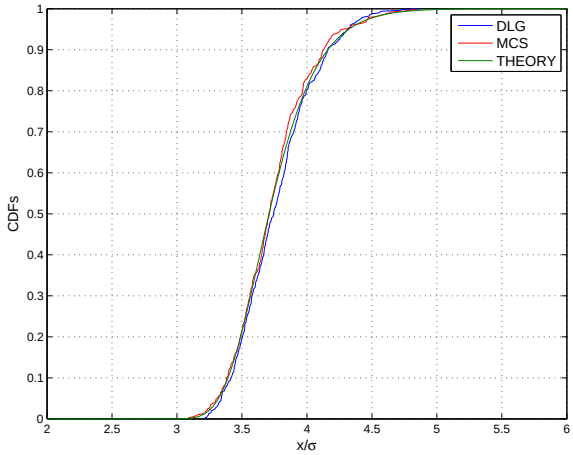

(a) Exposure Time: 2 Hours

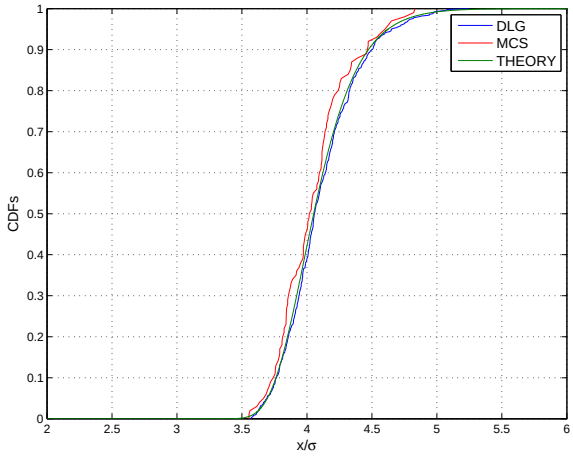

(b) Exposure Time: 7.5 Hours

Figure 6.16: Comparison between Extreme Value Distribution of Linear Bending Moments from Monte Carlo Simulations (MCS) and Corresponding DLG Linear Bending Moments [Sea State 7, 15 knots, Head Seas]

range includes the target point (i.e., a high PNE design event) sought by structural designers. The excellent matching in the upper tail is not a coincidence, which will be explained again in Sec. 6.7. The CDFs are over-predicted by MCS when the CDF level is below 0.3, in Fig. 6.17(a) and Fig. 6.18(a). This is consistent with the tendency observed in Monte Carlo simulations, which will also be discussed in the next section. The under-prediction of MCS when the CDF level is between, say, 0.3 and 0.8 may be explained, to a degree, by the under-prediction of MCS in Fig. 6.16(a) in the similar CDF range.

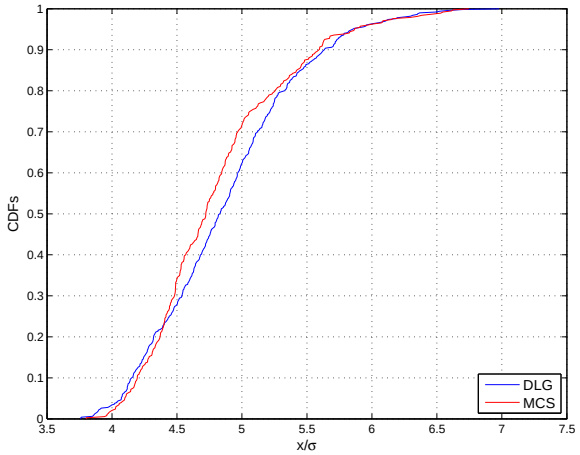

(a) Exposure Time: 2 Hours

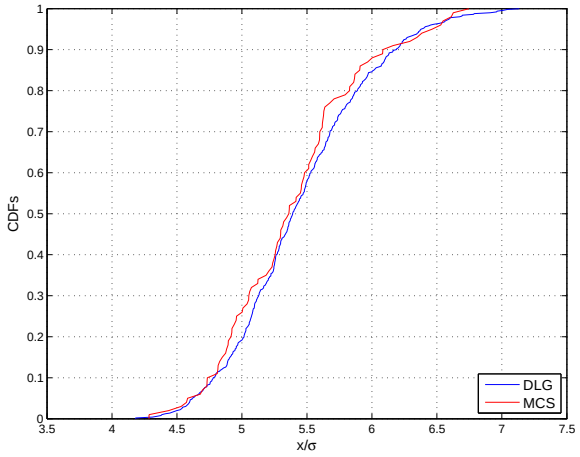

(b) Exposure Time: 7.5 Hours

Figure 6.17: Comparison between Extreme Value Distribution of LAMP2 Nonlinear Wave-Induced Bending Moments from Monte Carlo Simulations (MCS) and Corresponding Nonlinear Wave-Induced Bending in the Vicinity of DLG Linear Extreme Bending Moments (DLG) [Sea State 7, 15 knots, Head Seas]

It is somewhat more difficult to conclusively assess Fig. 6.17(b) and Fig. 6.18(b), due to the small number of samples. The effect of the insufficient number of samples can be seen in linear bending moments between Fig. 6.16(a) and Fig. 6.16(b). It is expected that the level of comparison in Fig. 6.17(b) and Fig. 6.18(b) would improve especially in the upper tail region, if more samples were available. As the exposure time increases further, the comparison may worsen for the same number of samples.

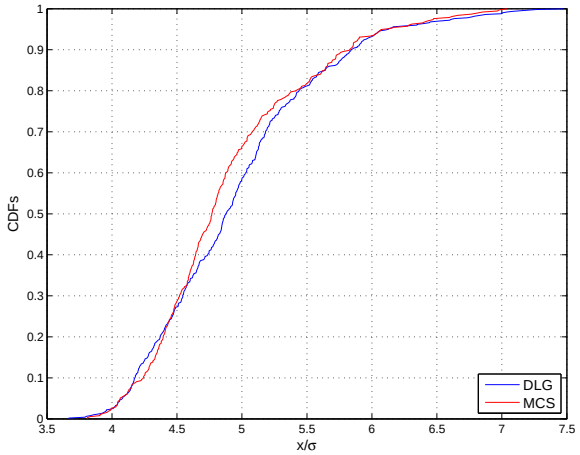

(a) Exposure Time: 2 Hours

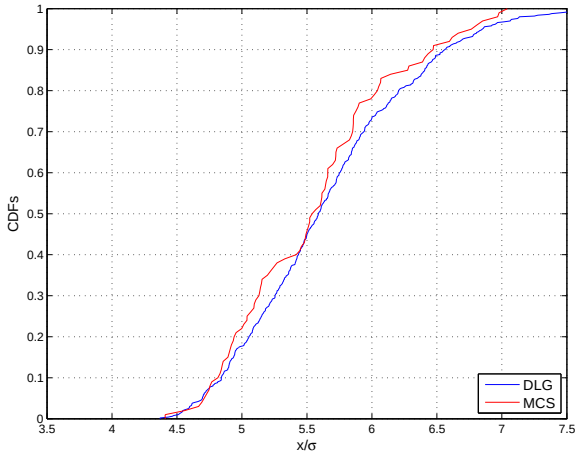

(b) Exposure Time: 7.5 Hours

Figure 6.18: Comparison between Extreme Value Distribution of LAMP2 Nonlinear Combined Bending Moments from Monte Carlo Simulations (MCS) and Corresponding Nonlinear Combined Bending in the Vicinity of DLG Linear Extreme Bending Moments (DLG) [Sea State 7, 15 knots, Head Seas]

However, favorable matching is still expected, which will be explained in Sec. 6.7. These results strongly indicate the validation of the DLG approach in the application of midship bending moments.

The results in this section may be explained in comparison with the correlations between extreme linear bending, extreme wave-induced bending, extreme combined bending moments in the same exposure time, which will be introduced in the next

section. The insights obtained in the next section will provide more confidence to the DLG approach.

6.7 Correlations from Monte Carlo Simulations

The nonlinear extreme response based on the incident wave profile identified by DLG should be understood as a lower bound of the "true" extreme response in the given exposure time. The reason for this can be illustrated using the following diagram.

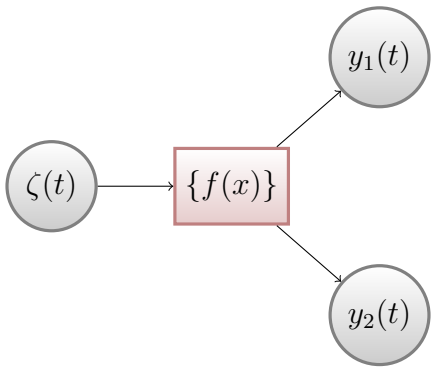

Figure 6.19: Schematic Diagram of Bounding "True" Extreme in DLG

Consider the schematic shown in Fig. 6.19. Input to a system $\{f(x)\}$ is the Gaussian process $\zeta(t)$. In this case, $\{f(x)\}$ may be considered as multiple filters working in parallel. The multiple outputs from the system consist of $y_1(t)$ and $y_2(t)$, where $y_1(t)$ is a linear Gaussian or near-Gaussian process, and $y_2(t)$ is a nonlinear non-Gaussian process. In Fig. 6.20(a), $y_1(t)$ is the linear wave-induced bending, while $y_2(t)$ is the nonlinear wave-induced bending identified by LAMP. Note that $y_2(t)$ becomes $y_1(t)$ in Fig. 6.20(b), where the relation between the nonlinear wave-induced bending and the impact-induced bending is studied.

A procedure for finding the square symbol in $y_2(t)$, which is the maximum of the peaks identified by the zero-upcrossing cycles of $y_1(t)$ in 15 minutes, may be designed. By the definition of the procedure, the maximum of $y_2(t)$ (marked as square) found in the zero-upcrossing cycle that has the maximum of $y_1(t)$ (marked as circle) represents a low bound of the "true" maximum (marked as star) of $y_2(t)$ in the same exposure time. This is a meaningful demonstration, because the time history around the circle may be considered as the time history identified DLG. The time history of LAMP2 nonlinear response associated with the DLG identified time history is comparable to

$y_2(t)$.

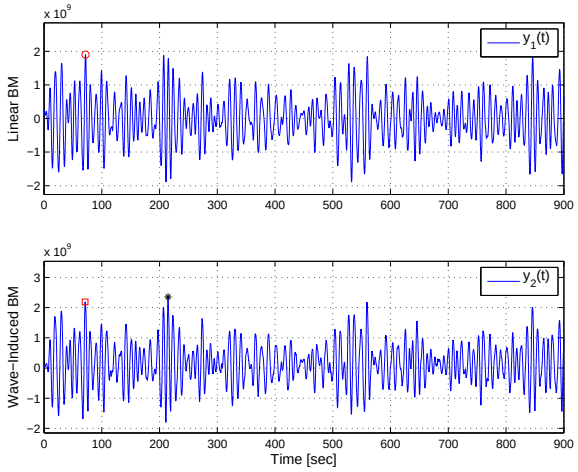

(a) Linear Wave-Induced and LAMP2 Wave-Induced Bending Moments

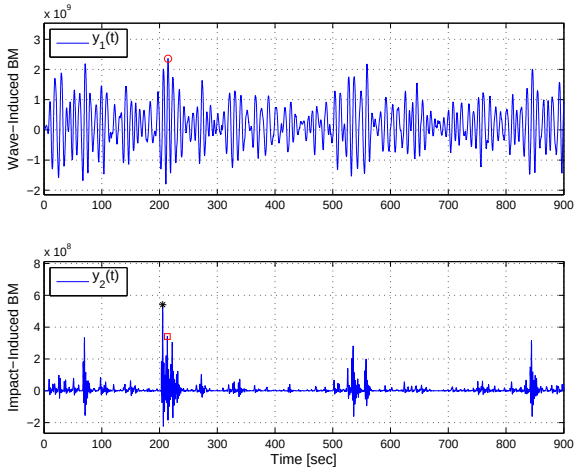

(b) LAMP2 Wave-Induced and Impact Induced Bending Moments

Figure 6.20: Examples of $y_1(t)$ and $y_2(t)$ in Schematic Diagram

By repeating the procedure illustrated in Fig. 6.20, a correlation coefficient between the maximum of $y_2(t)$ in the cycle of the maximum of $y_1(t)$ and the "true" maximum of $y_2(t)$ can be calculated. Moreover, the histogram (or PDF) created from the collection of squares will certainly form a lower bound of the histogram of stars from the same exposure time. The closer the correlation between the extreme of $y_1(t)$ and $y_2(t)$, in general, the more accurate the non-Gaussian maxima based on DLG+LAMP estimates will be in a statistical sense. A high positive correlation co-

efficient is not a sufficient condition to guarantee good matching, because it does not reflect the slope of the relationship. This point will be discussed using the composite Monte Carlo simulation. Different processes will have better or poorer correlations, but the tendency for the collection of squares to form a lower bound of the histogram of stars will remain valid. It should be emphasized that a specific realization that produced the linear maximum is not necessarily the same realization that will produce the non-linear maximum. However, the input $\zeta(t)$ that produced the DLG extreme value statistics will produce a good approximation of the non-Gaussian extreme value statistics.

The procedure is applied to the 750 hour composite Monte Carlo simulation [Sea State 7, 15 knots, Head Seas]. Specifically, the total record length is divided into 100 segments and 375 segments respectively. For each segment, two different time histories (i.e., wave-induced bending, and combined bending) do exist as presented previously. For each time history, three different maxima explained above (i.e., circle, square, and star) are collected. In total, 12 different figures are generated based on the 750 hour composite Monte Carlo simulation, as shown in Figs. 6.21 $\sim$ 6.23. These figures, especially Fig. 6.23, explain why the comparisons were exceptional between the nonlinear response associated with the DLG identified time history and the "true" nonlinear response. Given simultaneously is the correlation coefficient of two random variables in each figure, which is defined by

$$\rho_{XY} = \frac{\mathrm{Cov}[X,Y]}{\mathrm{Var[X]} \cdot \mathrm{Var[Y]}} = \frac{E[(X-\mu_X)(Y-\mu_Y)]}{\sigma_X \sigma_Y} \tag{6.1}$$

where μ_X and μ_Y are the mean of the two random variables X and Y, and σ_X and σ_Y are the variance of X and Y.

Presented in Fig. 6.21 for two different TEVs are the relations between 1) linear wave-induced maximum bending (LWMax) and "true" nonlinear wave-induced maximum bending (TNLWMax), and 2) linear wave-induced maximum bending (LWMax) and "true" nonlinear combined maximum bending (TNLCMax). As the exposure time increases, ρ_{XY} decreases slightly. The correlations for wave-induced bending moments are slightly higher than those of the combined bending moments, where nonlinearity is somewhat more important.

Similarly, in Fig. 6.22, the correlations between 1) LWMax and the associated nonlinear wave-induced maximum bending (ANLWMax), and 2) LWMax and the associated nonlinear combined maximum bending (ANLCMax) are presented. The associated nonlinear maxima, whether it is ANLWMax or ANLCMax, represent the

results from DLG+LAMP, as previously explained.

The most important results are shown in Fig. 6.23, where the relations between ANLWMax and TNLWMax, and between ANLCMax and TNLCMax are presented. Not only are the correlation coefficients higher than those presented in Figs. 6.21 $\sim$ 6.22, ANLWMax and ANLCMax (especially ones with higher magnitude) successfully find many of TNLWMax and TNLCMax exactly. This is why the CDF comparisons in the upper tails are exceptional in Figs. 6.17 $\sim$ 6.18.

In order to be more specific, the CDFs from ANLWMax, TNLWMax, ANLCMax and TNLCMax are generated in Fig. 6.24. Note that TNLWMax and TNLCMax are identical to MCS in Figs. 6.17 $\sim$ 6.18, while ANLWMax and ANLCMax are comparable to the realizations from DLG. Unlike ANLWMax and ANLCMax in Fig. 6.24, the responses from DLG are not always lower than those from MCS in Figs. 6.17 $\sim$ 6.18, which is probably due to the uncertainties introduced by the insufficient number of samples. However, the overall comparison implies that the DLG realizations successfully find not only the theoretical extreme value distribution, but also the backgrounds of the incident wave profiles. In other words, the incident wave profiles identified by DLG are statistically comparable to those identified by MCS.

As the exposure time increases the correlation decreases, but the tendency that ANLWMax and ANLCMax represent the low bounds of TNLWMax and TNLCMax remains true. Therefore, the CDF comparisons between DLG+LAMP and MCS in the upper tails will still be better than those in the lower tails as can be deduced in Fig. 6.25.

6.8 Hogging Bending Moments

As can be deduced from Fig. 6.14, the extreme nonlinear hogging bending moments in general are less Gaussian than the nonlinear sagging bending moments. This will increase the deviation between the nonlinear response associated with the DLG identified events and the "true" nonlinear response. However, as mentioned previously, the tendency that the nonlinear response based on the DLG forms a lower bound of the "true" maximum will remain unchanged, which is shown in Fig. 6.26.

In Fig. 6.26(a), the CDF, denoted as DLG, is calculated from 500 randomly selected realizations of an approximately 3.63σ event. The TEV is slightly different from the sagging example with the same exposure time, because the hogging response amplitude operator is calculated again with LAMP2 using the regular wave inputs, the height of which is equal to the significant wave height. While the statis-

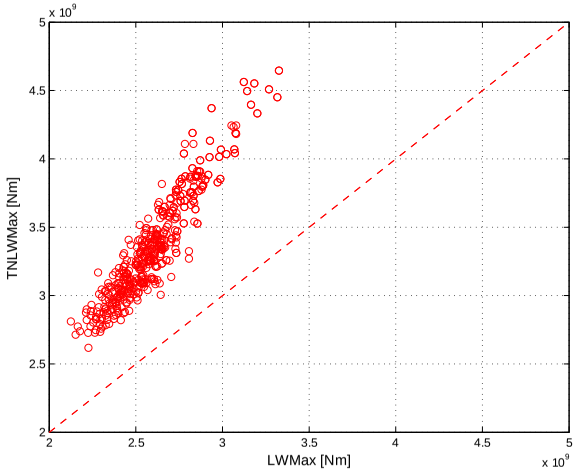

(a) Exposure Time: 2 Hours; $\rho_{XY} = 0.9313$

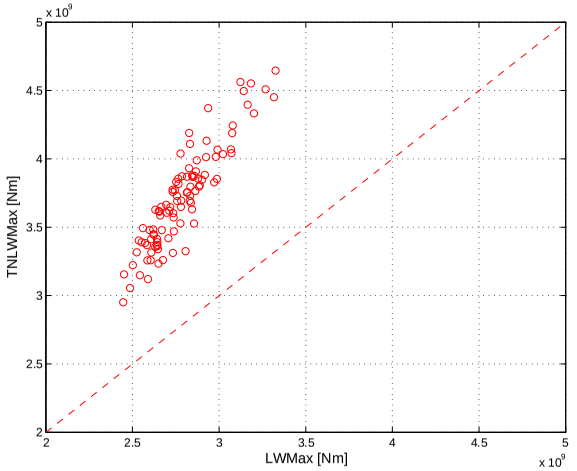

(b) Exposure Time: 7.5 Hours; $\rho_{XY} = 0.9135$

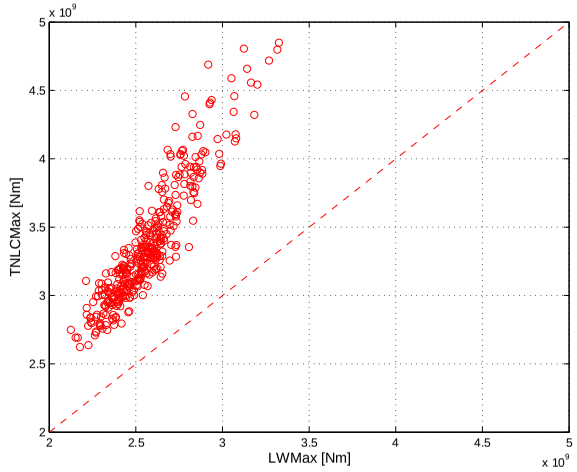

(c) Exposure Time: 2 Hours; $\rho_{XY} = 0.9199$

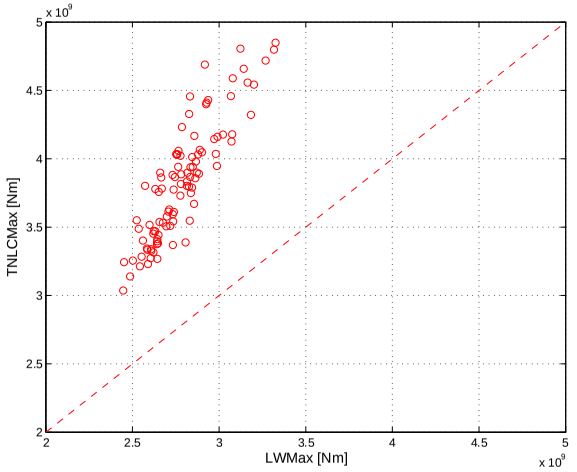

(d) Exposure Time: 7.5 Hours; $\rho_{XY} = 0.8817$

Figure 6.21: Correlations between Linear Maxima and "True" Nonlinear Maxima from MCS

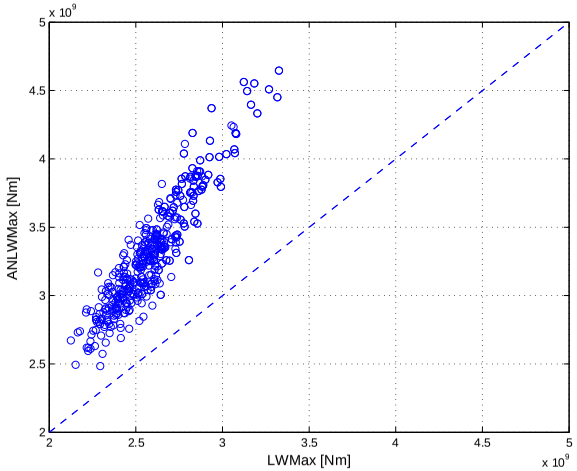

(a) Exposure Time: 2 Hours; $\rho_{XY} = 0.9244$

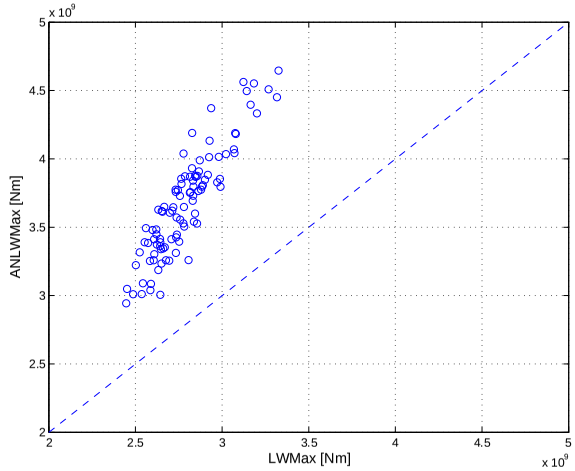

(b) Exposure Time: 7.5 Hours; $\rho_{XY} = 0.9035$

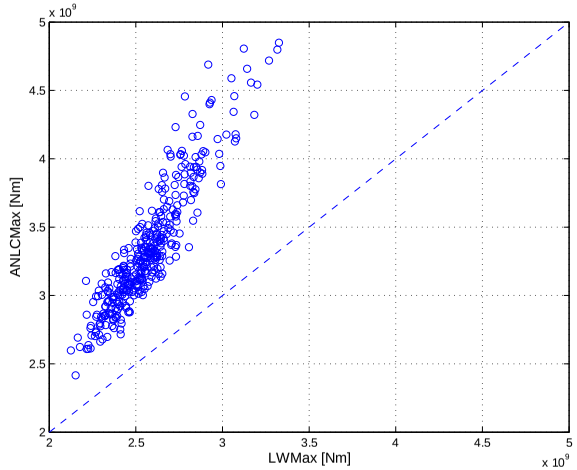

(c) Exposure Time: 2 Hours; $\rho_{XY} = 0.9203$

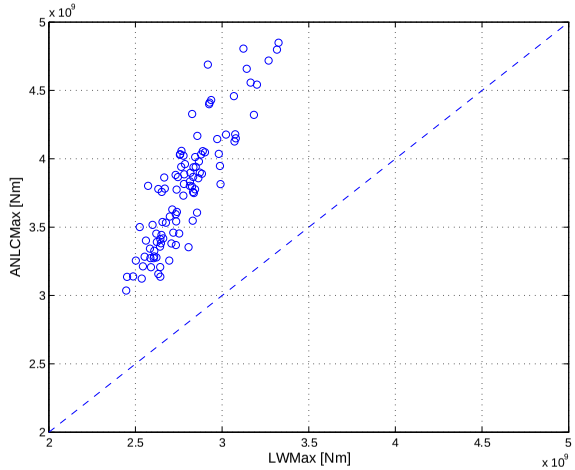

(d) Exposure Time: 7.5 Hours; $\rho_{XY} = 0.8824$

Figure 6.22: Correlations between Linear Maxima and Associated Nonlinear Maxima from MCS

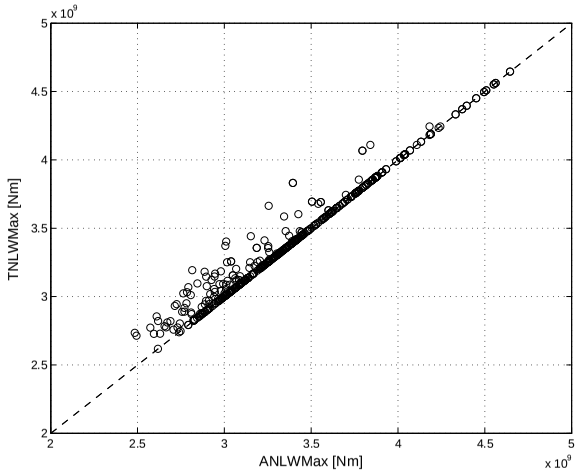

(a) Exposure Time: 2 Hours; $\rho_{XY} = 0.9856$

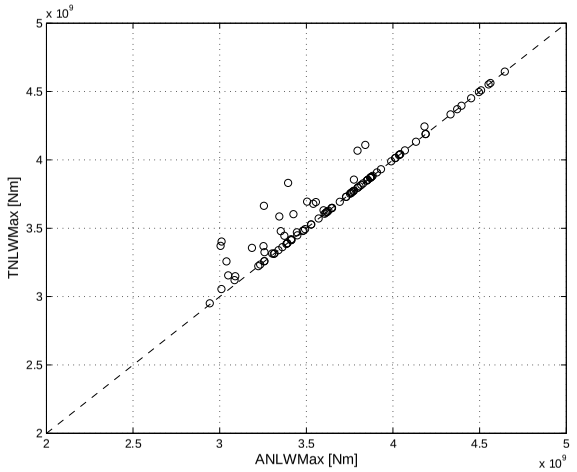

(b) Exposure Time: 7.5 Hours; $\rho_{XY} = 0.9699$

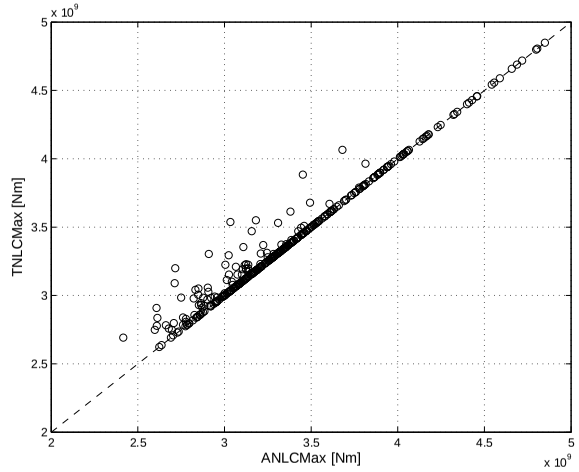

(c) Exposure Time: 2 Hours; $\rho_{XY} = 0.9858$

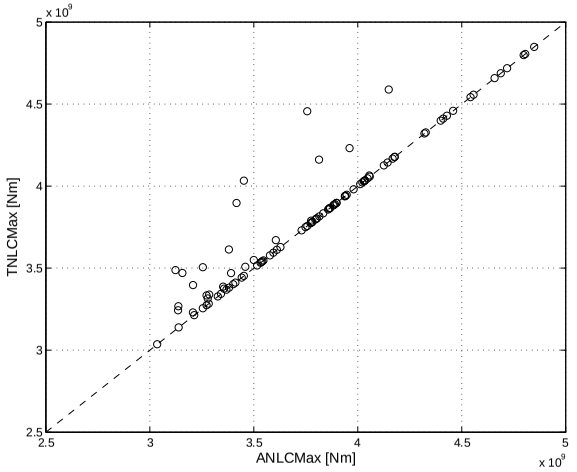

(d) Exposure Time: 7.5 Hours; $\rho_{XY} = 0.9562$

Figure 6.23: Correlations between Associated Nonlinear Maxima and "True" Nonlinear Maxima from MCS

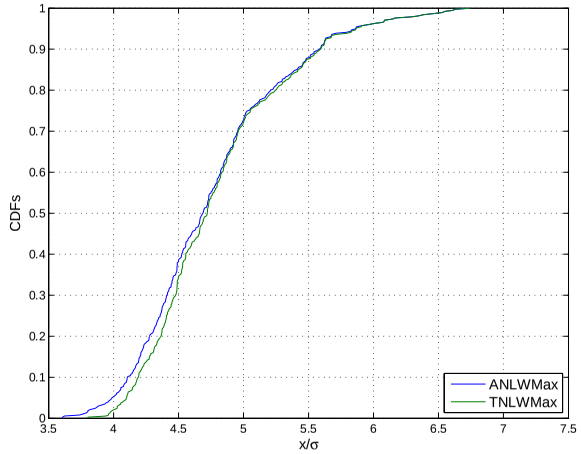

(a) Exposure Time: 2 Hours

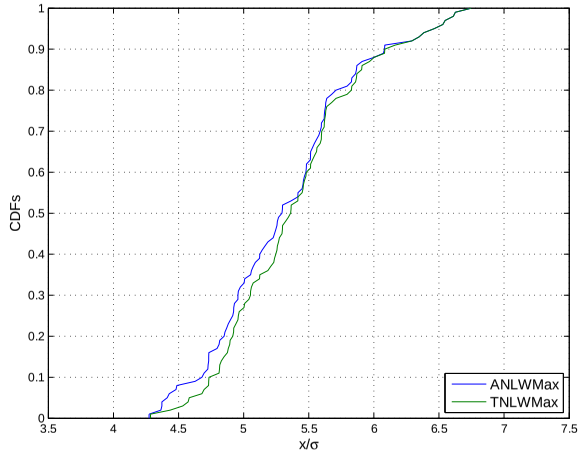

(b) Exposure Time: 7.5 Hours

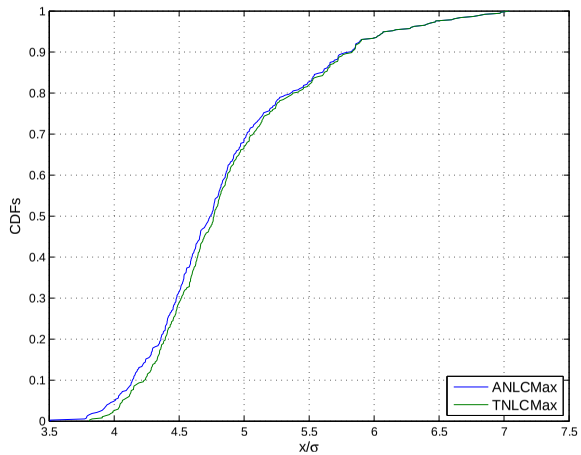

(c) Exposure Time: 2 Hours

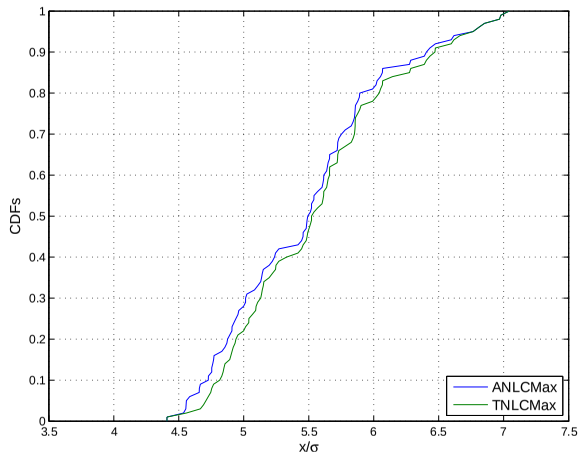

(d) Exposure Time: 7.5 Hours

Figure 6.24: Extreme Value Distributions of Associated Nonlinear Maxima and "True" Nonlinear Maxima from MCS

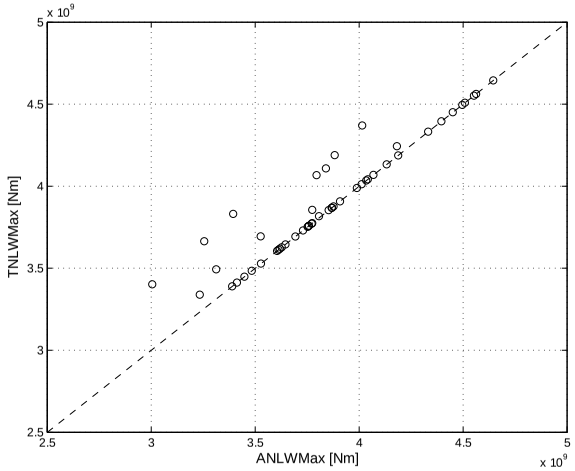

(a) Exposure Time: 15 Hours; $\rho_{XY} = 0.9437$

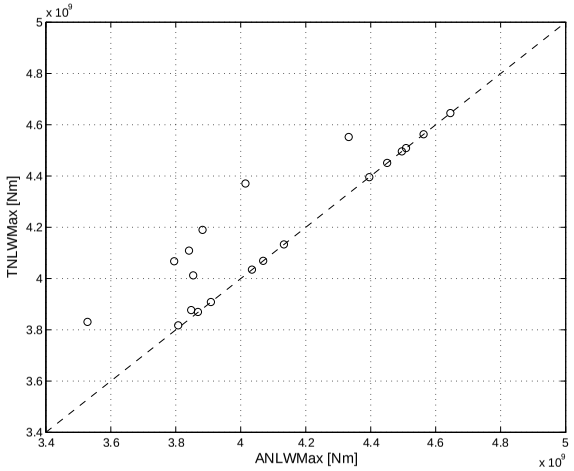

(b) Exposure Time: 37.5 Hours; $\rho_{XY} = 0.9074$

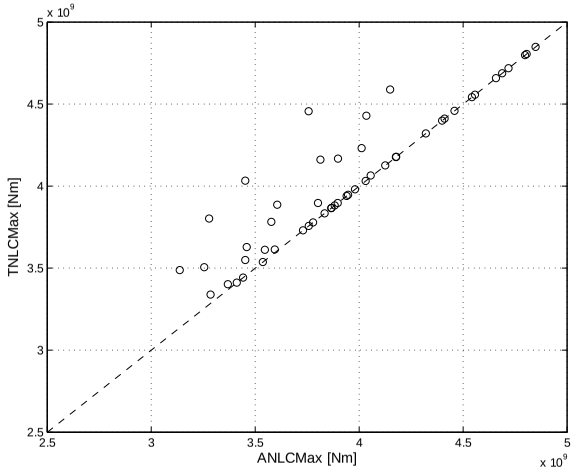

(c) Exposure Time: 15 Hours; $\rho_{XY} = 0.9221$

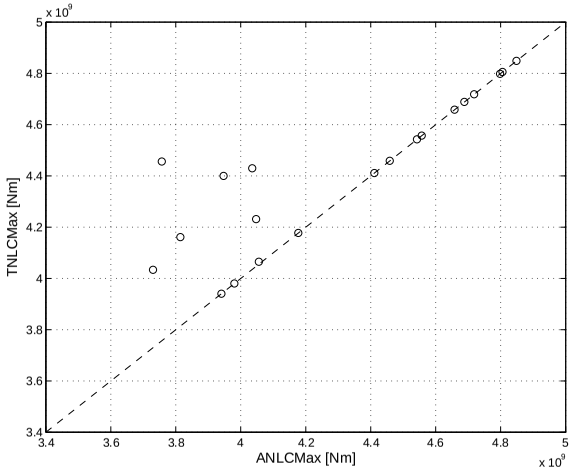

(d) Exposure Time: 37.5 Hours; $\rho_{XY} = 0.8520$

Figure 6.25: Correlations between Associated Nonlinear Maxima and "True" Nonlinear Maxima from MCS

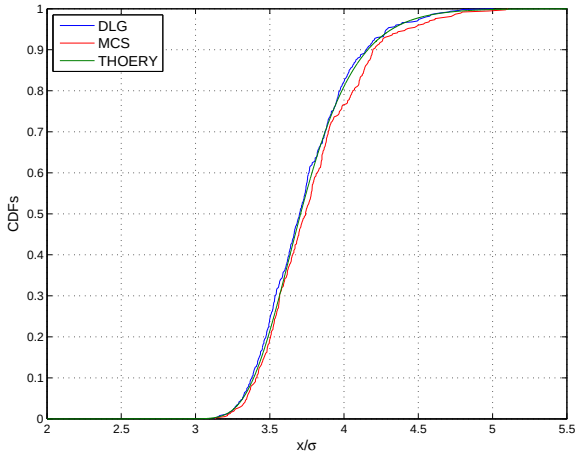

(a) Linear Bending (Exposure Time: 2 Hour)

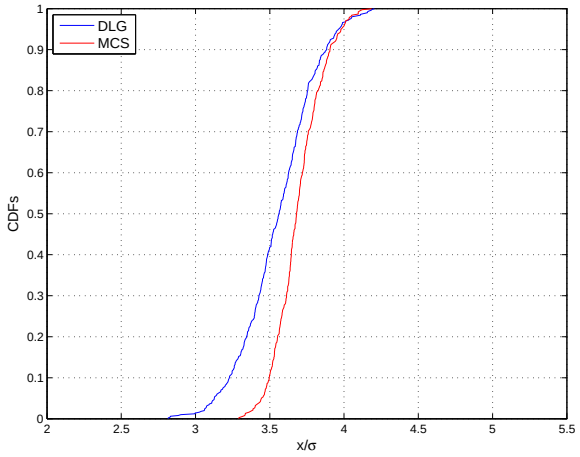

(b) Nonlinear Bending (Exposure Time: 2 Hour)

Figure 6.26: Comparison between Extreme Value Distribution of LAMP2 Wave-Induced Hogging Bending Moments from Monte Carlo Simulations (2 Hours) and Corresponding Wave-Induced Hogging Bending Moments in the Vicinity of DLG Linear Extreme Bending Moments [Sea State 7, 15 knots, Head Seas]

tical linearization may better represent the hogging response amplitude operator, an attempt is not made to show that DLG works as expected, even with the simplified approach. The variance of the corresponding response spectrum is used to calculate the CDF denoted as THEORY. The two CDFs in Fig. 6.26(b) are calculated from LAMP simulations of the incident wave profiles associated with the CDFs in Fig. 6.26(a). Unlike Figs. 6.17 $\sim$ 6.18, the uncertainty introduced by the insufficient

number of samples is not strong enough to "corrupt" the tendency that the response generated by DLG+LAMP represents the low bound of the "true" extreme responses.

6.9 Effects of Whipping to Total Combined Bending

The calculation of whipping requires the application of nonlinear time domain simulations. This is often not an option during a design process. Even if it is, long-term estimates under irregular seaways are not available without resorting to the statistical extrapolation approach. Therefore, whipping is often taken into account as a dynamic loading factor. The results presented in this chapter may be used to assess the contribution of whipping to rigid wave-induced bending when estimating lifetime design values. The recommendations found in the literature are mixed when addressing this issue. Some authors, e.g., Baarholm & Jensen (2004), claim that the whipping contribution is significant. Other authors, e.g., Soares *et al.* (2008), state that the whipping "effect on the global maximum vertical loads at midship are in general relatively small." The results presented so far show that both positions may be valid, depending on the hull form and operating conditions under consideration. For example, the JHSS hull form may experience a significant increase in wave-induced bending due to whipping for the conditions shown in Fig. 6.11 (45% increase in SS8 at 23 knots), or have a small increase in the whipping contribution to total bending for the conditions shown in Table 6.3 ($\sim$10% increase in SS7 at 15 knots).

As shown in this chapter, it may be very difficult to accurately find an increase due to whipping from the statistical extrapolation or simplified equations. However, this is relatively easy and straightforward using the DLG model, thus demonstrating the value of the DLG approach.

CHAPTER VII

Application II: Estimation of Extreme Slamming Pressures

7.1 Bow Slamming Pressure

While the impact-induced bending moment analyzed in Chapter VI acts on the hull girder, the local hull members (e.g., hull plates and transverse frames) are also subject to high impact pressures. Due to their characteristic short duration and extreme local concentration, the impact pressures prove to be particularly troublesome in the design of fast modern ships.

Slamming can occur when two necessary conditions are satisfied: hull emergence, which is related to the high relative motion of a target point on ship hull, and the relative velocity exceeding a certain threshold value. These two conditions were used in Ochi & Motter (1973) to derive the probability of slamming occurrence. In their work, they also estimated the magnitude of the impulsive pressure based on the assumption that the pressure is an exponentially distributed random variable. Although the design process presented in Ochi & Motter (1973) was comprehensive, their study was primarily based on the statistical analysis of slamming per se, rather than input random waves that would cause extreme slamming events. In other words, when advanced nonlinear time domain simulations are required to calculate the impact

Table 7.1: Environmental & Operation Conditions of Slamming Pressure Test Examples

Sea State (SS)	H_s [m]	T_{modal} [sec]	Wave Heading [deg]	Speed [knots]
7	7.5	14	180	15
8	11.5	16.4	180	23

pressure, the input waves leading to the extreme slamming events need to be identified. How this task can be done employing the DLG process is presented in this chapter. The environmental and operating conditions of the test examples presented here are listed in Table 7.1.

The relative motion of a point on a ship hull with respect to the incident wave, in a head/following sea, may be linearly approximated as

$$r(t) = \zeta_3(t) - L\zeta_5(t) - \zeta_0(t) + z \tag{7.1}$$

where $\zeta_3(t)$ is the heave displacement, $\zeta_5(t)$ is the pitch angle in radians, $\zeta_0(t)$ is the incident wave height at the target point, L is the distance between the center of gravity and the point in question, and z is the vertical coordinate (positive upward) of the target point from $z = 0$ (usually mean free surface). The temporal average of $r(t)$ approaches z as the record length increases. In this chapter, the surface pressure at a point near the intersection of the Forward Perpendicular (FP) and the hull bottom, referred to as the target point, is studied using the two sets of the composite Monte Carlo simulations introduced in Sec. 6.3. The longitudinal distance L between the center of the gravity and the target point (L) is 138.55 [m], and the vertical coordinate (Z) of the target point from the free surface is -8.33 [m]. While only bow slamming is studied here, the process employed in this chapter remains valid even for bow flare slamming or stern slamming (Kim *et al.*, 2010) as long as the available hydrodynamic computational tools are capable of calculating those pressures consistently.

7.2 Monte Carlo Simulations

As illustrated in Fig. 7.1, the total surface pressure P_{TOT} may be defined as the summation of three potential pressures P_T and the impact-induced pressure P_I, which are all defined in Eq. 5.2. The peaks of these pressures may be obtained based on the zero-upcrossing cycles of the mean-removed relative motion at the target point. The mean-removed relative motion time history can work as a "clock" to measure the exposure time of the impact pressure P_I as shown in Fig. 7.2. While P_T may be studied using the distribution of these peaks in Weibull space, P_{TOT} is not a suitable target of a typical Weibull analysis as shown in Fig. 7.3. In Fig. 7.3(b), a straight line that passes the point of which vertical coordinate is zero (i.e., the sample approximately equal to the characteristic value η) clearly fails to model the extreme values accurately. This is because two physically different processes are combined

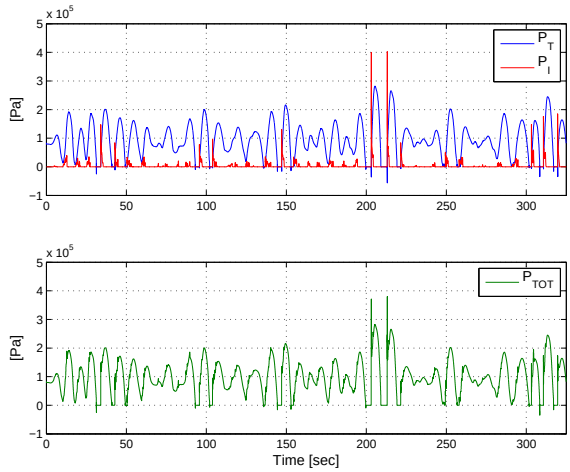

Figure 7.1: Example Time Histories of P_T, P_I, and P_{TOT} [Sea State 8, 23 knots, Head Seas]

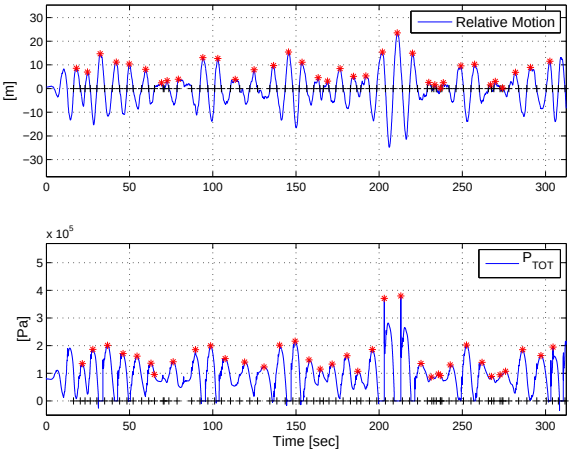

Figure 7.2: Collection of P_{TOT} Maxima Based on Zero-Upcrossing Cycles of Mean-Removed Relative Motion Time History [Sea State 8, 23 knots, Head Seas]

in the total pressure. While the application of two straight lines may be considered in the extrapolation, the results would still be subject to the shortcomings of the statistical extrapolation technique.

The DLG process, however, can be used to estimate the extreme P_T, P_{TOT}, or even P_I, because it does not require any statistical extrapolation technique. As an example demonstration, this chapter focuses on the estimation of P_I, which is a highly nonlinear process. The prediction of the extreme P_I is much more interesting than that of the extreme P_T, because P_T is essentially dominated by the hydrostatic

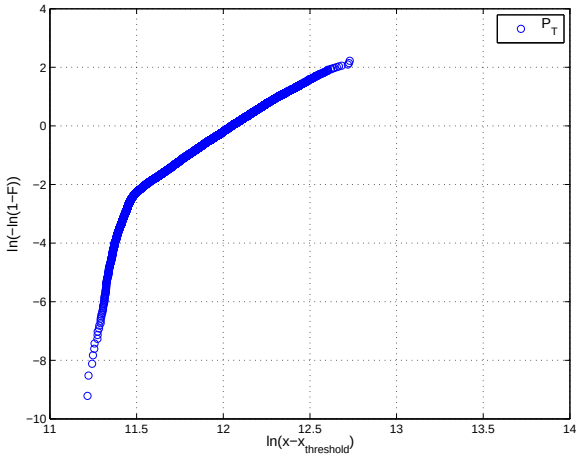

(a) Maxima of P_T in Weibull Space

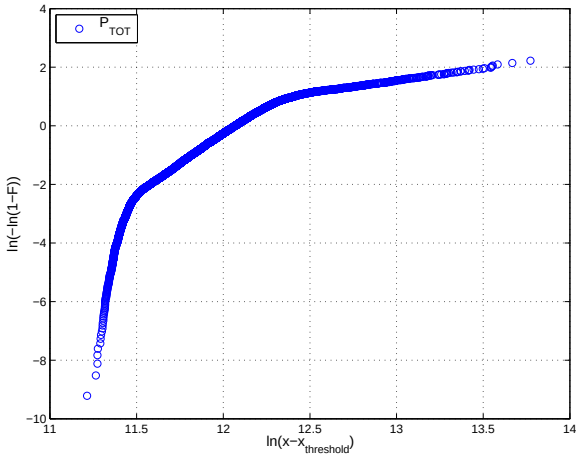

(b) Maxima of P_{TOT} in Weibull Space

Figure 7.3: 24 Hour Composite Monte Carlo Simulation of P_T and P_{TOT}, Associated with Maxima of Relative Motion in Weibull Space [Sea State 8, 23 knots, Head Seas; $x_{\text{threshold}} = 0$]

pressure and the Froude-Krylov pressure.

To assess the highly nonlinear impact pressure P_I, the DLG process uses an indirect method. Specifically, since the conditions under which a marine vehicle becomes conducive to impacts (i.e., hull emergence and extreme negative relative velocity) are known, the DLG process finds an ensemble of short incident wave profiles that will lead the vehicle to experience, for example, an extreme relative motion event at $t = 0$. The ensemble of short incident wave profiles ensures the hull emergence at $t = 0$ so that the target point is likely to experience the impact.

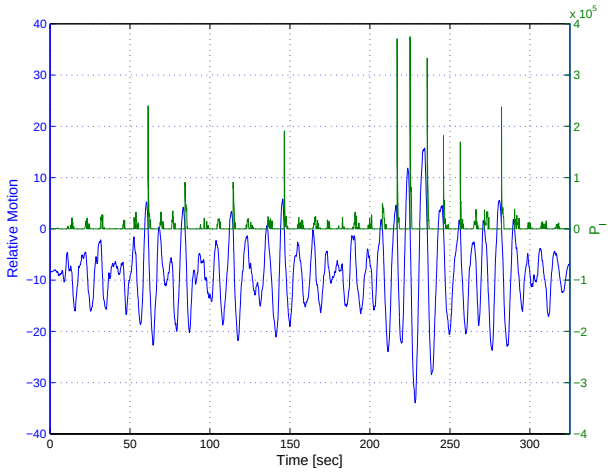

(a) Relative Motion and P_I

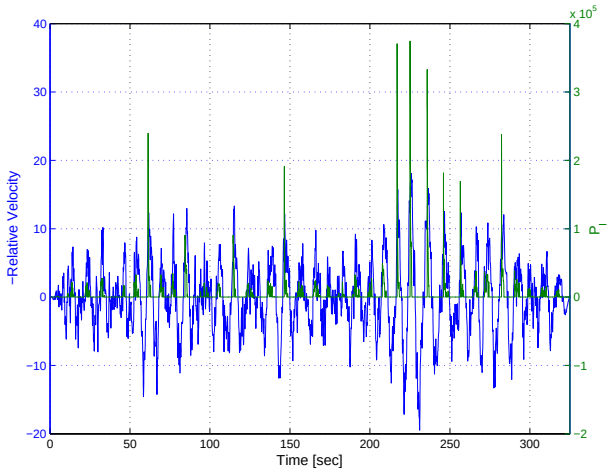

(b) Relative Velocity and P_I

Figure 7.4: Example Time Histories Showing Relationship between Relative Motion, Relative Velocity, and P_I [Sea State 8, 23 knots, Head Seas]

Although this approach does not guarantee the extreme negative relative velocity exceeding a certain threshold value, as TEV increases, the target point becomes more exposed to the extreme negative relative velocity by the time the target point hits the instantaneous water surface. The reason is due to the inherent relation between the relative motion and the relative velocity. This means that the distribution of the hull surface pressure associated with the ensemble of maximum relative motion for a given exposure time should be considered as the low bound of the distribution of "true" extreme pressure, as explained in Sec. 6.7. However, this approach is clearly much more rigorous than, for instance, calculating the maximum pressure associated

with a short regular wave train, in the sense that an ensemble of irregular waves are used. Moreover, the exposure time associated with the ensemble of incident waves is known due to DLG, which is the critical information to designers.

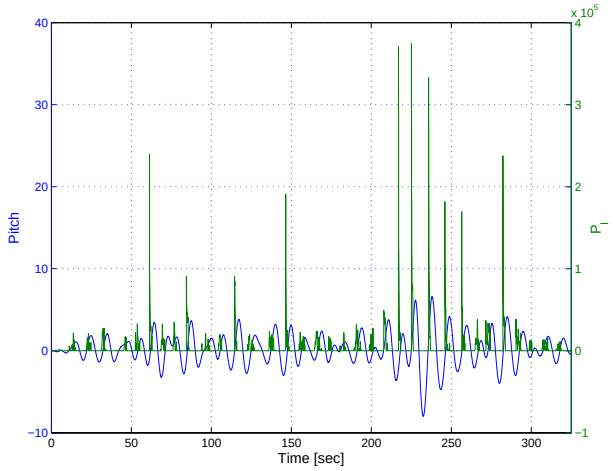

Figure 7.5: Example Time Histories Showing Relationship between Pitch and P_I [Sea State 8, 23 knots, Head Seas]

The relative motion is not the only response with which the impact pressure P_I may be bounded. As mentioned, the extreme negative relative velocity at the target point is a necessary condition for the extreme slamming pressure. Therefore, slamming is expected to happen in the vicinity of the extreme negative relative velocity. Fig. 7.4 shows two example time histories that reveal a relation between the relative motion and the impact pressure, and the relative velocity and the impact pressure. In Fig. 7.4(a), the target point is above the instantaneous free surface in the time interval in which the relative motion is positive. It it clear that the extreme impact pressure P_I is observed when the target point is reentering the instantaneous free surface. In Fig. 7.4(b), the negative relative velocity is used to illustrate the time history to better show the relation between the relative velocity and the magnitude of P_I. In Fig. 7.4(a), two almost identical impact pressure peaks are observed in two consecutive relative motion cycles in which the peaks of the relative motion are quite different. This phenomena may be explained in Fig. 7.4(b), where the relative velocities at the two instances of slamming are nearly equal.

As used in Alford *et al.* (2011), another example response to bound the impact pressure is an extreme pitch event, because an extreme pitch motion is associated with the bow emergence as shown in Fig. 7.5. In this case, the zero-downcrossing period appears to be a better choice than the zero-upcrossing period due to the phase

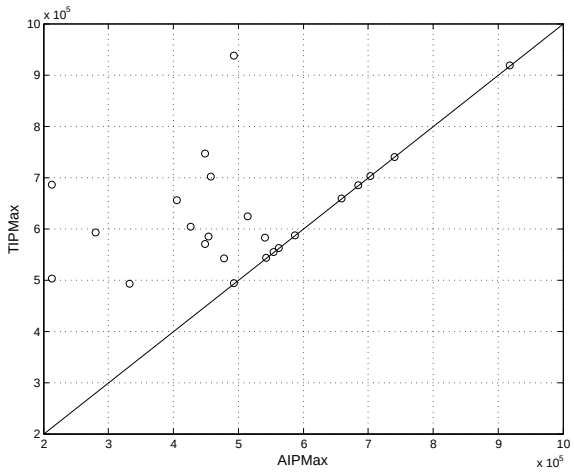

(a) Exposure Time: 1 Hour; $\rho_{XY} = 0.4836$

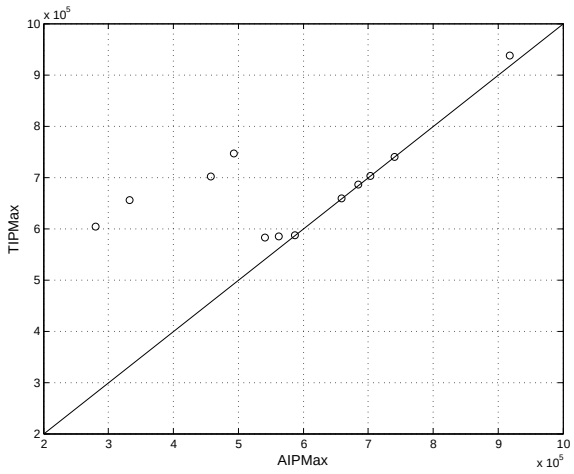

(b) Exposure Time: 2 Hours; $\rho_{XY} = 0.6409$

Figure 7.6: Correlations between Impact Pressure Associated with Relative Motion Maxima (AIPMax) and "True" Impact Pressure (TIPMax) [Sea State 8, 23 knots, Head Seas]

difference.

Among the few different choices discussed above, the relative motion (RM) at the target point is chosen as the clock with which the nonlinear impact pressure P_I can be bounded. The 24 hour composite Monte Carlo simulation under SS8 is used again to generate the composite relative motion time history and the impact pressure P_I at the target point near FP. The simulation results are then divided into 12 and 24 segments to find the maximum peaks in the corresponding operation periods. Similar to the scatter diagrams presented in Sec. 6.7, shown in Fig. 7.6 are the relations between the

"true" extreme impact pressure (TIPMax) and the impact pressure found in the zero-upcrossing cycle of the maximum relative motion (AIPMax) in 1 hour and 2 hours. This figure appears to show that the relative motion was a reasonable choice to bound the highly nonlinear impact pressure following the strategy described in Sec. 6.7. Since the statistical significance is not so high due to the insufficient number of samples in the SS8 example, more samples are collected using the 750 hour composite Monte Carlo simulation under SS7. It should be noted that the impact load calculations of LAMP reasonably well matched the experimental results up to SS7 as discussed in Sec. 6.2.

Presented in Fig. 7.7 are one hour subsets of the peaks of the relative motion and the associated impact pressure collected from the 750 hour composite Monte Carlo simulation. As expected, the relative motion nicely follows the Rayleigh distribution (i.e., the slope parameter β close to 2), as shown in Fig. 7.7(a), but the impact pressure does not. Unlike Fig. 6.7, even a 1 hour composite Monte Carlo simulation does not follow the Weibull assumption. The slope of the curve of P_I appears to be close to 1 around the characteristic value η (Ochi & Motter, 1973), but it decreases to around 0.5 as the curve goes up. Since the slope changes drastically, a typical Weibull parameter estimation is not meaningful. Note that the lowest value of F is different between Fig. 7.7(a) and Fig. 7.7(b), because impacts are not observed for certain time intervals. Although the difference is not significant, the maximum of F associated with the impact pressure is adjusted to that of F associated with the relative motion. The results of the complete 750 hour Monte Carlo simulation will be presented in the next section in comparison with the DLG simulations of two different TEVs.

7.3 DLG Simulations

The results from two different TEVs are presented in this section. For each TEV, 1000 realizations are selected and processed through LAMP and LMPOUND to get the nonlinear relative motion and the associate impact pressure time histories. Of interest is only the impact pressure associated with the peak of the relative motion at $t = 0$. Therefore, the impact pressure calculation through LMPOUND is limited between $t = -30$ and $t = 30$ only.

The two TEVs associated with the ensemble are approximately 3.96 and 4.99, which are equivalent to 7.5 hours and 750 hours, according to the mean period and the broadness parameter of the relative motion response spectrum at the target point. The generation of several thousand realizations that follow the extreme value distri-

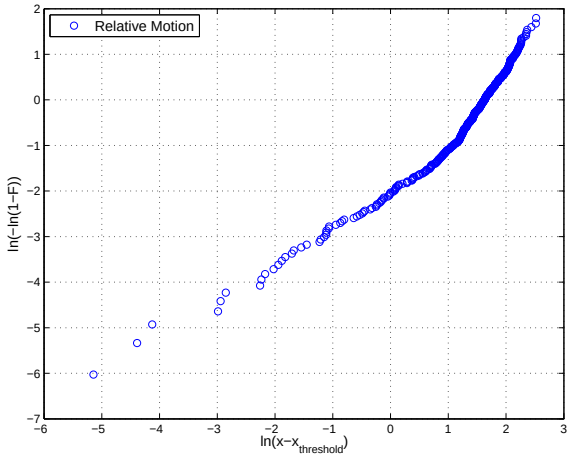

(a) Relative Motion

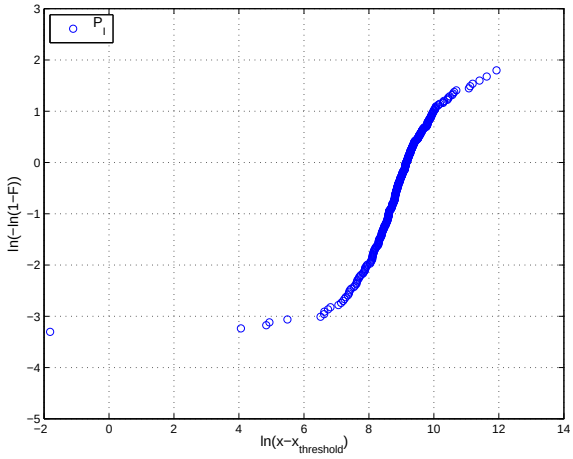

(b) P_I

Figure 7.7: 1 Hour Composite Monte Carlo Simulation of Relative Motion (RM) and Impact Pressure in Weibull Space [Sea State 7, 15 knots, Head Seas; $x_{\text{threshold}} = 0$]

bution associated with the given TEVs can be finished in a matter of a few minutes. Of 1000 realizations randomly selected for the 3.96σ case, the first 20 realizations are presented in Fig. 7.8. The responses at $t = 0$, of course, follow the distribution of the extreme relative motion of the given exposure time at the target point. The ensemble average of the realizations is presented at the same time.

Two set of the 1000 DLG realizations are processed through LAMP2. The result of this process is referred to as DLG. However, the results are denoted as DLG+LAMP, when it is necessary for clarity. An example result from this process is given in

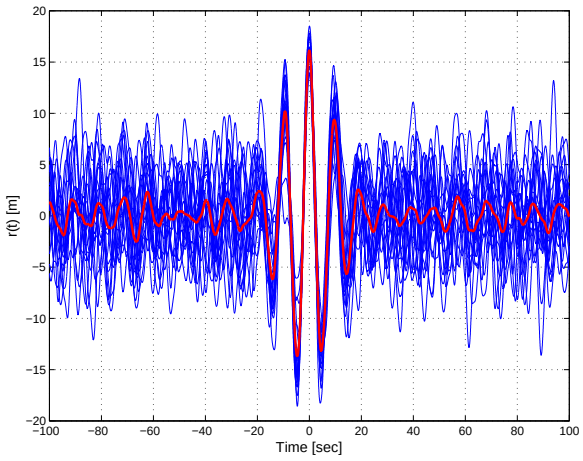

Figure 7.8: 20 Example Time Histories from 1000 DLG Realizations of Mean-Removed Extreme Relative Motion [TEV = 3.96σ Event, Ensemble Average of 20 Time Histories]

Fig. 7.9(a). The comparison between the relative motion predicted by DLG and the relative motion from LAMP2 is very good, because the relative motion retains the characteristic of heave and pitch motions, which are typically represented well by linear theory, even under SS7. As expected, the extreme relative motions lead the vessel to slam. One example is given in Fig. 7.9(b). Note that the temporal average of the relative motion in 7.9(b) approaches the vertical coordinate of the target point from the mean free surface, and the impacts are observed when the target point reenters the instantaneous free surface.

Similar to the process employed for Fig. 7.6, the 750 hour composite Monte Carlo simulation is divided into 100 segments and 375 segments such that each segment represent the random simulations for 7.5 hours and 2 hours, respectively. Collected for each segment are the maximum of the relative motion time history $r(t)$ defined by its mean-removed zero-upcrossing cycles, the extreme impact pressure associated with the maximum relative motion (AIPMax), and the "true" maximum impact pressure found in the entire record length (TIPMax). The sets of maxima collected from this process are presented in Fig. 7.10.

Compared to Fig. 7.6, the number of samples are increased so that a higher statistical confidence level is achieved. The correlation coefficient between AIPMax and TIPMax is much higher than that of SS8. The comparison between AIPMax and TIPMax is perfect for the peaks with high magnitude. The tendency observed in Fig. 7.6 becomes much clearer, even when the exposure time is increased to 7.5

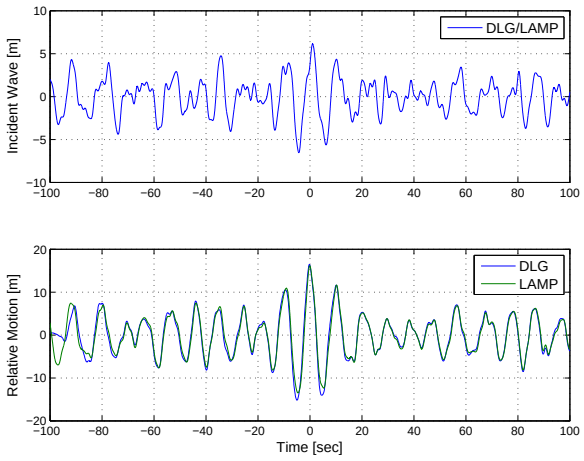

(a) Incident Wave at Midship and Mean-Removed Relative Motion

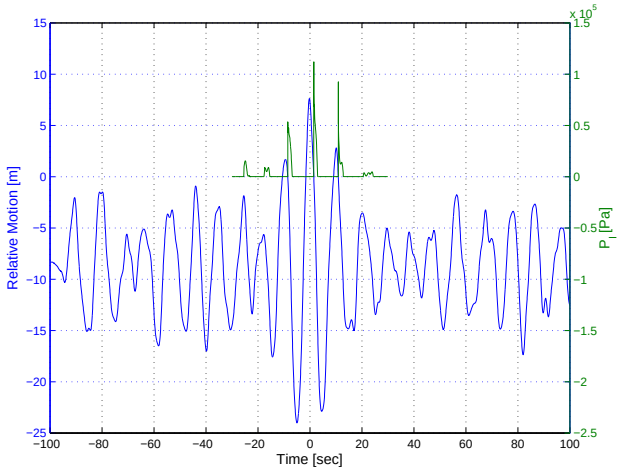

(b) Relative Motion and P_I at the Target Point

Figure 7.9: Example 7.5 Hours DLG Realization Based on Maximum Relative Motion [Sea State 7, 15 knots, Head Seas]

hours. The scatter diagram suggests that the distribution of the impact pressure for a given exposure time can be estimated by the distribution of the impact pressure associated with the extreme relative motion for the given exposure time at the target point. Since the DLG process can find an ensemble of short incident wave profiles extreme responses that follow the distribution of the extreme relative motion for a given exposure time (i.e., comparable to AIPMax), the impact pressure associated with those DLG realizations will follow the distribution of extreme impact pressure (i.e., comparable to TIPMax). The deviation in the comparison of two CDFs is of

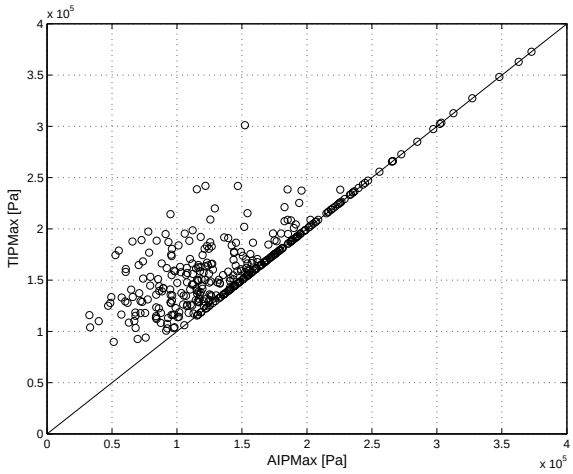

(a) Exposure Time: 2 Hours; $\rho_{XY} = 0.8231$

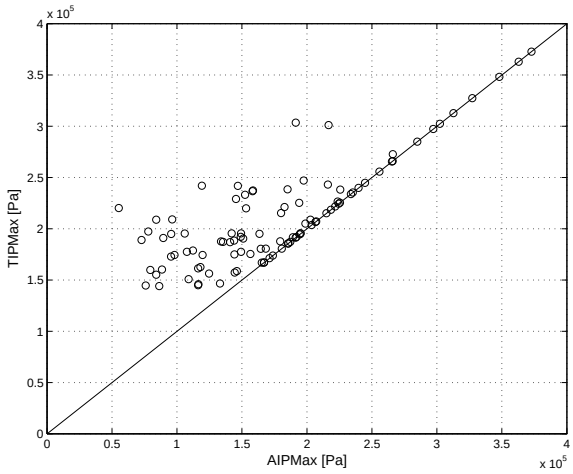

(b) Exposure Time: 7.5 Hours; $\rho_{XY} = 0.8105$

Figure 7.10: Correlations between Impact Pressure Associated with Relative Motion Maxima (AIPMax) and "True" Impact Pressure (TIPMax) [Sea State 7, 15 knots, Head Seas]

course expected, but the scatter diagram suggests the deviation will decrease as PNE increases, to the point where the cycle of extreme relative motion can exactly find the cycle of extreme impact pressure. This is a very promising result, because the peaks with higher PNE values are those sought by designers.

If this tendency remains valid, to a certain extent, as the exposure time increases, the maximum impact pressure from the 750 hour composite Monte Carlo simulation result may be somewhat larger than the most likely value of the 5σ DLG+LAMP impact pressure distribution. The basis of this claim, which is somewhat different

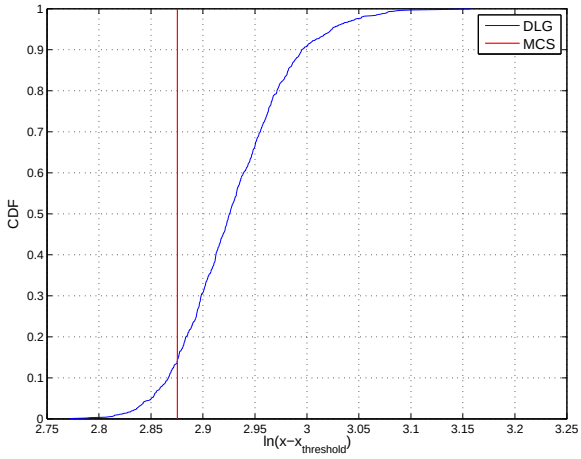

(a) Relative Motion

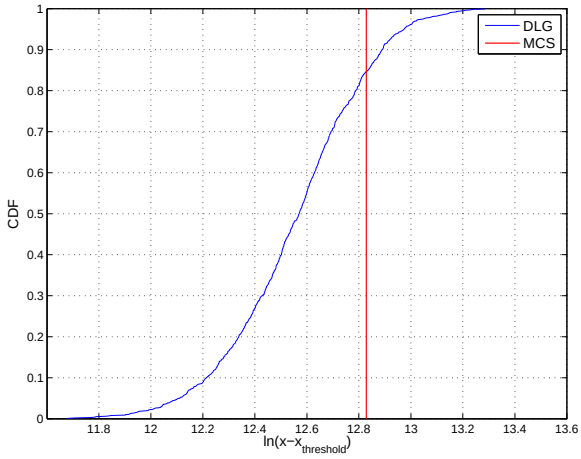

(b) P_I

Figure 7.11: Comparison Between Extreme Value Distributions of 4.99σ DLG Realizations and Maximum of 750 Hour Composite Monte Carlo Simulations [Sea State 7, 15 knots, Head Seas; $x_{\text{threshold}} = 0$]

from the claim made in association with Figs. 6.14 $\sim$ 6.15, is that the correlation coefficients are relatively lower, thus expecting a bigger deviation between AIPMax and TIPMax.

Fig. 7.11 shows the CDF of the relative motion and the CDF of the associated impact pressure constructed from 1000 LAMP2 simulation results of the 4.99σ DLG event. Presented simultaneously is the vertical line that corresponds to the maximum of the 750 hour Monte Carlo simulation using LAMP2. Since the 750 hour composite Monte Carlo simulation produces only one sample, the CDF level cannot be deter-

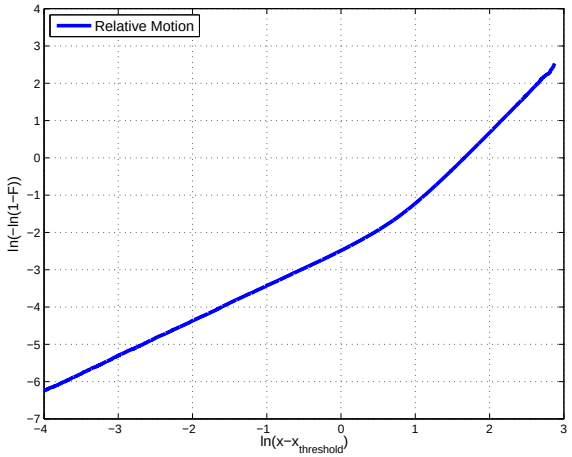

(a) Relative Motion

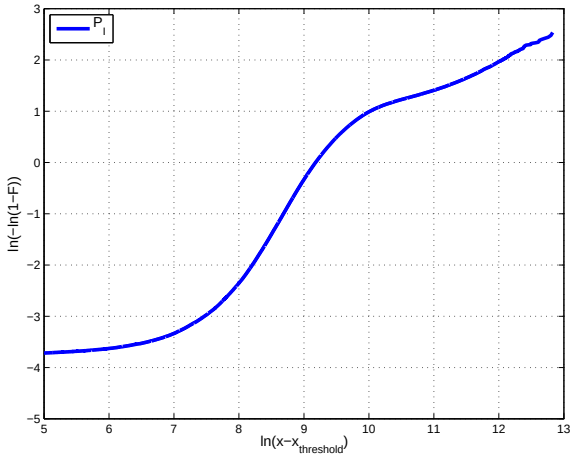

(b) P_I

Figure 7.12: 750 Hour Composite Monte Carlo Simulation of Relative Motion (RM) and Impact Pressure in Weibull Space [Sea State 7, 15 knots, Head Seas; $x_{\text{threshold}} = 0$]

mined. In this figure, the extreme relative motion from MCS is slightly lower than the most likely value (the inflection point of the CDF) of the distribution, which is very possible. But the extreme impact pressure from MCS is higher than the most likely value of the distribution, which is in accordance with the expectation explained above. A comparison of Fig. 7.7(b) with Fig. 7.12(b) strongly suggests that the prediction with this level of accuracy would not be possible with the typical Weibull extrapolation.

Although Fig. 7.11 suggests that the DLG results are consistent with the scatter

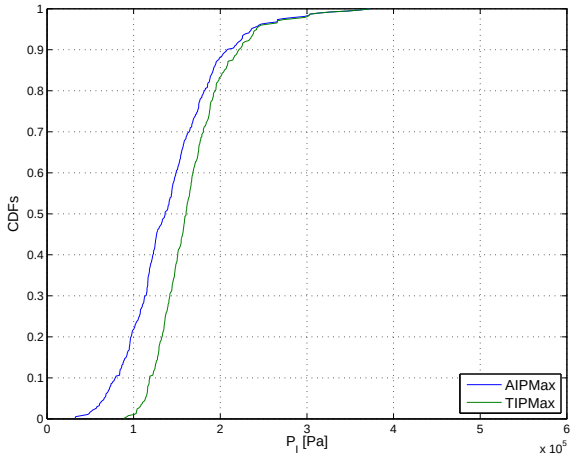

(a) Exposure Time: 2 Hours

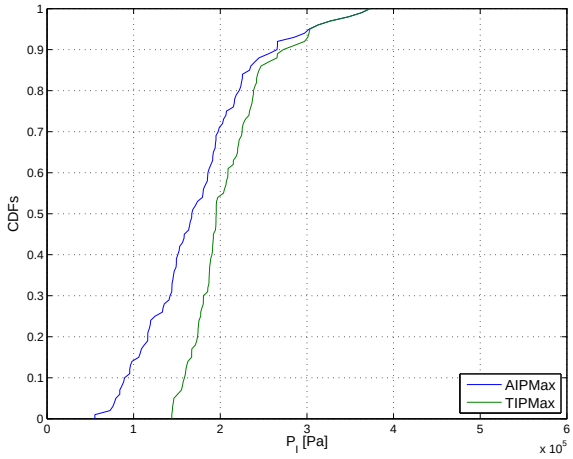

(b) Exposure Time: 7.5 Hours

Figure 7.13: Comparison between Extreme Value Distribution of Associated Impact Pressure Maxima (AIPMax) and "True" Impact Pressure Maxima (TIP-Max) from Monte Carlo Simulation [Sea State 7, 15 knots, Head Seas]

diagram created from the Monte Carlo simulation, this is not enough to completely validate the DLG approach. Extending the record length is not a feasible option. Similar to the 5σ case discussed in Chapter VI, it would require 750,000 hours' worth of LAMP2 Monte Carlo simulation to process the 1000 realizations of the 4.99σ event, which clearly exceeds the scope of the current research. However, the CDF of 7.5 hours may be approximately calculated from the 750 hour Monte Carlo simulation, based on which the 1000 realizations of the 3.96σ event may be validated.

While the results will be presented in the next section, it is possible to predict the

comparison between them. Specifically, the scatter diagrams in Fig 7.10 is processed in the form of two CDFs, as shown in Fig. 7.13. Due to the difference in the number of samples and its stochastic nature, the CDF from DLG will not be identical to AIPMax. However, the CDF of the impact pressure from the 3.96σ DLG event should be comparable to the CDF of AIPMax in Fig. 7.13(b). On the other hand, the comparison between the CDF of the relative motion from DLG and the CDF of the relative motion from MCS is expected to be almost perfect, as suggested by Fig. 7.9(a).

7.4 Validation of DLG

Similar to Sec. 6.6, the question to be addressed in this section is whether the distribution of the nonlinear bow impact pressures collected from the 1000 DLG+LAMP realizations is statistically comparable to the distribution of the Monte Carlo simulations with the corresponding exposure time. As mentioned, the 750 hour composite Monte Carlo simulation is divided into 100 segments, such that each segment represent approximately 7.5 hours' worth Monte Carlo simulation. The maximum in each segment is collected to obtain the empirical CDF of extreme relative motion and impact pressure in 7.5 hours. The exposure time of 7.5 hours is comparable to the TEV of 3.96 according to the mean period and the broadness parameter of the response spectrum of this case. The extreme relative motions and the impact pressures for each DLG+LAMP realization are processed to obtain the CDFs of the extreme relative motion and the extreme impact pressure. The results of this process are presented in Fig. 7.14.

In summary, the results are as expected in the closing of the previous section. First of all, in Fig. 7.14(a), the DLG+LAMP successfully finds the CDF of the extreme relative motion at the target point. Since the number of samples associated with MCS is significantly lower than that of DLG+LAMP, however, the CDF of MCS is not as smooth as the CDF of DLG+LAMP. The comparison of two impact pressure CDFs in Fig. 7.14(b) also meets the expectation discussed in the previous section. The two CDFs shows a rather significant deviation at the lower tail, which was expected. As PNE increases, however, the matching between them improves. As can be seen, there is still a small deviation in the upper tail. Considering the highly nonlinear nature of the problem, the statistical nature of the results, and the difference in the number of samples used in the construction of two CDFs, the comparison is very good. The difference in the number of samples is important, because the maximum

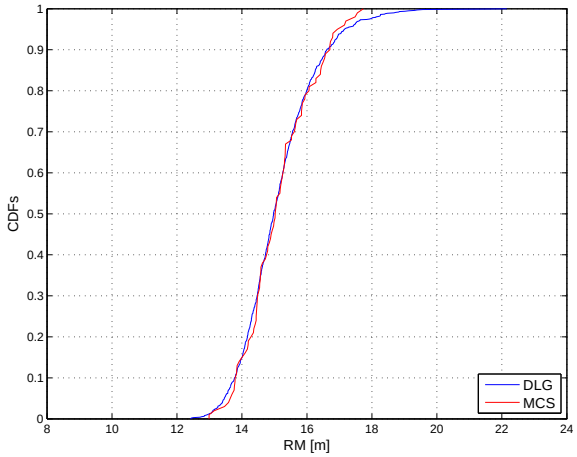

(a) Relative Motion

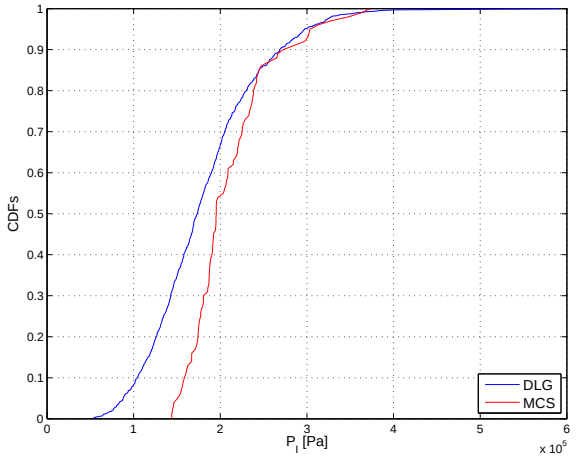

(b) P_I

Figure 7.14: Comparison between Extreme Value Distribution from DLG and from Monte Carlo Simulations (MCS) for 7.5 Hours [Sea State 7, 15 knots, Head Seas]

value achievable from the empirical CDF is simply the maximum of the observed samples. While the results presented so far show that the DLG process is working as expected for the extreme bow slamming pressure estimation, the comparison between two CDFs may be further improved by designing a more accurate "clock",

If the magnitude of the slamming pressure is highly dependent on the relative velocity as assumed, for example, in Ochi & Motter (1973), an "artificial" process that combines the extreme positive relative motion and the extreme negative relative motion may be a better choice to bound the impact pressure P_I. Consider the

dimensionless mean-removed relative motion $r(t)$ expressed by uniformly distributed random phase angles γ_j between $-\pi$ and π:

$$r(t) = \sum_{j=1}^{N} b_j \cos(-\omega_{e_j} t + \gamma_j) \tag{7.2}$$

where b_j is the Fourier coefficients normalized by the standard deviation of the process, such that the variance of the process becomes unity. Given the set of phase angles γ_j, the non-dimensional relative velocity at the same target point can be deterministically calculated as

$$\dot{r}(t) = \sum_{j=1}^{N} c_j \sin(-\omega_{e_j} t + \gamma_j) \tag{7.3}$$

where c_j is $\omega_{e_j} b_j$ normalized again such that the variance of $\dot{r}(t)$ becomes unity.

Since the relative velocity at the instance of slam is important, the extreme impact pressures may be correlated to the maxima of a derived process $x(t)$ defined by the normalized relative motion at t minus the normalized relative velocity at $t + t_o$ as shown in Eq. (7.4).

$$\begin{aligned} x(t) &= r(t) - \dot{r}(t + t_o) \\ &= \sum_{j=1}^{N} b_j \cos(-\omega_{e_j} t + \gamma_j) - \sum_{j=1}^{N} c_j \sin(-\omega_{e_j}(t + t_o) + \gamma_j) \\ &= \sum_{j=1}^{N} b_j \cos(-\omega_{e_j} t + \gamma_j) + \sum_{j=1}^{N} c_j \cos(-\omega_{e_j} t + \gamma_j - \omega_{e_j} t_o + \pi/2) \end{aligned} \tag{7.4}$$

where t_o accounts for the time it takes to the hull submergence after the peaks of the relative motion time history at the target point, and the phase angle γ_j is uniformly distributed between $-\pi$ and π. The maximum of this derived process $x(t)$ in a given exposure time may be better correlated with the extreme impact pressure in the same exposure time.

Two random variables sampled from $r(t)$ and $\dot{r}(t)$ are uncorrelated, so they approach two independent Gaussian random variables as N goes to infinity. The summation of two independent random Gaussian random variables follows a Gaussian distribution. Thus, the DLG process can readily be applied. Due to the time shift t_o, however, two random variables (D and V) sampled from $r(t)$ and $-\dot{r}(t + t_o)$ are correlated, and they approach a bivariate Gaussian distribution as N goes to infinity (see e.g., Newland, 2005). Even in this case, the random variable $D + V$ follows a

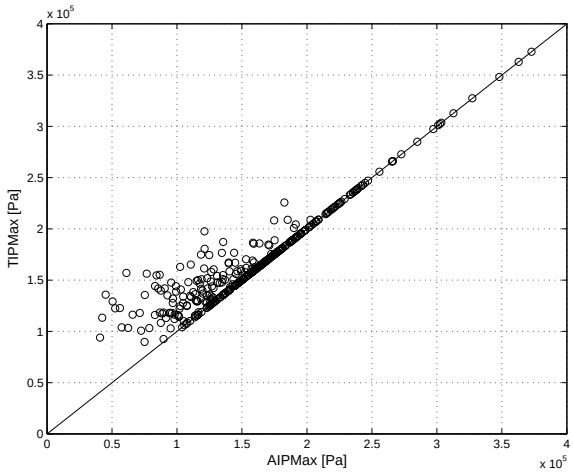

(a) Exposure Time: 2 Hours; $\rho_{XY} = 0.9411$

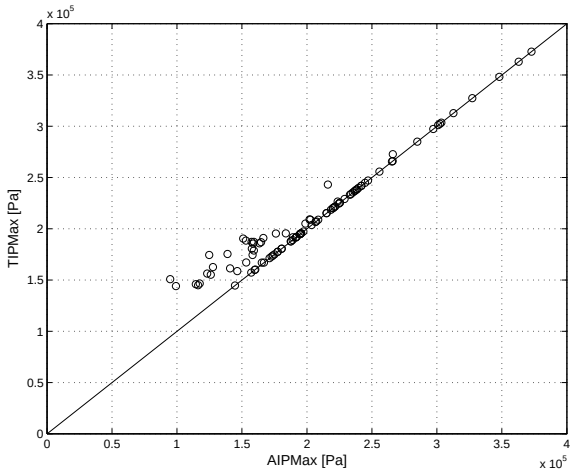

(b) Exposure Time: 7.5 Hours; $\rho_{XY} = 0.9754$

Figure 7.15: Correlations between Impact Pressure Associated with Derived Process (AIPMax) and "True" Impact Pressure (TIPMax) [Sea State 7, 15 knots, Head Seas]

Gaussian distribution (see e.g., Feller, 1965). The mean of the random variable is still zero, but the variance includes the effect of the non-zero covariance as

$$\sigma_{D+V}^2 = \sigma_D^2 + \sigma_V^2 + 2\mathrm{Cov}[D, V] \tag{7.5}$$

Meanwhile, Eq. (7.4) can be combined into the form of Eq. (2.1) using the trigono-

metric identities.

$$x(t) = \sum_{j=1}^{N} a_j \cos(-\omega_{e_j} t + \epsilon_j) \tag{7.6}$$

where

$$a_j^2 = (b_j)^2 + (c_j)^2 + 2b_j c_j \cos(\omega_{e_j} t_o - \pi/2) \tag{7.7}$$

and

$$\begin{aligned} \epsilon_j &= \arctan\Big(\frac{b_j \sin(\gamma_j) + c_j \sin(\gamma_j - \omega_{e_j} t_o + \pi/2)}{b_j \cos(\gamma_j) + c_j \cos(\gamma_j - \omega_{e_j} t_o + \pi/2)}\Big) \\ &= \arctan\Big(\frac{b_j \sin(\gamma_j) + c_j \cos(\gamma_j - \omega_{e_j} t_o)}{b_j \cos(\gamma_j) - c_j \sin(\gamma_j - \omega_{e_j} t_o)}\Big) \end{aligned} \tag{7.8}$$

Therefore, the Fourier coefficients of this derived process can be calculated from the Fourier coefficients of the relative motion, or it can be directly computed from a series of time domain analysis under regular wave inputs. When the DLG process generates an ensemble of ϵ_j, the back-calculation of the associated γ_j using Eq. (7.8) is straightforward.

In order to show that this process may bound the extreme of P_I better than the pure relative motion, the scatter diagrams are constructed in Fig. 7.15. The time shift t_o is assumed to be 1.4 seconds, based on the mean period and the mean value of the relative motion at the target point. Not only are the correlation coefficients significantly higher compared to those in Fig. 7.6, it is apparent that the extreme AIPMax can significantly better bound the extreme TIPMax. In other words, the impact pressure associated with the distribution of extreme responses of this derived process found from the DLG model better bounds the CDF of the highly nonlinear P_I than the relative motion.

Fig. 7.16 displays the result of a DLG analysis of the derived process $x(t)$. The TEV value associated with the exposure time of 7.5 hours is estimated approximately as 3.97, based on the response spectrum of the process. The extreme impact pressures associated with the 1000 realization of the 3.97σ of $x(t)$ are collected and then processed as a CDF, which is shown as CDF(RM-RV). Presented simultaneously is the CDF of the maximum impact pressures in the 100 segments of the 7.5 hour Monte Carlo simulations (MCS). The CDF of the 1000 realizations of the 3.96σ introduced in Fig. 7.14(b) is referred as DLG(RM). As predicted by Fig. 7.15, DLG(RM-RV) is a better clock to bound the impact pressure of the target point, at least for the current environmental condition. A small deviation between DLG(RM) and DLG(RM-RV) in the upper tail may come from the uncertainty in the estimation of TEVs based on

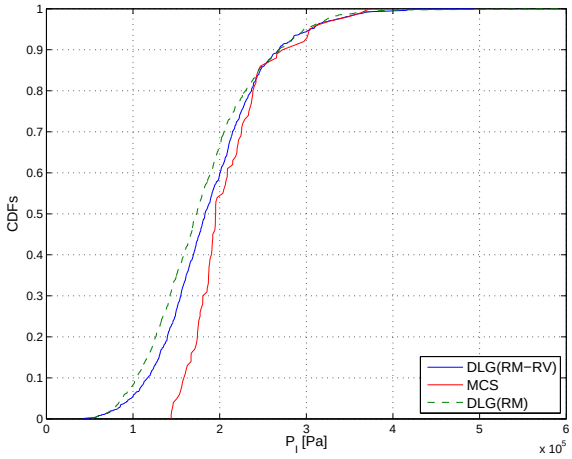

Figure 7.16: Comparison between Extreme Value Distribution from DLG of Derived Process x(t) and from Monte Carlo Simulations (MCS) for 7.5 Hours [Sea State 7, 15 knots, Head Seas]

two different response spectra.

It is possible to improve the matching even further by introducing a weight factor w in front of $\dot{r}(t)$ in Eq. 7.4. For example, Fig. 7.17 displays a slightly improved DLG(RM-RV) compared to Fig. 7.16. The weight factor w is set to be approximately 1.32. This weight factor is obtained from the 750 hour Monte Carlo simulation and found to yield slightly higher correlation coefficients (0.9712 for 2 hours and 0.9765 for 7.5 hours) than those in Fig. 7.15, which is consistent with the DLG results.

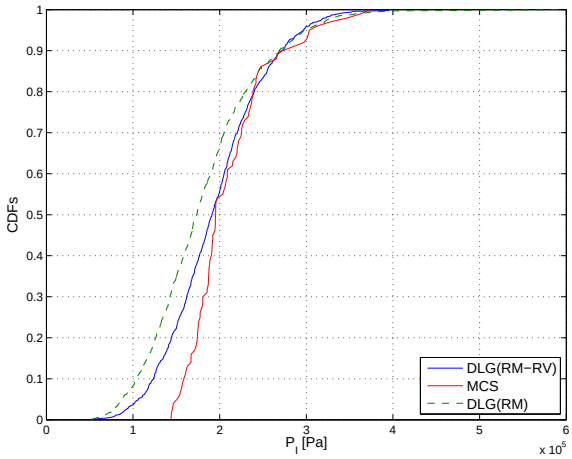

Figure 7.17: Comparison between Extreme Value Distribution from DLG of Derived Process x(t) with Weight Factor w and from Monte Carlo Simulations (MCS) for 7.5 Hours [Sea State 7, 15 knots, Head Seas]

The prediction of extreme impact pressure based on the derived process $x(t)$ not only validate the DLG approach again, but also suggest that the applicability of the current DLG approach can be significantly broadened if a suitable process can be devised, based on an understanding of the physics of the problem. For example, the combination of stresses at different points of a hull can be addressed using this approach.

CHAPTER VIII

Conclusions

8.1 Summary

The rule-based design approach has long been validated and found to be extremely useful for conventional ship design. Despite a successful history, the classification societies are continuously updating their rules to incorporate new developments such as state-of-the-art time domain computational tools. The computer-based direct analysis using these computational tools is essential to the design process for novel ships and/or offshore units. This is because the class rules are largely based on simplified empirical formulas that work within limits and thus they sometimes fail to capture the complex physics observed in nature.

Due to the developments in computer science and marine hydrodynamics, high-fidelity hydrodynamic computation is indeed becoming more popular and feasible. However, these high-fidelity computation softwares usually run much slower than real-time, which prevents a thorough investigation of the design space, especially during the concept design stage. This may negatively affect structural design and its optimization.

To address this limitation, a new probabilistic model/process, Design Loads Generator (DLG), has been developed and presented in this dissertation. As demonstrated, the process determines an ensemble of critical wave episodes associated with an input exposure time for different types of responses. Specifically, it can successfully replace the estimation of the long-term extreme value distribution based on various extrapolation techniques. With the application of DLG, the shortcomings associated with the statistical extrapolation can be minimized. Consequently, the process has a strong potential to supplement or even replace the current practice of determining critical wave episodes central to the computer-based direct analysis.

The utility of the DLG analysis method is that the interaction between the incident wave and the dynamic vessel response (both wave-induced and whipping-induced bending) occurs naturally, within the limits of the modeling assumptions of the simulator. The total duration of a DLG realization can be reduced to several minutes around an extreme for a specified exposure time, suggesting that even fully nonlinear hydrodynamic computation systems can begin to be used far more routinely in support of a ship design. The reduced simulation times required to accurately identify lifetime maximum loads will be especially useful during the concept design stage of a novel ship and marine system. Despite these advantages, the increased number of realizations (e.g., $500 \sim 1000$ as used in this dissertation) compared to a typical approach utilizing a single regular wave train may be viewed as a challenge. However, it is the cost to be spent to address the problem more accurately. This challenge will be solved naturally, as the multi-core CPU technology develops further, because the realizations can be simulated in parallel.

Unlike other methods found in the literature, this process contains all of the following features:

- The process can find an ensemble of critical wave episodes, not just a single wave realization that will produce a predetermined response.
- Each wave episode determined by the DLG process represents an irregular seaway around the extreme events for a given input exposure time, which is an important component of risk-based design analysis.
- The process is practically not influenced by the number of wave components (N) or the exposure time (TEV).
- The process is sufficiently fast and robust to readily be used in the real design process. Partially due to its speed and robustness, the process can be expanded to the extreme response under the short-crested seaways.

Compared to Alford (2008), the predecessor of the current research, the distribution generated by the current DLG now exactly matches the theoretical extreme value distribution. Moreover, since the time-consuming multivariable nonlinear optimization is no longer required, the total computation time to find the phase angles associated with the exact theoretical extreme value distribution is only a fraction of what Alford (2008) had to spend. Furthermore, the number of Fourier components N can now be increased to several thousands without being affected by the cost of the

multivariable nonlinear optimization. Last but not least, the DLG model can handle the response of a system under bi-directional seaways or even short-crested seaways. For example, as mentioned in Chapter IV, the bi-directional seaways composed of waves coming from two different directions may be important in the springing analysis of a vessel as discussed in Vidic-Perunovic (2005) or offshore units such as FPSO as explained in ABS (2010).

8.2 Contributions of Current Research

The extreme value distribution, which is the core of the current DLG model, is still a basis for the prediction of long-term wave statistics. For example, the probable maximum value in Ochi (1978), frequently referred to in class rules, is simply the modal value of the extreme value distribution. This value corresponds to a PNE of 1-e^{-1}, which may not be sufficient; thus, a safety factor is often added to find the design extreme value. Although very useful, these values are just numbers, and no information regarding the physics behinds the extreme events can be found unless the realistic time series associated with the extreme event can be obtained. This, in fact, is the motivation of the Dynamic Loading Approach (DLA), an optional classification notation available from American Bureau of Shipping as explained in e.g., ABS (2006).

Unlike the DLA analysis, where an equivalent regular incident wave history is produced, the DLG model generates an ensemble of irregular time histories associated with the distribution of extreme responses for the given input exposure time. However, DLA and DLG share common attributes. Most notably, they are both geared to the utilization of high-fidelity nonlinear seakeeping and structural codes. Since DLG does not require designers to change any previous tools and practices, the current DLG model can readily be combined into the current practice of designing ships and offshore units. In fact, the DLG approach facilitates the efficient use of high-fidelity hydrodynamic computational softwares available to them during the design process and strengthens the philosophy already in place.

Presented in Chapter III is the discovery that the change in the extreme value distribution as the exposure time (i.e., TEV) increases can be described as a single parameter (i.e., $\boldsymbol{\lambda}_o$). Due to this discovery and a novel approach devised to find $g_Y(y)$, the optimization problem now becomes much simpler than that of Alford (2008). The expansion or generalization of the DLG model introduced in Chapter IV is another important contribution. As mentioned, this can potentially facilitate the

use of DLG in the field of offshore engineering. In addition, as demonstrated in Sec. 4.3, the DLG process can provide statistically meaningful initial conditions for more rigorous nonlinear wave-field simulations as shown in e.g., Wu (2004). While the generalization of the DLG model can handle the summation of multiple independent random processes, the derivation of a completely new process is also possible as formulated in Sec. 7.4 or as used in Kim & Troesch (2011). This strategy will allow DLG to address a wider range of problems better than earlier methods.

The dissertation is first to use the acceptance-rejection method in the field of naval architecture and marine/ocean engineering, to the best of author's knowledge. This algorithm is a very powerful scheme and it can possibly be extended to other problems in our fields. For example, the theoretical extreme value distribution, which was used as a target PDF may be adjusted to address a slightly non-Gaussian process with a suitable model.

Last but not least, the dissertation employs the strategy of estimating the extreme value distribution of highly nonlinear processes based on the extreme value distribution of an associated linear process of the same exposure time. Unlike some of the previously available methods introduced in Chapter I, the dissertation demonstrated that this strategy can bound the distribution of extreme responses of highly nonlinear processes, which is also an important contribution of this research.

8.3 Future Research

Unfortunately, the world is not so simple to be completely described by linear systems. The dynamical systems found in a real world problem are rarely linear. They are most frequently located on a scale between slightly nonlinear and fully nonlinear. Although the strategy adopted by the current dissertation to address nonlinear processes works well and provides much more information about the nonlinear processes, such as whipping bending moments and impact pressures, than previously available, the next natural step would be to find a way to directly pinpoint the extreme responses of nonlinear systems. Similarly, since the DLG process can now perfectly address the extreme response under the assumption of the Gaussian wave model using the probabilistic model developed in the current dissertation, the natural next step would be to develop a version of DLG that can address non-Gaussian wave inputs. The use of the second-order wave model based on the phases for linear waves would be an obvious step. But it might be possible to directly include the effects of higher order wave model into the governing equation of DLG.

The other potential direction the DLG model can follow is the addition of a new capability of investigating of different types of extreme events. Each DLG realization captures a single extreme event in a given exposure time. The wave trains outside the very extreme event may look relatively benign as shown in Fig. 4.7. As mentioned, this phenomenon is not inconsistent with extreme wave examples observed from actual radar sets as shown in e.g., Lehner (2004). However, a series of big waves (e.g., the phenomena called *three sisters*) may induce a more critical condition of interest to designers. This problem is expected to be addressed by the approach introduced with Eq. (7.4). Similarly, since the second largest or third largest linear extreme response in a given exposure time might be better correlated with the true nonlinear extreme response (Torhaug, 1996), the ability to handle the k^{th} extreme value will be a useful addition to the current DLG formulation.

This dissertation shows that the DLG process can be used for highly nonlinear whipping bending moments and impact pressures, thus validating the DLG process to a degree. However, without a doubt, further validation efforts need to be made using a wide range of problems and much longer Monte Carlo simulations than used in this research. For example, the probability of experiencing *green water on deck* can be addressed in the concept design stage using the DLG approach. The estimation of the extreme wetdeck slamming of multi-hull vessels and offshore floating units will be possible, using the very approach applied to predict the extreme bow impact pressures in Chapter VII.

APPENDICES

APPENDIX A

Effects of N

As explained in Chapter II, the derivation of DLG model starts from a process defined by Eq. (A.1).

$$x(t) = \sum_{j=1}^{N} a_j \cos(\omega_j t + \epsilon_j) \tag{A.1}$$

Assuming the process is stationary and ergodic, the random variable X from this process is sampled from an *ensemble space* at $t = 0$ defined by Eq. (A.2).

$$x(0) = \sum_{j=1}^{N} a_j Y_j \tag{A.2}$$

where

$$Y_j = \cos(\epsilon_j) \tag{A.3}$$

where ϵ_j is uniformly distributed between $-\pi$ and π.

The random variable X sampled by Eq. (A.2) is determined by the choice of ϵ_j: ϵ_j may be sampled from a uniformly distributed random variable between $-\pi$ and π such that X models a Gaussian random variable. When N goes to infinity, the PDF of X approaches the Gaussian PDF, which is due to the central limit theorem. Even when N is finite, the difference between the Gaussian PDF and the PDF of X may be quite small.

However, the difference between the extreme value distribution of the Gaussian random variable and the random variable X can be significant due to the nature of Eq. (2.13). The deviation can be calculated, without any random sampling of ϵ_j, using the Fast Fourier Transform. In other words, the PDF of the extreme values in m

samples of X can be calculated from the inverse Fourier transform of the characteristic function of the random variable as derived below:

The CDF of the uniformly distributed (between $-\pi$ and π) random phases ϵ_j can be defined as

$$F_{E_j}(z) = \frac{z}{2\pi} + \frac{1}{2}, \quad -\pi \leq z < \pi \tag{A.4}$$

Therefore, the characteristic function of its component Y_j, when the CDF of ϵ_j follows Eq. (A.4), is then calculated as

$$\begin{aligned} F_{Y_j}(y) &= P(\cos\epsilon_j \leq y) \\ &= P(\epsilon_j \geq \arccos y) \\ &= 2 - 2F_{E_j}(\arccos y) \\ &= 1 - \arccos y/\pi, \quad -1 \leq y \leq 1 \end{aligned} \tag{A.5}$$

where Eq. (A.4) is used in the last equality. Due to its definition, Y_j is a random variable distributed between -1 and 1. Differentiating Eq. (A.5) with respect to y produces the PDF of Y_j, which is

$$f_{Y_j}(y) = \frac{1}{\pi\sqrt{1-y^2}}, \quad -1 \leq y \leq 1 \tag{A.6}$$

Additionally, when a random variable is expressed as a summation of N statistically independent random variables, the characteristic function of the random variable can be expressed using the characteristic functions of N independent random variables:

$$\begin{aligned} E[\mathrm{e}^{isX}] &= E[\mathrm{e}^{is(a_1Y_1+a_2Y_2+\cdots+a_NY_N)}] \\ &= E[\mathrm{e}^{isa_1Y_1}\ \mathrm{e}^{isa_2Y_2}\cdots\ \mathrm{e}^{isa_NY_N}] \\ &= E[\mathrm{e}^{isa_1Y_1}]E[\mathrm{e}^{isa_2Y_2}]\cdots E[\mathrm{e}^{isa_NY_N}] \end{aligned} \tag{A.7}$$

where the last equality is from the independency. Due to this identity, the characteristic function of X can now be determined from the product of the characteristic functions of Y_j, which is

$$\begin{aligned}\psi_X(s) &= \prod_{j=1}^{N} \int_{-\infty}^{\infty} \mathrm{e}^{isa_j y} f_{Y_j}(y)\,\mathrm{d}y \\ &= \prod_{j=1}^{N} \int_{-1}^{1} \mathrm{e}^{isa_j y} \frac{1}{\pi\sqrt{1-y^2}}\,\mathrm{d}y \\ &= \prod_{j=1}^{N} J_o(a_j s) \end{aligned} \tag{A.8}$$

where the second equality is due to Eq. (A.6) and the last equality is from the use of Eqs. (3.9) $\sim$ (3.10). Taking the inverse Fourier Transform of Eq. (A.8) generates the PDF of X, which should be very close to the theoretical Gaussian distribution for larger N. Due to the characteristic of Eq. (2.13), however, a small deviation can make quite a big difference in the distribution of X_m.

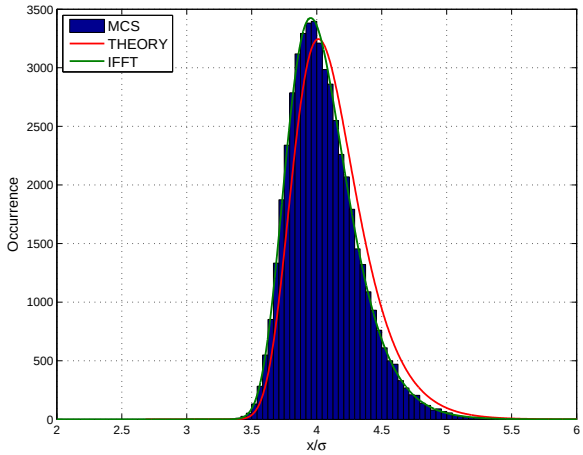

Figure A.1: Example Comparison between Empirical Extreme Value Distribution from Monte Carlo Simulations (MCS), Theoretical Extreme Value Distribution (THEORY), and Inversion of Characteristic Function (IFFT)

The next step is to apply Eq. (2.13) to X from the inversion of Eq. (A.8) to get the PDF of X_m or the extreme value distribution of X. An example is shown in Fig. A.1. Similar to Fig. 3.5(a), Monte Carlo simulations (MCS) using the approach explained in Sec. 2.2 approximates the theoretical extreme value distribution of a process (THEORY) reasonably well, but a small discrepancy between MCS and THEORY still exists due to the finite N. However, the inverse Fourier transform of

Eq. (A.8) (IFFT) can find MCS without time-consuming Monte Carlo simulations. Moreover, IFFT matches MCS better than THEORY. In fact, DLG calculates $g_Y(y)$, as explained in Sec. 3.5, using IFFT in a very similar way: the only difference is the use of the modified Gaussian distribution instead of the uniform distribution for the phase angles.

In DLG, the extreme value distribution of the theoretical Gaussian random variable is used as the target extreme value distribution. Utilizing the extreme value distribution calculated from the inversion of Eq. (A.8) as a target extreme value distribution is an available option in DLG. However, in most cases, the difference is not expected to be significant, as long as N is not too low. The DLG program generates an warning message, if N is too low, considering the input spectrum. For an additional discussion of the effect of N on the finite approximation of a Gaussian process, refer to Hodapp *et al.* (2012).

APPENDIX B

Derivation of Governing Equation

As shown in Sec. 2.4, the cornerstone of DLG is to recover X_m using the the characteristic function of X'_m, where the modified Gaussian distribution with different parameters is used to generate a set of phase angles. In other words, the phase distribution associated with X'_m is modeled by the modified Gaussian distribution. The PDF of the modified Gaussian distribution can be calculated from the integration of Eq. (2.26), which is

$$F_{E_j}(z) = \frac{1}{2}\text{erf}(\frac{z}{\lambda_j\sqrt{2}}) + \frac{1}{2\pi}\big(1 - \text{erf}(\frac{\pi}{\lambda_j\sqrt{2}})\big)(z+\pi) + \frac{1}{2}\text{erf}(\frac{\pi}{\lambda_j\sqrt{2}}) \tag{B.1}$$

Similar to the approach introduced in Appendix A, when ϵ_j follows the modified Gaussian distribution, the CDF of Y_j defined by Eq. (A.3) becomes

$$\begin{aligned} F_{Y_j}(y) &= P(\cos\epsilon_j \le y) \\ &= 2 - 2F_{E_j}(\arccos y) \\ &= 1 - \text{erf}(\frac{\arccos y}{\lambda_j\sqrt{2}}) + \frac{\arccos y}{\pi}\Big(\text{erf}(\frac{\pi}{\lambda_j\sqrt{2}}) - 1\Big), \quad -1 \le y \le 1 \end{aligned} \tag{B.2}$$

Taking the derivative of Eq. (B.2) with respect to y yields the PDF of Y_j when ϵ_j follows the modified Gaussian distribution with a parameter λ_j.

$$f_{Y_j}(y) = \frac{\sqrt{2\pi}\ \text{e}^{-(\arccos y)^2/(2\lambda_j^2)} - \lambda_j\ \text{erf}\left(\pi/(\lambda_j\sqrt{2})\right) + \lambda_j}{\pi\lambda_j\sqrt{1-y^2}}, \quad -1 \le y \le 1 \tag{B.3}$$

By substituting Eq. (B.3) into Eq. (A.7), the characteristic function of X'_m can be

obtained as

$$\psi_{X'_m}(s) = \prod_{j=1}^{N} \int_{-1}^{1} \frac{\mathrm{e}^{ia_j sy}}{\pi\lambda_j\sqrt{1-y^2}} \Big\{ \sqrt{2\pi}\ \mathrm{e}^{-(\arccos y)^2/(2\lambda_j^2)} - \lambda_j\ \mathrm{erf}\left(\pi/(\lambda_j\sqrt{2})\right) + \lambda_j \Big\}\, \mathrm{d}y \tag{B.4}$$

This equation can very easily be extended to the characteristic function of X'_m under short-crested seaways. According to Eq. (4.9), the response of a system at $t = 0$ can be expressed as

$$x(0) = \sum_{k=1}^{h} \sum_{j=1}^{N} {}^{k}a_j \cos({}^{k}\omega_j \cdot 0 + {}^{k}\epsilon_j) = \sum_{k=1}^{h} \sum_{j=1}^{N} {}^{k}a_j Y_{jk} \tag{B.5}$$

where ${}^{k}\epsilon_j$ is uniformly distributed between $-\pi$ and π, and Y_{jk} is simply defined as

$$Y_{jk} = \cos({}^{k}\epsilon_j) \tag{B.6}$$

Since the statistical independency of Y_{jk} remains valid, using Eq. (A.7), Eq. (B.4) can readily be extended to derive the characteristic function of X'_m under the short-crested seaways:

$$\psi_{X'_m}(s) = \prod_{k=1}^{h} \prod_{j=1}^{N} \int_{-1}^{1} \frac{\mathrm{e}^{i({}^{k}a_j)sy}}{\pi({}^{k}\lambda_j)\sqrt{1-y^2}} \Big\{ \sqrt{2\pi}\ \mathrm{e}^{-0.5\arccos^2 y/{}^{k}\lambda_j^2} - \lambda_j\ \mathrm{erf}\left(\pi/({}^{k}\lambda_j\sqrt{2})\right) + {}^{k}\lambda_j \Big\}\, \mathrm{d}y \tag{B.7}$$

APPENDIX C

Rankine Source Formulation in LAMP

Although the DLG process does not dictate any specific nonlinear simulation program, LAMP has been significantly used in this research. LAMP has been introduced, verified, and validated quite extensively (e.g., Shin *et al.*, 2003; Lin *et al.*, 2007). However, it is not a commercially available program. Therefore, a background of LAMP, available in the manual of LAMP (Lin *et al.*, 2008), is taken and summarized in this appendix.

LAMP is a 3D time domain potential code and it solves the combined effect of the diffraction problem and the radiation problem using a choice of singularity models and computational approaches. Several singularity models are available to solve the problem at each time step. Originally, LAMP was developed to use the transient Green function to solve the boundary value problem. With this approach, singularities need to be distributed only on the wetted body surface, which can save the computational cost. However, numerical difficulties arises near the free surface for ship with non-wall-sided geometry or on the area where the intersection angles between the the body surface and the free surface become small. To address this problem, the mixed source formulation (i.e., the combination of the transient Green function approach and the Rankine source approach) has been added, which is the current principal singularity model. However, the mixed source formulation also has a problem when the Froude number is high: obtaining a stable free surface solution may become a challenge. For this reason, the Rankine source method with a damping beach is recommended for a problem with a high Froude number.

Since the Rankine source does not automatically satisfy the free surface boundary condition, the singularity should be placed on the free surface, too. However, it has to be truncated at a certain limit due to the high computational cost. Instead,

the so-called numerical damping beach is placed around the outer boundary of the truncated free surface. The effect of the singularity on the far field surface S_∞ to the body surface or the free surface is assumed zero. Even though LAMP has a capability of addressing the shallow water effects, all the LAMP simulations introduced in this dissertation assume infinite water depth.

In LAMP, the exact body boundary condition can be applied on the instantaneous body surface, but a linearized free surface boundary condition is used even with LAMP4. In order to make it possible, the hull geometry is deformed such that the free surface on the body becomes flat in a computational domain at each time step.

The boundary value problem LAMP solves is also taken from the LAMP manual (Lin *et al.*, 2008) and summarized. First, the total velocity potential is decomposed as the summation of the incident wave potential and the perturbation potential

$$\Phi_T(\vec{x},t) = \Phi_I(\vec{x},t) + \Phi_P(\vec{x},t) \tag{C.1}$$

where $\vec{x}$ is the position vector in a space-fixed coordinate system. Since the incident wave potential by definition satisfies the Laplace equation, the governing equation in this approach becomes

$$\nabla^2\Phi_P = 0 \quad \text{in} \quad \Omega \tag{C.2}$$

The body boundary condition is then applied on the instantaneous submerged hull surface S_b. Therefore, the no-flux boundary condition on the body is expressed as

$$\frac{\partial\Phi_P}{\partial n} = \vec{V}\cdot\hat{n} - \frac{\partial\Phi_I}{\partial n} \quad \text{on} \quad S_b \tag{C.3}$$

where $\vec{V}$ is the instantaneous velocity of a point on the body including rotational effects. $\hat{n}$ is the normal vector on the body surface and it is positive into the body. This boundary condition ensures that the perturbation potential includes the diffraction potential.

With regard to the free surface boundary condition, the linearized dynamic free surface boundary condition is applied on the mean free surface S_f.

$$\frac{\partial\Phi_P}{\partial t} = -g\zeta \quad \text{on} \quad S_f \tag{C.4}$$

where ζ is termed as *the total disturbance wave elevation* on S_f.

The kinematic free surface boundary condition is a little different due to the numerical damping beach applied to absorb the outgoing wave energy generated by

the body.

$$\frac{\partial \zeta}{\partial t} = \begin{cases} \dfrac{\partial \Phi_P}{\partial \zeta} & \text{on} \quad S_{f1} \quad (\text{for} \quad |\vec{x}| < r_o) \\ \dfrac{\partial \Phi_P}{\partial \zeta} - \mu_1(\vec{x})\zeta + \dfrac{\mu_1^2(\vec{x})}{4g}\Phi_P & \text{on} \quad S_{f2} \quad (\text{for} \quad |\vec{x}| > r_o) \end{cases} \tag{C.5}$$

where $S_{f1} \cap S_{f2} = S_f$ and S_{f2} is the damping beach region (outer area of the free surface). The coefficient μ_1 is the damping beach parameter, which is defined as

$$\mu_1 = 3\mu_0 \frac{(|\vec{x}| - r_o)^2}{(L - r_o)^3} \tag{C.6}$$

where r_o and L define the inner and the outer edge of the damping beach and μ_o is called the beach strength. r_o, L and μ_o are parameters that can be changed in the input control file.

The free surface boundary condition needs to be integrated in time to update ζ and Φ_T at the next time step. Due to the space fixed coordinate, the free surface boundary condition is rewritten as

$$\frac{D\zeta}{Dt} = \begin{cases} \dfrac{\partial \Phi_P}{\partial \zeta} + \vec{U} \cdot \nabla \zeta & \text{on} \quad S_{f1} \\ \dfrac{\partial \Phi_P}{\partial \zeta} - \mu_1(\vec{x})\zeta + \dfrac{\mu_1^2(\vec{x})}{4g} + \vec{U} \cdot \nabla \zeta \Phi_P & \text{on} \quad S_{f2} \end{cases} \tag{C.7}$$

and

$$\frac{D\Phi_P}{Dt} = -g\zeta + \vec{U} \cdot \nabla \Phi_P \quad \text{on} \quad S_f \tag{C.8}$$

where $\vec{U}$ is the grid velocity of the free surface and D/Dt is the material derivative following a moving control point. The initial conditions for the time integration are

$$\Phi_P = \frac{\partial \Phi_P}{\partial t} = 0 \quad \text{at} \quad t = 0 \tag{C.9}$$

The boundary integral equation corresponding to the ranking source singularity $G = 1/r = 1/|P - Q|$ is

$$2\pi\Phi_P(P) + \int_{S_b + S_f} \Big(\Phi_P \frac{\partial G}{\partial n} - \frac{\partial \Phi_P}{\partial n} G \Big) dS = 0 \tag{C.10}$$

where P is the field point, Q is the source point. This equation is solved using the boundary element method at each time step.

Once the total disturbance potential Φ_P is obtained, the total hydrodynamic pressure can be calculated on S_b using the Bernoulli equation.

$$p = -\rho\big(\frac{\partial \Phi_T}{\partial t} + \frac{1}{2}|\nabla \Phi_T|^2\big) \tag{C.11}$$

The associated forces and moments can be calculated by the integration of the pressure over the instantaneous body surface at each time step and the resulting forces and moments can finally be used to solve the equation of the motion at each time step.

$$\vec{F} = \int_{S_b} p\hat{n}dS \quad \text{and} \quad \vec{M} = \int_{S_b} p\vec{r} \times \hat{n}dS \tag{C.12}$$

BIBLIOGRAPHY

BIBLIOGRAPHY

ABS. 2006. *'Safehull-Dynamic Loading Approach' for Vessels*. 16855 Northchase Drive, Houston TX 77060 USA: American Bureau of Shipping.

ABS. 2010. *'Dynamic Loading Approach' for Floating Production, Storage and Offloading (FPSO) Installations*. 16855 Northchase Drive, Houston TX 77060 USA: American Bureau of Shipping.

Adegeest, L. J. M., Braathen, A., & Løseth, R. M. 1998. Use of Non-Linear Sea-Loads Simulations in Design of Ships. *Pages 53 – 58 of: Practical Design of Ships and Mobile Units*.

Alford, L. K. 2008. *Estimating Extreme Responses Using a Non-Uniform Phase Distribution*. Ph.D. thesis, The University of Michigan.

Alford, Laura K., Kim, Dae-Hyun, & Troesch, Armin Walter. 2011. Estimation of Extreme Slamming Pressures Using the Non-Uniform Fourier Phase Distributions of a Design Loads Generator. *Ocean Engineering*, **38**, 748–762.

Baarholm, Gro Sagli, & Jensen, Jørgen Juncher. 2004. Influence of Whipping on Long-term Vertical Bending Moment. *Journal of Ship Research*, **28**(4), 261–272.

Belenky, V. L. 2005. On Long Numerical Simulatons at Extreme Seas. *In: 8th International Ship Stability Workshop*.

Bishop, R. E. D., & Price, W. G. 1979. *Hydroelasticity of Ships*. Cambridge University Press.

Cartwright, DE, & Longuet-Higgins, MS. 1956. The Statistical Distribution of the Maxima of a Random Function. *Proceedings of the Royal Society of London. Series A, Mathematical and Physical Sciences*, **237**(1209), 212–232.

Cassidy, Mark Jason. 1999. *Non-Linear Analysis of Jack-Up Structures Subjected to Random Waves*. Ph.D. thesis, The University of Oxford.

Dietz, J. S., Hansen, P. F., & Jensen, J. J. 2004. Design Wave Episodes for Extreme Value Ship Responses. *In: International Symposium on Practical Design of Ships and Other Floating Structures*.

Dinsenbacher, Alfred, & Engle, Allen. 2011. *Guidelines for Hydroelastic Model Design, Testing and Analysis of Loads & Responses*. Tech. rept. Naval Surface Warfare Center Carderock Division.

Dysthe, Kristian, Krogstad, Harald E, & Müller, Peter. 2008. Oceanic Rogue Waves. *Annual Review of Fluid Mechanics*, **40**.

Feller, William. 1965. *An Introduction to Probability Theory and Its Applications*. Vol. 2. John Wiley & Sons.

Friis-Hansen, Peter, & Nielsen, Lars P. 1995. On the New Wave Model for the Kinematics of Large Ocean Waves. *In: 14th International Conference on Offshore Mechanics and Arctic Engineering*.

Gumbel, E. J. 1958. *Statistic of Extremes*. Columbia University Press.

Hodapp, David P., Kim, Dae-Hyun, & Troesch, Armin W. 2012. On the Finite Approximation of a Gaussian Process and its Effect on Extreme Value Theory. *Preprint Submitted to Ocean Engineering*.

Hughes, Owen F. 1988. *Ship Structural Design: A Rationally-Based, Computer-Aided Optimization Approach*. SNAME.

Jensen, Jørgen Juncher. 1996. Second-order wave kinematics conditional on a given wave crest. *Applied Ocean Research*, **18**(2-3), 119–128.

Jensen, Jørgen Juncher. 2008. Extreme Value Predictions and Critical Wave Episodes for Marine Structures by FORM. *Ships and Offshore Structures*, **3**(4), 325 – 333.

Jensen, Jørgen Juncher. 2009. Stochastic Procedures for Extreme Wave Load Predictions - Wave Bending Moment in Ships. *Marine Structures*, **22**(2), 194–208.

Kim, Cheung Hun. 2008. *Nonlinear Waves and Offshore Structures*. Advanced Series on Ocean Engineering, vol. 27. World Scientific.

Kim, Dae-Hyun, & Troesch, Armin W. 2011. Stochastic Wave Inputs for Extreme Roll in Near Head Seas. *In: Proceedings of the 12th International Ship Stability Workshop*.

Kim, Dae-Hyun, & Troesch, Armin Walter. 2010. An Application of Design Load Generator to Predict Extreme Dynamic Bending Moments. *In: 29th International Conference on Ocean, Offshore Mechanics and Arctic Engineering*.

Kim, Dae-Hyun, Alford, Laura K., & Troesch, Armin W. 2010. Probability Based Simulation of Stern Slamming Design Events. *In: The 2010 Conference on Grand Challenges in Modeling and Simulation/Very Large Complex Systems*.

Kim, Dae-Hyun, Engle, Allen H., & Troesch, Armin W. 2011. Estimates of Long-Term Combined Wave Bending and Whipping for Two Alternative Hull Forms. *Transactions of SNAME*, **119**.

Kiureghian, A. Der. 2000. The Geometry of Random Vibrations and Solutions by FORM and SORM. *Probabilistic Engineering Mechanics*, **15**(1), 81–90.

Lehner, S. H. 2004. Extreme Wave Statistics from Radar Data Sets. *In: IEEE International Geoscience and Remote Sensing Symposium (IGARSS)*.

Lin, W. M., Bergquist, J. R., Collette, M. D., Liut, D., Treakle, T. W., Weems, K. M., Weems, M. H.C., & Zhang, S. 2008 (March). *Large Amplitude Motion Program (LAMP) for Ship Motions and Wave Loads Predictions Version 3.2.1.* Tech. rept. Science Applications International Corporation, 4321 Collington Road, Suite 250, Bowie, Maryland 20716.

Lin, Woei-Min, Collette, Matthew, Lavis, David, Jessup, Suart, & Kuhn, John. 2007. Recent Hydrodynamic Tool Development and Validation for Motions and Slam Loads on Ocean-Going High-Speed Vessels. *In: 10th International Symposium on Practical Design of Ships and Other Floating Structures*.

Lindgren, George. 1970. Some Properties of a Normal Process Near a Local Maximum. *The Annals of Mathematical Statistics*, **41**(6), 1870–1883.

Longuet-Higgins, M. S. 1957. The statistical analysis of a random, moving surface. *Philosophical Transactions of the Royal Society of London. Series A, Mathematical and Physical Sciences*, **249**(966), 321–387.

Madsen, H. O., Krenk, S., & Lind, N. C. 2006. *Methods of Structural Safety*. Dover Publications.

Newland, D. E. 2005. *An Introduction to Random Vibrations, Spectral & Wavelet Analysis*. Dover Publications.

Ochi, Michel K. 1978. Wave Statistics for the Design of Ships and Ocean Structures. *Transactions of SNAME*, **86**.

Ochi, Michel K. 1990. *Applied Probability and Stochastic Processes*. John Wiley & Sons.

Ochi, Michel K. 1998. *Ocean Waves*. Cambridge University Press.

Ochi, Michel K., & Motter, Lewis E. 1973. Prediction of Slamming Characteristics and Hull Responses for Ship Design. *Transactions of SNAME*, **81**.

Pastoor, L. W. 2002. *On the Assessment of Nonlinear Ship Motions and Loads*. Ph.D. thesis, Technische Universiteit Delft.

Richardson, William R. 2007. *General Procedure for Lifetime Seaway Load Estimation (LSLE) with Example*. Tech. rept. Naval Surface Warfare Center Carderock Division.

Rowan, T. H. 1990. *Functional Stability Analysis of Numerical Algorithms*. Ph.D. thesis, The University of Texas at Austin.

Shin, Y. S., Belenky, V. L., Lin, W. M., Weems, K. M., & Engle, A. H. 2003. Nonlinear Time Domain Simulation Technology for Seakeeping and Wave-Load Analysis for Modern Ship Design. *Transactions of SNAME*, **111**.

Soares, Guedes C., Fonseca, N., & Pascoal, R. 2008. Abnormal Wave-Induced Load Effects in Ship Structures. *Journal of Ship Research*, **52**(1), 30–44.

St. Denis, Manley, & Pierson, W. J. 1953. On the Motions of Ships in Confused Seas. *Trans. SNAME*.

Taylor, Paul H., Jonathan, Philip, & Harland, Léon A. 1995. Time Domain Simulation of Jack-Up Dynamics with the Extremes of a Gaussian Process. *In: 14th International Conference on Offshore Mechanics and Arctic Engineering*.

Torhaug, Rune. 1996. *Extreme Response of Nonlinear Ocean Structures: Identification of Minimal Stochastic Wave Input for Time-domain Simulation*. Ph.D. thesis, Stanford University.

Troesch, Armin W. 1997. *Study of the Use of Nonlinear Time Domain Simulation in a Design Loads Generator (DLG)*. Tech. rept. Final Report to the American Bureau of Shipping.

Tromans, Peter S., Anaturk, Ali R., & Hagemeijer, Paul. 1991. A New Model for the Kinematics of Large Ocean Waves - Application as a Design Wave. *In: Proceedings of the First International Offshore and Polar Engineering Conference*.

Vidic-Perunovic, Jelena. 2005. *Springing Response due to Bidirectional Wave Excitation*. Ph.D. thesis, Technical University of Denmark.

von Neumann, John. 1951. Various Techniques Used in Connection with Random Digits. *In:* Householder, A. S., Forsythe, G. E., & Germond, H. H. (eds), *Monte Carlo Method*. Applied Mathematics Series. National Bureau of Standards.

Weibull, Waloddi. 1951. A Statistical Distribution Function of Wide Applicability. *Journal of Applied Mechanics*, **18**(3), 293–297.

Wu, Guangyu. 2004. *Direct Simulation of Deterministic Prediction of Large-scale Nonlinear Ocean Wave-field*. Ph.D. thesis, Massachusetts Institute of Technology.